Quantifying and Modeling Subgrid Scale Snow Depth Variability in Forested Areas Throughout Multiple Climates in the Western United States

William Ryan Currier

A dissertation

submitted in partial fulfillment of the

requirements for the degree of

Doctor of Philosophy

University of Washington

2019

Reading Committee:

Jessica D. Lundquist (Chair)

Mark Wigmosta

Tobias Jonas

Program Authorized to Offer Degree:

Civil and Environmental Engineering

University of Washington

Abstract

Quantifying and Modeling Subgrid Scale Snow Depth Variability in Forested Areas Throughout Multiple Climates in the Western United States

William Ryan Currier

Chair of the Supervisory Committee:
Professor Jessica D. Lundquist
Civil and Environmental Engineering

The mountain snowpack provides natural storage of freshwater. This natural storage far exceeds the extent of manmade reservoirs. Furthermore, watersheds throughout the western United States can be predominantly covered in forests. Forests decrease atmospheric winds, alter the amount of incoming radiation, and intercept snowfall, leading to significant variation in snow depth throughout the forest. Snow depth variability influences the magnitude, timing, and temperature of streamflow. Additionally, snow depth variability can drive ecological processes and affect the energy exchanged between the land and the atmosphere.

To quantify snow depth variability in forests, spatially continuous, high-resolution (1-3 m) observations are needed at watershed extents. Chapter I of this dissertation evaluates the ability for airborne lidar to derive snow depth underneath the canopy by comparing airborne lidar to terrestrial lidar and snow depth probe transects from NASA's 2017 SnowEx campaign. Differences between gridded airborne lidar and ground-based observations did not increase underneath the canopy. Airborne lidar observations were therefore used in Chapter 2 to examine forest snow depth variability in four different snow climates throughout the western United

States. In the Jemez Mountains, NM and in Tuolumne, CA, snow depth differences between north and south-facing sides of the canopy were statistically significant and greater than or equal to the difference between areas underneath the canopy and in the open.

To account for this variability, a tiling parameterization, was incorporated into the Distributed Hydrologic and Soil Vegetation Model (DHSVM). The tiling parameterization explicitly simulates radiation differences within the forest and accounts for horizontal forest structure by using classifications from high-resolution vegetation maps. The tile parameterization therefore tested the impact of explicit forest representation on simulated snow water equivalent (SWE) and streamflow compared to the original implicit representation in three watersheds throughout the western United States. In Jemez, NM, where forests were relatively sparse and trees were 10.2 m tall, the tile model's grid-cell average snow disappearance date (SDD) was 12 days earlier and peak streamflow occurred 20-days earlier than the original model. In the Chiwawa, WA, where forests were dense and 17.2 m tall, SDD was 11 days later and late-season streamflow increased up to 11-13%. Despite statistically different snow depth distributions, forest edges had a relatively small effect on simulated streamflow (2-6%). However, grid cell average ablation rates and streamflow were primarily impacted by tiled grid cells, which only contained exposed and forested areas. The contrasting responses between the Jemez and Chiwawa were primarily controlled by the grid cells average fractional forest cover and the forest's radiation attenuation, which is a function of tree height and the sun's elevation angle. Ultimately, DHSVM's tile parameterization is a tool that more realistically represents forest radiation and while forest-edge contributions were relatively small within the existing forest structure, going forward, forest managers could use the tile parameterization to better understand how changes in the forest structure (e.g. maximizing forest shading) affect streamflow.

Dedication

To my family for their unwavering support and for their encouragement to follow my passions.

Acknowledgements

I would like to thank members of the graduate supervisory committee for their invaluable guidance and feedback. Specifically, I'd like to thank Jessica Lundquist for her mentorship, guidance, and patience. I would also like to thank Jessica for providing an abundance of opportunities in addition to those at the University of Washington, to work in various national parks and forests, and to visit and learn from others at various universities and research labs while being at UW. I would like to thank Tobias Jonas for providing the opportunity to visit his research group for two months in the winter of 2018 in Switzerland. I would also like to thank Tobias for his feedback as the research progressed even after leaving Switzerland. This trip to SLF provided experiences, conversations, and relationships that I'll never forget. I would like to thank Glen Liston for letting me visit him in Fort Collins, CO for a week and for teaching me the architecture of his hydrologic model, SnowModel. I would also like to thank Mark Wigmosta and Ning Sun for letting me visit their research group in Richland, WA and for teaching me the architecture of their hydrologic model, DHSVM. I would also like to thank Bart Nijssen for thoughtful feedback during both my masters and doctoral work. Lastly, I would like to thank Monika Moskal for serving as the Graduate School Representative.

I received financial support from a NASA Earth and Space Sciences Fellowship grant NNX16AO02H. I greatly appreciate the work by Clifford Mass, Neal Johnson, and Mimi Hughes for providing us with WRF data over Washington and California. I would also like to thank Tom Painter, Kathryn Bormann, Jeff Deems, and the NASA Airborne Snow Observatory program for providing ASO data. In addition, I would like to extend my gratitude to all those who participated and supported the NASA 2017 SnowEx campaign. Furthermore, I want to thank NCALM for the airborne lidar data and the field workers who maintained the Ameriflux,

SNOTEL, and California Department of Water Resources (CDWR) instrumentation over the years. Lastly, I would like to thank Jeff Deems, Charles Luce, Ernesto Trujillo, Matthew Sturm, and anonymous reviewers, who greatly improved the quality of the published chapters.

I also want to thank current and past members of the Mountain Hydrology Research Group at the University of Washington, in particular, Cassie Lumbrazo, Justin Pflug, Dylan Reynolds, Giulia Mazzotti, Victoria Ly, Steven Pestana, Susan Dickerson-Lange, Brian Henn, Karl Lapo, Nic Wayand, Mark Raleigh, Nicoleta Cristea, Teddy Thorson, Eric Keenan, Max Mozer, Hannah Hampson, Colin Buttler, Gwyn Perry, Adam Massmann, and Derek Beal. Your feedback on presentations and papers were great, and your camaraderie, feedback, coding tips, mentorship and friendship made my graduate research experience a joy. Last, but not least, I want to thank friends outside of my academic community, who have made the past five and a half years an unforgettable experience.

Published Material

At the time of writing, two of the following chapters have been published in a peer reviewed journal. I would like to acknowledge John Wiley and Sons, publisher of *Water Resources Research*, for granting permission to reproduce two of the articles in this dissertation.

The citations for published material are:

Currier, W. R., & Lundquist, J. D. (2018). Snow Depth Variability at the Forest Edge in Multiple Climates in the Western United States. *Water Resources Research*, *54*, 1–18. https://doi.org/10.1029/2018WR022553

Currier, W. R., Pflug, J., Mazzotti, G. Jonas, T. Deems, J. S., Gormann, K. J., et al. (2019). Comparing aerial lidar observations with terrestial lidar and snow-probe transects from NASA's 2017 SnowEx campaign. *Water Resources Research,* 1-10. https://doi.org/10.1029/2018wr024533

Table of Contents

List of Figures

List of Tables

Chapter 1 Introduction

The mountain snowpack provides natural storage of freshwater that far exceeds the extent of manmade reservoirs. In mountainous regions of the western United States, this natural reservoir system produces 70% of the total annual streamflow (D. Li et al., 2017), which generates electricity and supplies water for agriculture and municipalities. In addition, snow controls the distribution of terrestrial ecosystems, influences weather and climate systems, and supplies cool freshwater for fish and lower trophic organisms.

At the hillslope scale (1-100 m) (Clark et al., 2011), interactions between the meteorological conditions, terrain, and vegetation yield variation in snow depth and snow water equivalent (SWE) on the order of 100-300%. Snow depth or SWE's spatial variability at the hillslope scale leads to a nonuniform snow disappearance date across the basin, and thus the spatial variability at the hillslope scale influences the magnitude, timing, duration, and temperature of streamflow (Clark et al., 2011; Leach & Moore, 2014; Luce et al., 1998, 1999; Lundquist et al., 2005; Lundquist & Dettinger, 2005; Sun et al., 2018).

Recent snow depth variability studies have benefited from advancements in airborne and terrestrial lidar systems, which are capable of producing high-resolution (<5 m) snow depth maps (Broxton et al., 2015; Deems et al., 2006, 2008, 2015; Grünewald et al., 2010; Mott et al., 2010; Revuelto et al., 2015; Schirmer et al., 2011; Schirmer & Lehning, 2011; Trujillo et al., 2009, 2007; Wayand et al., 2018). Other methods such as snow-probe transects, synthetic aperture radar, and photogrammetry (structure from motion photography, satellite based stereo imagery) can be used to capture the hillslope-scale variability, but lidar provides data underneath the canopy and at greater areal extents than snow-probe transects. However, prior lidar evaluation studies used point-based measurements and thus were unable to explicitly evaluate lidar's ability

to capture snow depth's spatial variability. Furthermore, previous studies differed on whether airborne lidar errors were higher in the forest or in the open (Hopkinson et al., 2004; Reutebuch et al., 2003; Tinkham et al., 2014).

This dissertation quantifies our ability to observe snow depth variability at the hillslope scale in forested areas and quantifies the dominant modes of snow depth variability in these forested areas. This dissertation then incorporates a sub-grid cell tiling parameterization into a distributed hydrological model to simulate snow depth variability within model grid cells that are larger than the process scale. In turn, we hope that this dissertation will improve the simulation of land-atmospheric fluxes, ecological processes, and quantify the impacts that explicitly resolving the dominant modes of snow depth variability have on the timing and magnitude of streamflow. To achieve these goals, this dissertation has done the following.

In chapter II of this dissertation we comprehensively compared ALS, TLS, and snow-probe transects from NASA's 2017 SnowEx field campaign (Kim, 2018; Kim et al., 2017) to quantify their sensitivity and accuracy in capturing snow depth's spatial variability at high spatial resolution (50 cm – 5 m) across various vegetation types, including directly underneath the canopy. Once these lidar datasets were validated, in Chapter III, we used them to study snow depth variability within forested regions at four different snow climates within the western United States. In chapter III, we provide background on topographic and forest processes the effect snow depth variability. We also discuss how existing snow hydrology models account for spatial variability within model grid cells. In chapter III, we discussed how the observed snow depth variability could be used as an observational basis for a sub-grid cell parameterization within hydrologic models to account for forest-edge snow depth variability. In Chapter IV, we implemented this sub-grid cell tiling parameterization into a distributed hydrological model, to

test the watershed level impact of snow depth variability within forested areas within multiple climates.

Chapter 2 Comparing aerial lidar observations with terrestrial lidar and snow-probe transects from NASA's 2017 SnowEx campaign

William Ryan Currier[1], Justin Pflug[1], Giulia Mazzotti[2], Tobias Jonas[2], Jeffrey S. Deems[3,4], Kat J. Bormann[5], Thomas H. Painter[5,] Christopher A. Hiemstra[6], Arthur Gelvin[6], Zach Uhlmann[7], Lucas Spaete[7], Nancy F. Glenn[7], and Jessica D. Lundquist[1]

[1] Department of Civil and Environmental Engineering, University of Washington, Seattle, WA, USA
[2] WSL Institute for Snow and Avalanche Research SLF, Davos Dorf, Switzerland
[3] Cooperative Institute for Research in the Environmental Sciences, University of Colorado, Boulder, CO, USA
[4] National Snow and Ice Data Center, Boulder, CO, USA
[5] Jet Propulsion Laboratory, California Institute of Technology, Pasadena, CA, USA
[6] Cold Regions Research and Engineering Laboratory (CRREL), Fort Wainwright, AK, USA
[7] Department of Geosciences, Boise State University, Boise, ID, USA

Note: This chapter has been published in its current form as an article in Water Resources Research (Currier et al., 2019); the only differences are in section, figure, and table numbering. It is used here by permission of John Wiley and Sons.

2.1 Abstract

NASA's 2017 SnowEx field campaign at Grand Mesa, CO, generated Airborne Laser Scans (ALS), Terrestrial Laser Scans (TLS), and snow-probe transects, which allowed for a comparison between snow depth measurement techniques. At six locations, comparisons between gridded ALS and TLS observations, at 1-m resolution, had a median snow depth difference of 5 cm, root-mean-square-difference of 16 cm, mean-absolute-difference of 10 cm, and 3-cm difference in standard deviation. ALS generally had greater, but similar snow depth values to TLS, and results were not sensitive to the gridded cell size between 0.5 and 5 m. The greatest disagreements were where snow-off TLS scans had shrubs and high incidence angles, leading to deeper snow depths (>10 cm) from ALS than TLS. The low vegetation and oblique angles caused occlusion in the TLS data and thus produced higher snow-off bare earth models relative to the ALS. Furthermore, in sub-canopy areas where both ALS and TLS data existed, snow depth differences were comparable to differences in the open. Meanwhile, median values from 52 snow-probe transects and near-coincident ALS data had a mean difference of 6 cm, root-mean-square-difference of 8 cm, mean-absolute-difference of 7 cm, and a mean difference in the standard deviation of 1 cm. Snow depth probes had greater, but similar snow depth values to ALS. Therefore, based on comparisons with TLS and snow depth probes, ALS captured snow depth magnitude with better than or equal agreement to what has been reported in previous studies, and showed the ability to capture high-resolution spatial variability.

2.2 Introduction

Previous snow depth spatial variability studies have benefited from advancements in airborne and terrestrial lidar systems, which are capable of producing high-resolution (<5 m) snow depth maps (Broxton et al., 2015; Currier & Lundquist, 2018; Deems et al., 2006, 2008, 2013, 2015; Grünewald et al., 2010; Hedrick et al., 2018; Mott et al., 2010; Painter et al., 2016; Revuelto et al., 2015; Schirmer et al., 2011; Schirmer & Lehning, 2011; Trujillo et al., 2007, 2009; Wayand et al., 2018). Uncertainties in Airborne Laser Scanning (ALS) are a function of the laser's range, the topography, and the accuracy and precision of the laser's geospatial positioning and orientation (Deems et al., 2013; Glennie, 2007). Terrestrial Laser Scanning (TLS) views the terrain from a fixed height and position, and has similar sources of uncertainty to ALS (Figure 2.1). A stable ground surface is necessary to minimize error in TLS data collections, and surveys that take place in deep snow can be subjected to snow compaction throughout the scan (Deems et al., 2015; Hartzell et al., 2015)

The scan angle of an ALS or TLS survey is important to consider because the laser beam diverges as the range increases, which can increase the snow depth uncertainty, specifically in areas where the laser has a high incidence angle (Deems et al., 2013; Hartzell et al., 2015). For instance, as the incidence angle increases, the footprint of an obliquely-incident laser pulse elongates when interacting with the surface, which introduces uncertainty in the return signal. A rigorous error propagation effort showed that discrete lidar returns with incidence angles greater than 60º at a 500-m range have an additional vertical and horizontal uncertainty introduced, which ranges from 2-10 cm (Hartzell et al., 2015). This uncertainty will rise in regions where vegetation cover occludes (or partially occludes) the laser from penetrating to the ground (K. E. Anderson et al., 2018).

These sources of uncertainty however are offset by the ability of lidar systems to map snow depth at high resolutions across complex and forested terrain. Therefore, airborne lidar has been used to map snow depth since 2001 (Hopkinson et al., 2001, 2004). Since then, snow depth maps derived from ALS and TLS have been compared with snow-probe measurements, Global Navigation Satellite System (GNSS) observations, and acoustic snow depth sensors (Table 2.1). These studies have used a collection of point-scale measurements, characterized by a small support of 0.01 – 0.5 m (Blöschl, 1999), which can contain geolocation uncertainty, and do not provide the same measurement density over wide areas as lidar scans. Therefore, previous studies were unable to explicitly quantify the ability for aerial or terrestrial lidar systems to determine the spatial variability of snow depth. Furthermore, these studies come to different conclusions as to whether errors are higher in the forest or in the open, and whether these errors are due to low lying vegetation or significant geolocation errors (Hopkinson et al., 2004; Reutebuch et al., 2003; Tinkham et al., 2014). Lastly, previous studies have not explicitly evaluated discrepancies in lidar data due to different viewing perspectives.

NASA's 2017 SnowEx field campaign at Grand Mesa, CO generated a suite of coincident, or nearly-coincident, airborne and ground based observations – including ALS, TLS, and snow depth probe transects. This extensive data set offers the unique opportunity to test the consistency of different snow depth measuring techniques and test their sensitivity at various spatial resolutions over a gradient of different vegetation types (Kim, 2018; Kim et al., 2017).

In this technical note, we comprehensively compare ALS observations to TLS surveys for the first time and also compare ALS observations to snow-probe transects from NASA's 2017 SnowEx campaign. We therefore quantify the sensitivity and consistency of different snow depth

measurement techniques to capture spatial variability at high spatial resolution across various land cover types, including directly underneath the forest canopy.

2.3 Location and data

Grand Mesa, CO

NASA's 2017 SnowEx campaign took place on Grand Mesa in western Colorado, USA (Figure 2.2). There were six TLS sites with variable components of grasses, shrubs, and trees. Shrubby cinquefoil (*Dasiphora fruticosa*), big sagebrush (*Artemesia tridentata* ssp. *vaseyena*), and silver sagebrush (*A. cana* ssp. *viscidula*) are all under 1-m height and prevalent on the windier western end of the Mesa. Forests were present at four TLS sites (A, K, N, and the Ranger Station) and are predominantly Engelmann spruce (*Picea engelmannii*), with much rarer components of subalpine fir (*Abies lasiocarpa*), Aspen (*Populus tremuloides*), and lodgepole pine (*Pinus contorta* var. *latifolia*). The Ranger Station site was unique in that it included a grassy picnic area, parking lot, and two cabins with partly snow-free roofs.

Airborne Laser Scans (ALS)

The snow-off ALS survey was collected by the NASA Airborne Snow Observatory (ASO) on 26 September 2016, with snow-on data collected on 8 and 16 February 2017 using methods, instrumentation, and processing steps described in Painter et al. (2016) to receive three-dimensional point cloud data. All three flight altitudes were around 4100 m above sea level, which is about 1000-1100 m above the terrain leading to a footprint size of about 26 cm and an average total point density of around 18 points per square meter. See Text S1.a. for additional details.

Terrestrial Laser Scans (TLS)

Snow-off TLS data were collected between 26 September and 2 October 2016 using two different lidar scanners, a Riegl VZ-1000 and Leica C-10 ScanStation (Table S1). Snow-on scans were collected o near coincident dates in February (Table S1), and tripod legs were placed in contact with the ground or a packed snow surface to minimize potential errors from snow compaction throughout the survey. Scans with the Riegl VZ-1000 were obtained from 50º off-nadir, to 150º pointing upwards, in a 360º rotation at a 0.03º increment (angular resolution of 0.03º) in both rotation planes. Scans with the Leica C-10 ScanStation were obtained from 45º off-nadir, to 180º pointing upwards, in a 360º rotation at a 0.06º increment in both rotation planes. See Text S1.b. for additional details.

Snow depth probe transects

Both a standard 3 m snow depth probe and a 1.2 m GPS equipped Magnaprobe (Matthew Sturm & Holmgren, 2018), which automatically records the geolocation of each snow depth measurement to within ±2.5 m, were used to compare with ALS data. Snow-probe transects did not overlap with TLS surveys, therefore only ALS was compared with snow-probe transects. The snow depth measurement uncertainty of both snow depth probe measurements is estimated to be around ±5 cm due to the potential penetration of the probe's tip into the soil underneath the snow, impacts of low vegetation, and the angle of the probe (Matthew Sturm & Holmgren, 2018). The location of each standard snow-probe transect was estimated using linear lines between georeferenced transect poles used to guide surveyors from beginning to end. This resulted in an estimated ±5 m geolocation error for each snow depth measurement. More details are provided in Text S2.

2.4 Methods

Classification and gridding

Three-dimensional point clouds were classified as ground and non-ground points (e.g. vegetation) using LAStools *lasground* (http://rapidlasso.com/lastools/), which is a variation of the Axelsson (2000) methodology. We used default parameters within *lasground,* with the exception of choosing step sizes of 2 m and 10 m to allow for some uncertainty in the classification.

Snow-on and snow-off scans from both ALS and TLS were gridded to 0.5, 1, 2, 3, and 5-m spatial resolutions using two strategies: first using the lowest of all ground points within each grid cell, and second, averaging all ground-classified points within a grid cell. With both strategies, if the difference between the two elevation models built with the two different classifications (step 2 m and 10 m) was greater than 20 cm, then that grid cell was removed from the comparison. Across all sites, this filtering removed 0.14% of the snow depth values. Lastly, while there was little difference in the results based on gridding methodology, we focus our results on snow depth values derived from the lowest-return gridding method, and show results from the alternative strategy in the supplemental material (Text S4).

TLS incidence angle

For each TLS site, we used the geographic position of the snow-off TLS scan position, the ALS digital terrain model at 1-m resolution, and the TLS scanner's Height Relative to the Target Terrain Height (HRTTH) to derive an incidence angle map for each snow-off TLS scan position. From each scan position, we searched out radially, computing the distance between the TLS scanner and the target grid cell (DIST). We then approximated the slope of each target grid cell using the two adjacent elevation values within the azimuthal direction of the search line. The

incidence angles (θ) corresponding to each snow-off scan position were computed over the entire domain (Eq. 1) to create a set of incidence angle maps for each snow-off TLS scan position. Finally, the lowest incidence angle within the set of maps was determined for each grid cell.

$$\theta = \tan^{-1}\left(\frac{DIST}{HRTTH}\right) - slope \quad (1)$$

2.5 Results

ALS vs. TLS comparison

Both ALS and TLS surveys captured a similar snow depth magnitude and variability. Using all data where the 1-m ALS and TLS snow depth grids overlapped, we found a median difference of 5 cm (4%), root-mean-square-difference (RMSD) of 16 cm, and mean absolute difference of 10 cm (Table 2.2). At individual TLS sites, ALS and TLS snow depth differences ranged from a 1-13 cm (1-10%) median difference (Figure 2.3 and S3; Table 2.2 and S3), 10-28 cm RMSD (Table S5), and a 7-20 cm mean absolute difference (Table S6), where the ALS data generally showed deeper snow depth values. The closest agreement occurred at TLS Sites A, B and K, where median snow depth differences were less than 5 cm, while the worst agreement was at the Ranger Station, where median snow depth difference was 13 cm.

At individual sites, the difference in standard deviations from the 1-m resolution ALS and TLS snow depth ranged between -7 and 1 cm (mean: -3 cm). The TLS snow depth data generally contained a higher standard deviation due to the difficulty in obtaining a snow-off surface while scanning shrubs at a high-incidence angle (Section 2.6.1.i). Snow-off or snow-on surfaces were not compared directly because the ALS data were not subjected to absolute registration, resulting in a vertical bias relative to the TLS snow-off data (Text S1).

Differences in the median snow depth values between ALS and TLS were generally not sensitive to the gridding resolution between 50 cm and 5 m (Table S3). However, at the Ranger Station, differences in median snow depth values increased 5 cm as the gridding resolution increased from 50 cm to 5 m. Similar to median snow depth differences, the difference in standard deviations between ALS and TLS were generally not sensitive to the gridding resolution, except at the Ranger Station and Site P (Table S4).

ALS vs. snow-probe transects

In general, both standard and magnaprobe snow depth measurements had higher snow depths than the ALS snow depth values on both 8 and 16 February (Figure 2.4). The median values from combining both standard and magnaprobe snow depth transects were on average 6-cm greater than the median values from ALS on 8 and 16 February, and the mean absolute difference and RMSD of that comparison were 7 cm and 8 cm, respectively.

On average, snow-probe transects agreed with the ALS standard deviation. For instance, ALS and snow-probe transects differed in their standard deviations by 1 cm and 0 cm on 8 and 16 February, respectively. The mean absolute difference and RMSD between the standard deviation values from the snow-probe and ALS transects were 3 cm and 4 cm, respectively, on both 8 and 16 February. The general agreement between ALS and TLS standard deviations, as well as between standard deviations from ALS and snow depth transects, suggests that ALS data were able to resolve the snow depth variability at high spatial resolution.

ALS and TLS vegetation interactions

At TLS Sites A, K, N, and the Ranger Station, the domains were partly forested (Table 2.2). At these locations, the median snow depth difference between ALS and TLS was 1-cm greater underneath the canopy than in the open. Similarly, the RMSD and mean absolute difference

between ALS and TLS snow depth increased by 6 and 4 cm, respectively. The largest change in RMSD and mean absolute difference was at the Ranger Station site, which generally performed worse than the other sites likely due to multipath errors (see Section 2.6.1.ii). Removing the Ranger Station site, the RMSD and mean absolute difference only increased by 3 and 2 cm. Lastly, the difference in the snow depth's standard deviation between ALS and TLS did not generally increase (Table 2.2). This implied that ALS snow depth data were not adversely affected by canopy cover. However, between the four forested sites, ALS data were missing 17% of the 1-m grid cells, and TLS data were missing 21%. This left 66% of the total forested area to compare ALS and TLS snow depth (Table 2.2).

2.6 Discussion

Sources of snow depth differences

2.6.1.i Shrubs and high incidence angles

Despite similar differences between ALS and TLS within open and forested areas, TLS snow depth was 10-13 cm less than ALS snow depth in areas where shrub heights were greater than 20 cm in combination with TLS incidence angles that were higher than 80º (Figure S5). These localized differences caused the TLS derived snow depth to be more heterogenous and have lower median snow depths than ALS data (Table 2.2 and S4).

These differences were likely due to the different viewing perspectives of ALS and TLS (Figure 2.1). For instance, it is easier to penetrate a shrub with a laser at a normal rather than an oblique angle. Prior studies using snow depth probes or GNSS observations noted that airborne lidar systematically underestimated snow depth in areas with significant ground vegetation (Hopkinson et al., 2004), or ALS errors increased where there were shrubs (DeBeer & Pomeroy, 2010; Spaete et al., 2011). In contrast, our results suggested aerial lidar did penetrate at least

partly through the shrubs, while the terrestrial lidar was partially occluded by the shrubs (K. E. Anderson et al., 2018), ultimately biasing the TLS derived snow depth too low. The ability for ALS to see through the shrubs in our study is likely explained by differences in ground vegetation type between Grand Mesa and previous studies, the relatively low altitude and high point density of the ALS survey, and the development in recent years of more advanced algorithms that extract discrete lidar returns from the return energy waveforms (Pfennigbauer & Ullrich, 2011; Ullrich & Pfennigbauer, 2011).

2.6.1.ii Multipath errors.

A combination of high incidence angles and shrubs were unable to explain all of the snow depth differences. For instance, we still found greater than 10-cm snow depth differences near the TLS snow-off scan positions at the Ranger Station site. At the Ranger Station site, TLS scans were not vertically or horizontally registered with each other as a result of multipath errors in the GNSS measurements. Multipath errors were likely more significant at the Ranger Station than other TLS sites due to the topography, buildings, and vegetation. We were unable to quantify potential registration errors at other sites due to the lack of a snow-free static structure; however, qualitative point cloud comparisons with trees showed that the ALS and TLS surveys were co-registered with each other. Fortunately, we were able to detect and correct for these multipath errors at the Ranger Station site. Registering both the TLS scans to the snow-free roof in the ALS data improved the metrics at the Ranger Station site. However, the Ranger Station site was a smaller domain compared to other TLS sites; therefore, the TLS registration only changed the median snow depth difference using all ALS and TLS snow depth data from 5 cm to 4 cm. Furthermore, there was little change in other metrics using all the ALS and TLS snow depth (Table S11).

2.6.1.iii Snow depth probes

ALS derived snow depth was 6 cm less on average than what was recorded with snow-probe measurements. We suspect that the general bias in ALS measurements relative to snow-probe measurements is due to snow-probe penetration through the soil/vegetation (Matthew Sturm & Holmgren, 2018). For instance, human observers are more likely to press a probe into duff or soft ground, and are known to unintentionally avoid making measurements in very low or zero snow (both of which would bias probe measurements high). Furthermore, while ALS reached the ground through shrubs more than TLS, it may have done so less frequently than a human observer. Interestingly, both magnaprobe and standard snow depth transects generally showed higher snow depth values despite different methodologies. For instance, magnaprobe geolocation uncertainties are independent between each measurement, while the geolocation uncertainty of a standard snow-probe transect increases along the transect line. Since both types of snow-probe transects typically provided higher median snow depth values than ALS, snow depth differences between median values were not likely due to geolocation errors.

Comparisons to previous studies

Despite contrasting median snow depth differences between ALS vs. TLS and ALS vs. snow-probe transects, the RMSD was 16 cm between all 1-m gridded ALS and TLS snow depth data. Meanwhile, the RMSD between median values from ALS and snow-probe transects was 8 cm. This suggested that ALS data, which was evaluated using TLS data and 52 snow-probe transects (n=10,926) through a variety of vegetation, resulted in a RMSD that was equal to or better than previous studies which evaluated ALS using point based measurements (DeBeer & Pomeroy, 2010; A A Harpold et al., 2014; Spaete et al., 2011; Tinkham et al., 2011, 2014). Lastly, the mean absolute difference using all ALS and TLS data was 10 cm, while the mean

absolute difference between the median values of the ALS and snow-probe transects was 7 cm. These mean absolute differences were similar or less than the mean absolute difference reported in Painter et al. (2016) (Table 2.1).

Context of the snow depth differences

After co-registering the Ranger Station site (Section 2.6.1.ii), the median snow depth differences were relatively small, ranging between 1-7 cm, or 1-5% using the observed median snow depth across all TLS sites (1.29 m). Because the differences in observations are absolute in nature, as the snow depth decreases, the percent differences will increase. For instance, if the median snow depth was 25 cm, the percent difference in median values would have ranged from 4-28%.

2.7 Conclusions

Both ALS and TLS data captured a similar spatial variability and magnitude of snow depth at high spatial resolutions. For instance, at 1-m resolution, ALS and TLS data had a median difference of 5 cm, RMSD of 16 cm, a mean absolute difference of 10 cm, and a difference in standard deviation of 3 cm. Additionally, comparisons between median values from ALS and snow-probe transects showed a mean difference of 6 cm, mean absolute difference of 7 cm, RMSD of 8 cm, and a mean difference in the standard deviation of 1 cm. These differences, in combination with the differences between ALS and TLS were similar or better than those reported in previous evaluations of ALS.

In addition, ALS and TLS showed similar differences underneath the canopy to those in the open, but ALS data at 1-m spatial resolution were unable to derive snow depth in part of the forested area due to missing ground returns. Furthermore, ALS and TLS both inherently have different viewing perspectives. In localized areas where the snow-off TLS scans had high

incidence angles and were scanning shrubs, TLS surveys derived shallower snow depths relative to ALS. This implied that ALS pulses were more likely to be from the ground, whereas the ground was relatively more occluded in the TLS data. Using these results, we provide suggestions for future campaigns that evaluate ALS data (Text S5). These recommendations focus on explicitly evaluating void filling routines in forested areas (Zheng et al., 2016), minimizing differences in viewing perspective, and ground controlling observations to provide absolute georegistration.

2.8 Tables

Table 2.1 Previous evaluations of aerial and terrestrial lidar

Study	Laser	ALS/ TLS	Snow [Y/N]	Height above terrain [m]	Evaluation method	Evaluation summary
Reutebuch et al. (2003)	Saab TopEye Lidar System (Helicopter)	ALS	N	200	GNSS	Different forest densities: (Mean difference ±1σ) Clearcut: 0.16 ± 0.23 m, Heavily thinned: 0.18 ±0.14 m, Lightly thinned: 0.18 ± 0.18m, Uncut: 0.31 ± 0.29 m
Hopkinson et al. (2001, 2004)	Optech ALTM 1210 and 1225	ALS	Y	700-750	Snow Depth Probes	Mean Difference: 0.01-0.13 m. Canopy understory can systematically underestimate snow depth
Hopkinson et al. (2005)	Optech ALTM 2050	ALS	N	1200	GNSS	Mean difference: 0.04 m
Prokop et al. (2008)	Riegl LPM-i800HA	TLS	Y	~2	Tachymetry and Snow Probing	Tachymetry: 1σ = 0.02 m Snow Probe: 1σ = 0.1 m
Prokop (2008)	Riegl LPM-i800HA and LPM-2K	TLS	Y	~2	Snow Depth Probes	Snow depth accuracy within 0.1 m for distances <500 m
DeBeer & Pomeroy (2010)	Optech ALTM 3100	ALS	Y	3500	Snow Depth Probes	RMSD was 0.17 m, Greater error of up to 0.6 m in locations with exposed alpine shrubs.
Spaete et al. (2011)	Leica ALS50 Phase II	ALS	N	900	GNSS	RMSD 0.07-0.22 m – largest errors on herbaceous slopes
Tinkham et al. (2011)	Leica ALS50 Phase II	ALS	N	900	GNSS	RMSD 0.13 – 0.46 m depending on vegetation type. Mean RMSD: 0.28 m
Hopkinson et al. (2012)	Optech ALTM 3100	ALS	Y	3500	Snow Depth Probes	Mean differences: Lower open area: 0.07 m Forested areas: 0.13 m Alpine Open area: -0.04 m Lidar generally had higher snow depth than snow probe
Tinkham et al. (2014)	Leica ALS50 Phase II	ALS	Y	900	Snow Depth Probes	Shrub/meadow: RMSD = 0.14 m Forested areas 0.2-0.35 m
Kirchner et al. (2014)	Optech GEMINI ALTM 1233	ALS	Y	600	Plowed Area Comparison	Biased up to 0.05 m
Harpold et al. (2014)	Optech GEMINI ALTM 1233	ALS	Y	Varied	Acoustic Snow Depth Sensors	RMSD 0.23 m between 60 acoustic snow depth sensors

Deems et al. (2015)	Riegl VZ-4000 and Riegl VZ-6000	TLS	Y	~2	Snow Pit	Difference was 0.01 m between TLS and corner of snow pit
Painter et al. (2016)	Riegl Q1560 - Dual lasers.	ALS	Y	~3000	Snow Depth Probes	Exposed area, Mean Absolute Difference: 0.08 m in 15 x 15 m area

Table 2.2 Percentage of the domain that contained a vegetation height > 2 m (forest), snow depth differences between lidar datasets at 1-m spatial resolution in the open and in the forest, and percent of the forested area where both ALS and TLS data were unable to derive snow depth.

	Forested area	**Median difference** [Open/ Forest] $median(ALS - TLS)$	**RMSD** [Open/ Forest] $\sqrt{\frac{\sum(ALS - TLS)^2}{N}}$	**Mean absolute difference** [Open/ Forest] $\overline{abs(ALS - TLS)}$	**Difference in standard deviation** [Open/ Forest] $\sigma_{ALS} - \sigma_{TLS}$	**Forested area missing by ALS**	**Forested area missing by TLS**	**Forested area captured by both ALS and TLS**
Site A	17% 2,685 m^2	2 cm 0 cm	17 cm 18 cm	12 cm 11 cm	-3 cm -3 cm	26% 689 m^2	15% 405 m^2	63% 1,687 m^2
Site B	--	1 cm --	16 cm --	10 cm --	-7 cm --	--	--	--
Site K	20% 3,552 m^2	4 cm 5 cm	9 cm 13 cm	7 cm 10 cm	-1 cm -4 cm	12% 417 m^2	24% 859 m^2	67% 2,392 m^2
Ranger Station	36% 2,257 m^2	12 cm 16 cm	25 cm 34 cm	18 cm 24 cm	-6 cm -6 cm	21% 479 m^2	30% 684 m^2	59% 1,328 m^2
Site P	--	7 cm --	11 cm --	8 cm --	6 cm --	--	--	--
Site N	37% 3,887 m^2	6 cm 8 cm	20 cm 22 cm	12 cm 15 cm	-5 cm -5 cm	14% 549 m^2	17% 663 m^2	71% 2,745 m^2
All Forested Sites	24% 12,381 m^2	5 cm 6 cm	16 cm 22 cm	10 cm 14 cm	-3 cm -3 cm	17% 2,134 m^2	21% 2,611 m^2	66% 8,152 m^2
All Sites (Forest + Open)	--	5 cm	16 cm	10 cm	-3 cm	--	--	--

Table 2.3: Manufacturer specifications for different lidar scanners

ALS/ TLS	Lidar Scanner	Sites: Snow-on Survey Date	Horizontally Adjusted	Scanner height above terrain [m]	Scanner's Range [m]	Wavelength [nm]	Beam Divergence [mrad]
ALS	Riegl LMS-Q1560	8 and 16 February 2017	N	~1000-1100	5800	1064	0.25
TLS	Leica ScanStation C-10	A: 9 February 2017 B: 17 February 2017 N: 15 February 2017 Ranger Station: 17 February 2017	Y	2	300	532	0.1
TLS	Riegl VZ-1000	K: 8 February P: 9 February 2017	N	2	1400	1550	0.3

Table 2.4 Snow depth transect date, type, and sample size.

Date	Type	Total Number of Transects (n)	Notes
February 8	Standard Transect	15 (n=1248)	--
February 9	Magnaprobe Transect	16 (n=1657)	--
February 16	Standard Transect	9 (n=2447)	--
February 17	Magnaprobe Transect	12 (n=5574)	Spiral

Table 2.5: Median snow depth differences between ALS and TLS at the six different TLS locations based on the gridding resolution. Differences are reported in cm and percentages. Percentages were normalized by the median snow depth from the ALS survey.

	Median Snow Depth Differences [cm/%] ALS – TLS						
Gridding Resolution	**Site A**	**Site B**	**Site K**	**Ranger Station**	**Site P**	**Site N**	**All Data**
50 cm	2 2%	4 5%	4 2%	12 9%	6 5%	6 4%	**5** **4%**
1 m	1 1%	1 1%	4 2%	13 10%	7 5%	7 4%	**5** **4%**
2 m	2 2%	1 1%	4 2%	16 12%	6 5%	7 4%	**5** **4%**
3 m	2 2%	0 0%	3 2%	19 15%	6 5%	7 4%	**5** **4%**
5 m	2 2%	0 0%	3 2%	22 17%	6 5%	9 6%	**5** **4%**

Table 2.6: Difference in snow depth standard deviation between ALS and TLS at the six different TLS locations based on the gridding resolution. Differences are reported in cm and percentages. Percentages were normalized by the median snow depth from the ALS survey.

	Difference in Standard Deviation [cm/%] ALS – TLS						
Gridding Resolution	**Site A**	**Site B**	**Site K**	**Ranger Station**	**Site P**	**Site N**	**Mean**
50 cm	-4 -4%	-6 -8%	-1 -1%	-3 -2%	-1 0%	-2 -1%	**-3** **-3%**
1 m	-3 -3%	-7 -10%	-1 -1%	-5 -4%	1 1%	-3 -2%	**-3** **-3%**
2 m	-1 -1%	-6 -8%	-2 -1%	-10 -8%	3 3%	-3 -2%	**-3** **-3%**
3 m	-1 -1%	-5 -6%	-2 -1%	-15 -11%	6 4%	-3 -2%	**-2** **-2%**
5 m	2 2%	-7 -9%	-4 -3%	-24 -19%	11 8%	-1 0%	**-2** **-2%**

Table 2.7: Root mean square difference between ALS and TLS derived snow depth at the six different TLS locations based on the gridding resolution.

	Root Mean Square Difference [cm]						
Gridding Resolution	**Site A**	**Site B**	**Site K**	**Ranger Station**	**Site P**	**Site N**	**All Data**
50 cm	19	16	8	21	11	16	**15**
1 m	17	16	10	28	11	20	**16**
2 m	19	18	12	36	13	24	**19**
3 m	23	20	14	45	16	28	**22**
5 m	32	20	15	51	23	30	**27**

Table 2.8: Mean absolute difference between ALS and TLS derived snow depth at the six different TLS locations based on the gridding resolution.

	Mean Absolute Difference [cm]						
Gridding Resolution	**Site A**	**Site B**	**Site K**	**Ranger Station**	**Site P**	**Site N**	**All Data**
50 cm	13	11	6	16	8	11	**10**
1 m	12	10	7	20	8	13	**10**
2 m	11	10	8	25	8	15	**11**
3 m	12	11	8	30	8	17	**12**
5 m	13	11	8	35	10	18	**13**

Table 2.9: Median snow depth differences between ALS and TLS. Percentages were normalized by the median snow depth from the ALS survey. Table S7 differs from Table S3 as the gridding was performed using the average of the classified ground points instead of the lowest ground point.

	Median Snow Depth Differences [cm/%] ALS – TLS						
Gridding Resolution	**Site A**	**Site B**	**Site K**	**Ranger Station**	**Site P**	**Site N**	**All Data**
50 cm	8 8%	4 5%	2 1%	13 10%	8 6%	10 6%	**6** **5%**
1 m	8 8%	1 1%	2 1%	15 11%	8 6%	11 7%	**6** **5%**
2 m	9 9%	1 1%	1 1%	16 13%	9 7%	12 7%	**6** **5%**
3 m	11 11%	0 0%	2 1%	17 13%	10 8%	13 8%	**7** **5%**
5 m	13 14%	0 0%	3 2%	18 15%	10 8%	14 8%	**7** **5%**

Table 2.10: Difference in snow depth standard deviation between ALS and TLS at the six different TLS locations based on the gridding resolution. Percentages were normalized by the median snow depth from the ALS survey. Table S8 differs from Table S4 in the text as the gridding was performed using the average of the classified ground points instead of the lowest ground point.

	Difference in Standard Deviation [cm/%] ALS – TLS						
Gridding Resolution	**Site A**	**Site B**	**Site K**	**Ranger Station**	**Site P**	**Site N**	**Mean**
50 cm	-5 -5%	-6 -8%	-1 -1%	-3 -2%	-2 -2%	-2 -1%	**-3** **-2%**
1 m	-5 -5%	-7 -10%	-1 -1%	-5 -4%	-2 -2%	-4 -2%	**-3** **-2%**
2 m	-4 -4%	-6 -8%	-2 -1%	-8 -6%	-3 -2%	-5 -3%	**-3** **-3%**
3 m	-4 -4%	-5 -6%	-2 -1%	-8 -6%	-5 -4%	-8 -5%	**-4** **-3%**
5 m	-6 -7%	-7 -9%	-4 -3%	-10 -8%	-9 -7%	-10 -6%	**-5** **-4%**

Table 2.11Root-mean-square-difference between ALS and TLS derived snow depth at the six different TLS locations based on the gridding resolution. Table S9 differs from Table S5 in the supplement as the gridding was performed using the average of the classified ground points instead of the lowest ground point.

	Root Mean Square Difference [cm]						
Gridding Resolution	**Site A**	**Site B**	**Site K**	**Ranger Station**	**Site P**	**Site N**	**All Data**
50 cm	23	16	7	23	12	17	**16**
1 m	22	16	8	31	12	20	**17**
2 m	21	18	9	39	13	23	**19**
3 m	23	20	10	45	14	25	**21**
5 m	26	20	12	52	28	26	**25**

Table 2.12 Mean absolute difference between ALS and TLS derived snow depth at the six different TLS locations based on the gridding resolution. Table S10 differs from Table S6 in the supplement as the gridding was performed using the average of the classified ground points instead of the lowest ground point.

	Mean Absolute Difference [cm]						
Gridding Resolution	**Site A**	**Site B**	**Site K**	**Ranger Station**	**Site P**	**Site N**	**All Data**
50 cm	15	11	5	17	9	13	**11**
1 m	15	10	6	22	10	15	**11**
2 m	16	10	6	27	11	17	**13**
3 m	18	11	6	30	11	18	**14**
5 m	20	11	7	35	14	20	**16**

Table 2.13 Snow depth differences between ALS and TLS using different metrics at the Ranger Station site after the TLS data were co-registered to the snow-free part of the roof. `All data` reflect the snow depth difference metric using all data from TLS Sites A, B, K, N, P, and the co-registered Ranger Station. Gridding was performed using the lowest of the classified ground points instead of the average of the ground points.

	Median Snow Depth Difference [cm] ALS-TLS		**Difference in Standard Deviation [cm] ALS-TLS**		**Root Mean Square Difference [cm]**		**Mean Absolute Difference [cm]**	
Gridding Resolution	**Ranger Station**	**All Data**	**Ranger Station**	**All Data**	**Ranger Station**	**All Data**	**Ranger Station**	**All Data**
50 cm	3	5	-3	-3	17	15	10	10
1 m	5	4	-5	-3	26	16	14	10
2 m	6	4	-8	-3	34	19	19	11
3 m	7	4	-8	-2	40	22	23	12
5 m	8	4	-10	-1	47	27	28	13

2.9 Figures

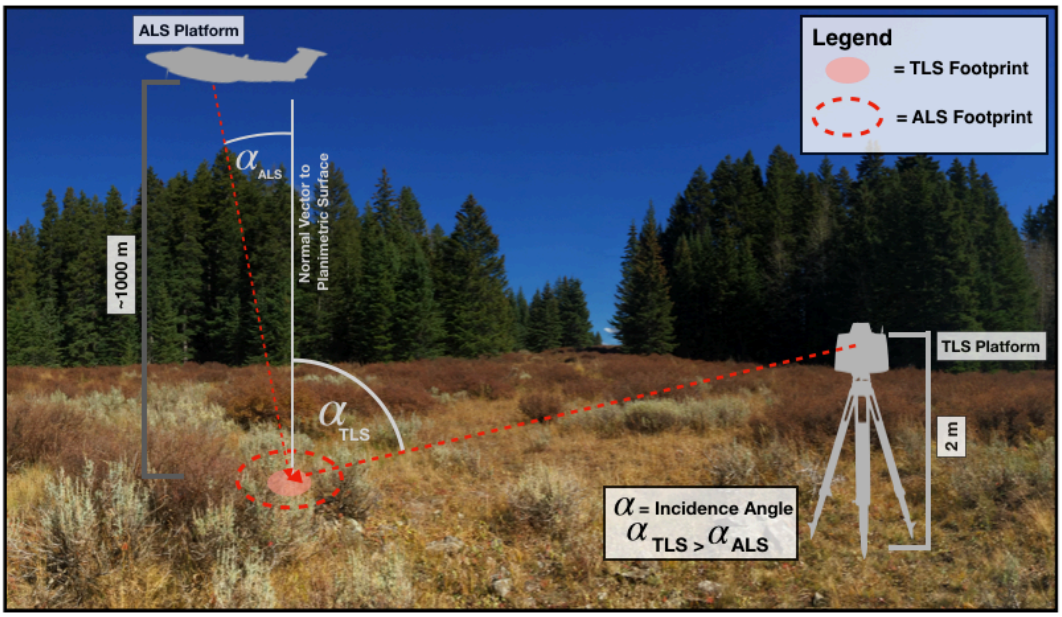

Figure 2.1 Conceptual diagram of ALS and TLS scans during the snow-off survey. Photo is from the western end of Grand Mesa, CO, USA. Aircraft height and size are not to scale.

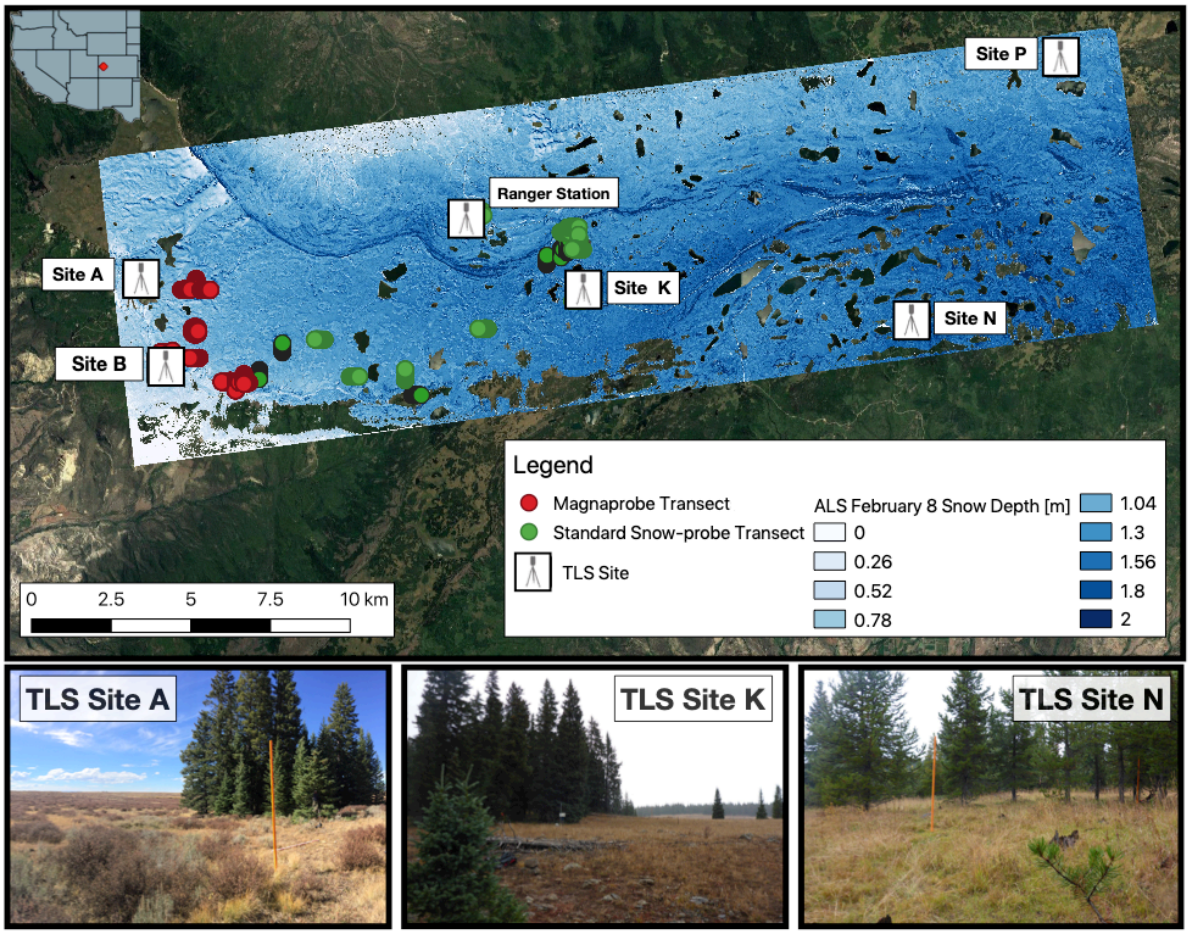

Figure 2.2 Distribution of ALS, TLS, and snow-probe transects across Grand Mesa, Colorado (top panel). Ground images collected in September 2016 demonstrate the variability and state of the ground vegetation at the TLS sites (bottom panels). Many gaps within the ALS data are water bodies which were intentionally masked out with the national hydrography dataset.

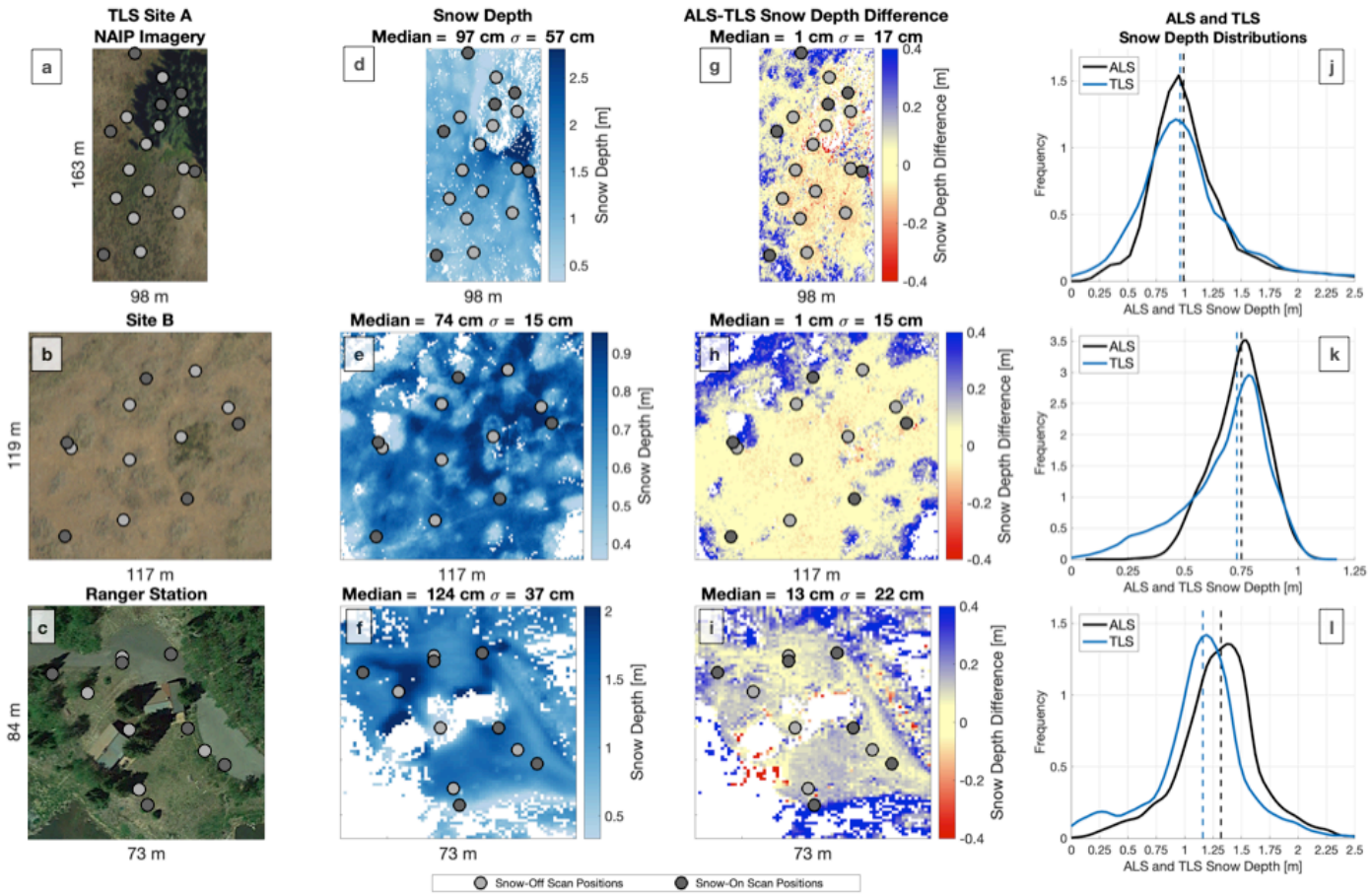

Figure 2.3 a-c: True color imagery for TLS Sites A, B (USDA NAIP), and the Ranger Station (© 2018 Google). d-f: Average of the ALS and TLS snow depth. Areas that were missing either ALS or TLS data were removed from the analysis and are shown in white. g-i: ALS snow depth minus TLS snow depth at 1-m resolution. j-l: ALS and TLS snow depth distributions. Dashed lines show the median value of the distribution. Figure S3 shows similar results for TLS Site K, N, and P.

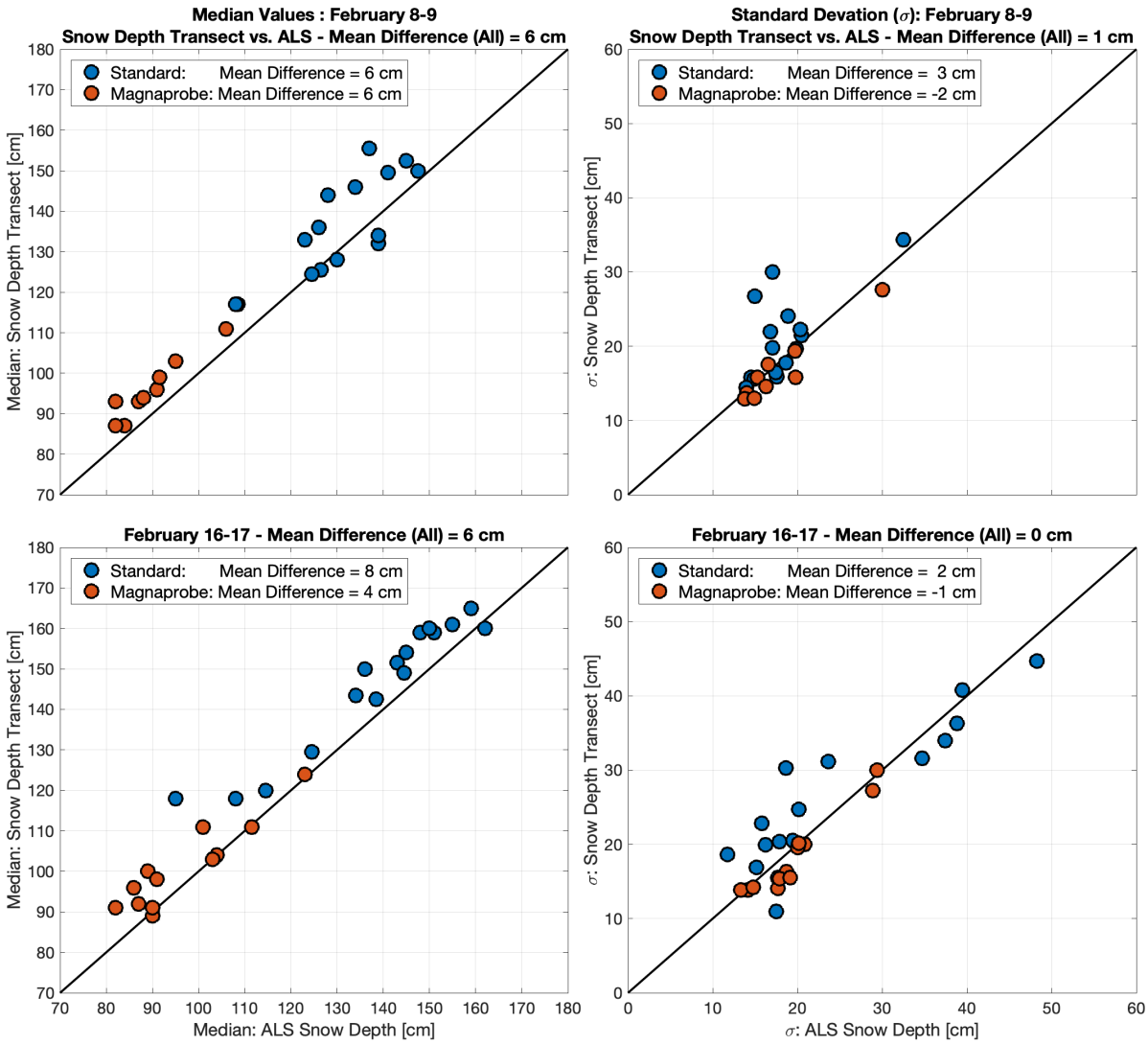

Figure 2.4 Left column: comparison between median snow depth values from snow-probe transects (standard and magnaprobe) and ALS snow depth data from 8 and 16 February 2017. Right column: comparison between standard deviations from the snow-probe transects (standard and magnaprobe) and the ALS data from 8 and 16 February 2017. "(All)" implies that the mean difference was used by combing either the standard deviation of the transect or the median snow depth values from both the standard and magnaprobe snow depth transects.

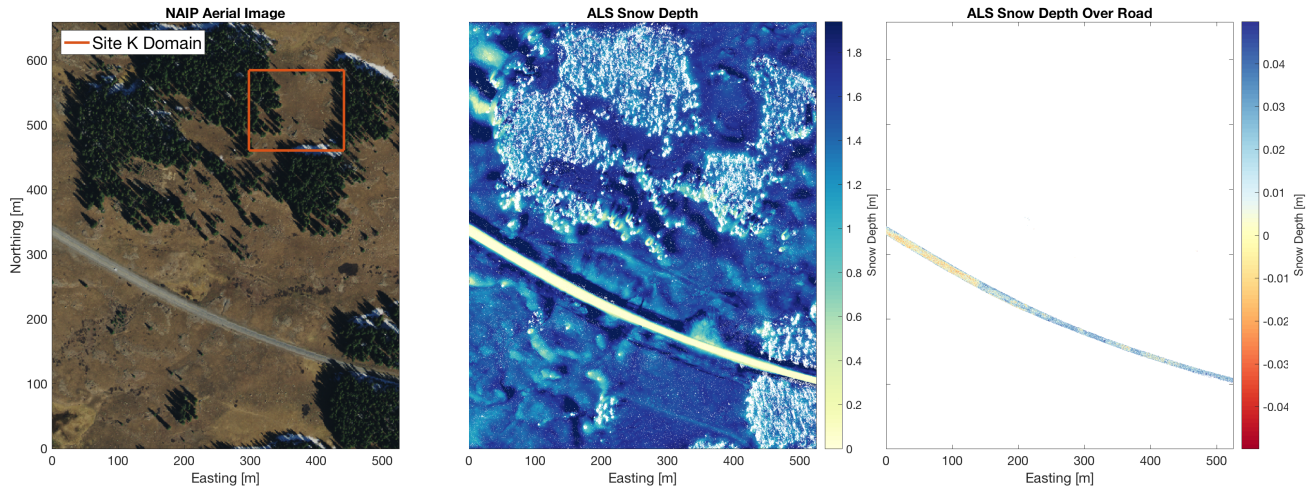

Figure 2.5: ALS derived snow depth at 1-m resolution on 8 February 2017 along a section of plowed road (route 65) just south of TLS Site K. Mean snow depth along the road was 1 cm with 17% of the area showing snow depths exactly equal to 0 cm.

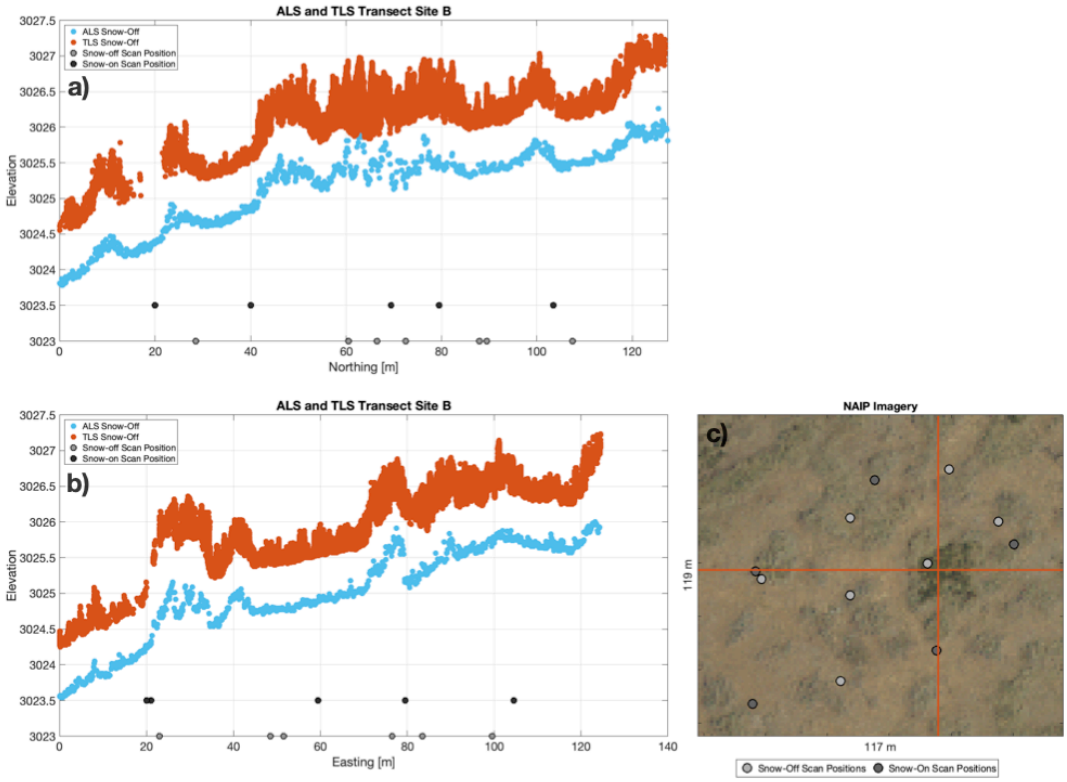

Figure 2.6: a.) South to north point cloud transect at TLS Site B. Point cloud transect was 0.5 m wide. All points are shown. b.) West to east point cloud transect at TLS Site B. c.) NAIP imagery showing south to north and west (a) to east point (c) cloud transects

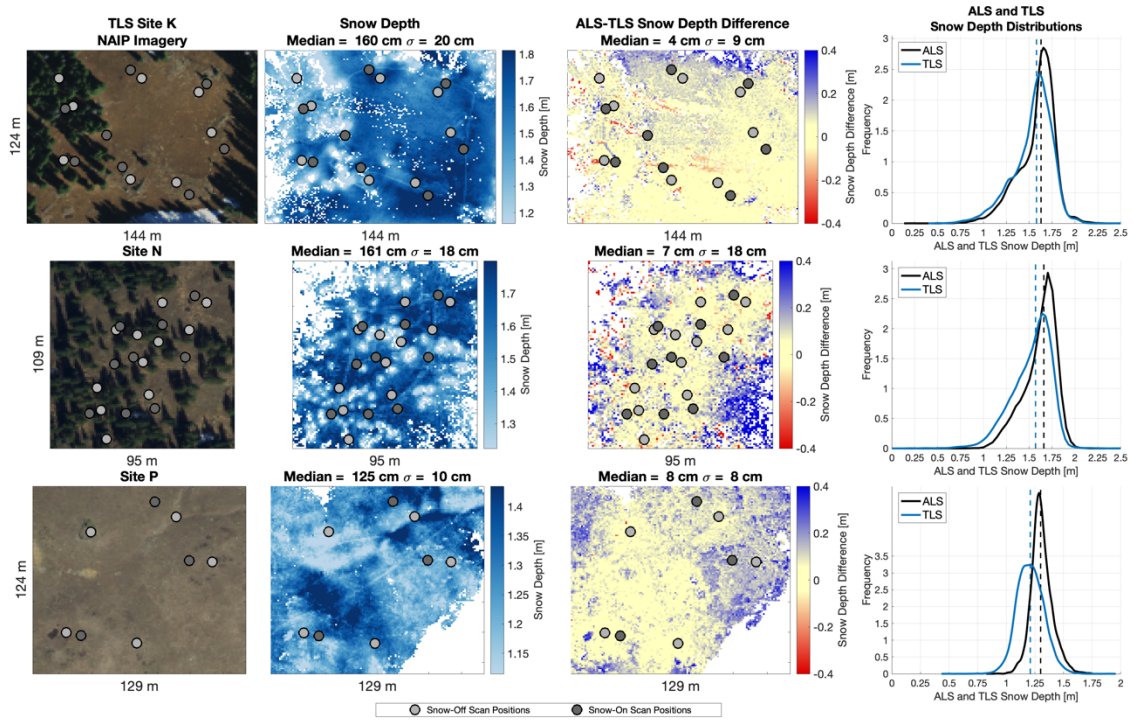

Figure 2.7: Same as Figure 2.3 in the main text but for TLS Site K, N, and P.

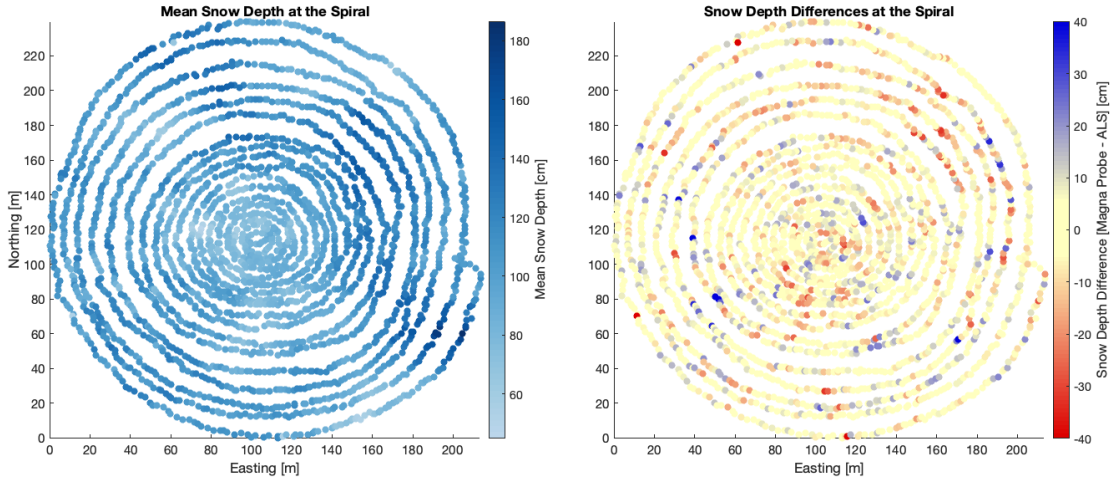

Figure 2.8 Left: Averaged snow depth between ALS and magnaprobe at sampled areas. Right: Spatial distribution of snow depth differences between the magnaprobe and ALS.
The spiral had a 0 cm difference between the median snow depth value despite normally distributed errors around 0 cm (1σ = 10 cm). Furthermore, the magnaprobe standard deviation had a 0 cm difference from the standard deviation of the gridded ALS snow depth data.

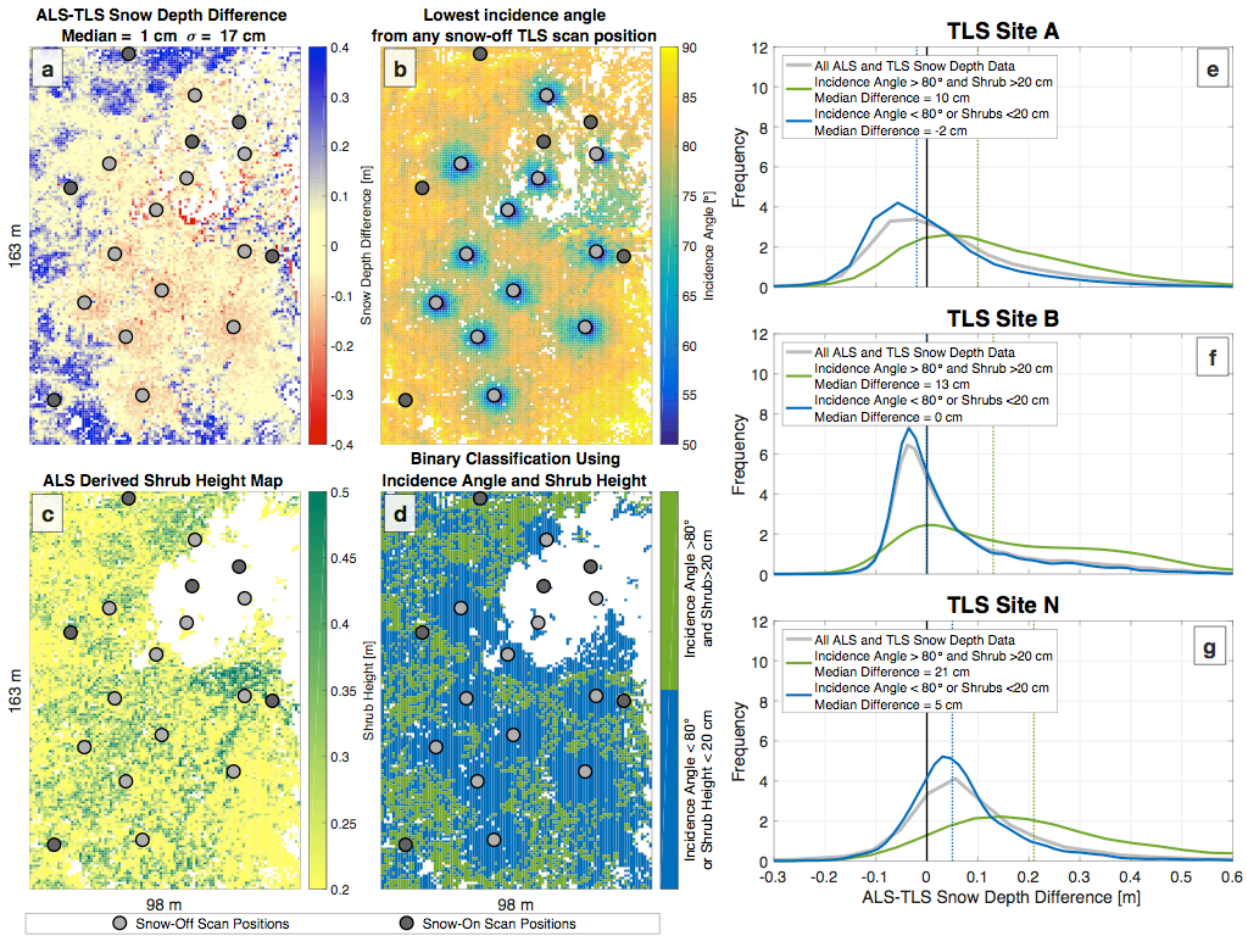

Figure 2.9 a.) Snow depth differences between ALS and TLS derived snow depth at TLS Site A (same as in Figure 2.3). b.) The lowest incidence angle that a TLS snow-off pulse hit the terrain from any of the TLS snow-off scan positions. c.) Shrub height map. d.) Binary classification that considers the incidence angle and shrub height. e-f.) Histograms showing ALS snow depth subtracted by TLS snow depth, separated into different areas using the binary classification map (d).

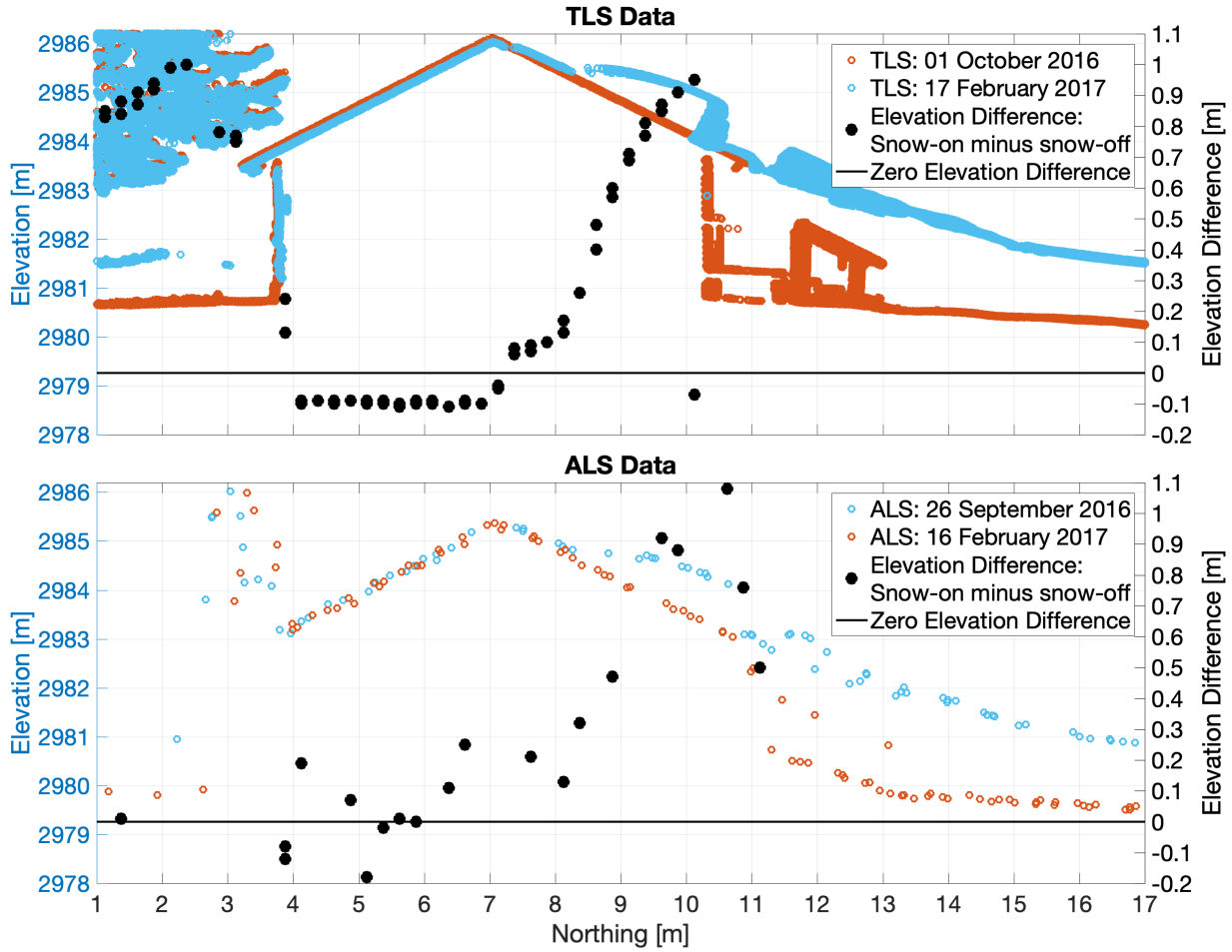

Figure 2.10 Snow-on and snow-off, south to north point cloud transects of a cabin at the Ranger Station site. South side of the cabin was snow free. Black dots show the elevation difference (axis right) between the lowest point within a 25-cm bin.

2.10 Appendix A: Additional specifications and details of ALS and TLS data

Airborne Laser Scans (ALS)

ALS point cloud data were originally processed to a WGS84 UTM Zone 13 N horizontal reference system, which had a WGS84 ellipsoid as the vertical datum. To ensure consistency with the TLS data, the ALS point cloud's vertical datum was transformed from Ellipsoidal to NAVD88 GEOID12B. Using 243 RTK survey points that had a 2 – 7 cm vertical uncertainty, we found that the snow-off ALS survey gridded at 1-m resolution had an elevation difference that was on average 69 cm (elevation difference: $1\sigma = 39$ cm). These differences in elevation can be explained by the ALS survey not being registered to ground control points, as the survey was designed to determine relative differences in snow depth. Using known snow-free targets (plowed road, buildings, and trees) within the domain, we found that the relative difference between the snow-on and snow-off ALS surveys were negligible (Figure S1). Therefore, other than changing the vertical datum, no relative registration adjustments were made to the ALS point clouds used for snow depth quantification.

Terrestrial Laser Scans (TLS)

Both snow-off and snow-on TLS surveys used reflectors along with differentially corrected GNSS surveys to merge individual point clouds together and transform these point cloud data from the scanner reference system to the geographical coordinate system - WGS84 UTM Zone 13N with an NAVD88 vertical datum (GEOID12B).

An analysis of the ALS and TLS scans at the Ranger Station, the only area where all three units scanned, indicated satisfactory horizontal agreement between Riegl scanners, while the Leica ScanStation C-10 survey appeared to have a horizontal offset. When the ALS data from the 17 February and the 23 February 2017 Riegl VZ-1000 point clouds were compared, they

were horizontally aligned (easting and northing) with the two man-made structures, which served as reference targets. However, the Leica ScanStation C-10 survey was horizontally offset 1.22 m to the east and 0.49 m south, relative to the ALS scan and the Riegl VZ-1000 scan. At TLS Sites A and N, translating the snow-on and snow-off data from the Leica ScanStation C-10 by the same amount resulted in the correct horizontal alignment of the trees relative to the snow-off and snow-on ALS surveys. Thus, TLS point clouds that used the Leica ScanStation C-10 were translated 1.22 m to the east and 0.49 m south to match the ALS and Riegl VZ-1000, but were not rotated or vertically translated (Table S1). At TLS Site K, the Riegl VZ-1000 snow-on and snow-off survey showed that the data were horizontally aligned with the trees from the ALS scans without any translation. At TLS Site B and P, there were no trees or man-made objects, but shrubs and the topography appeared to align (Figure S2).

2.11 Appendix B: Sample sizes, dates, and methods for snow depth transects

On the western end of Grand Mesa, standard snow depth probe transects were coincident with snow-on ALS flights, while magnaprobe measurements occurred one day after the snow-on ALS flights (Table S2). One magnaprobe transect on 17 February 2017 was sampled in a spiral starting at the center, rather than a straight line. The spiral consisted of 2701 snow depth measurements, walking a total distance of 5.9 km in a 240 x 214 m area. The nearest 1-m ALS snow depth value was extracted from the estimated position of each snow-probe measurement.

In September 2016, the beginning, intermediate, and end points of the standard snow-probe transects were marked with t-posts and vertically placed, red PVC piping. The t-posts' geographic coordinates were obtained in July 2017 using differentially corrected GNSS surveys. On 8 and 16 February 2017, snow depth measurements were collected along a transect every 3-m using the standard 3-m snow depth probe. In forested areas, flagging was used to guide the individual walking the snow depth transect. Despite efforts to guide the manual snow depth transects with marked posts, flagging, and a compass, maintaining a straight line was difficult, especially in the forest.

2.12 Appendix C: Sensitivity to results from different survey dates

Ultrasonic snow depth sensors and observed changes in snow depth

At TLS Sites K and N, ten and seven ultrasonic snow depth sensors were installed, respectively. The Ranger Station site and TLS Site A each had a meteorological tower with one ultrasonic snow depth sensor. At TLS Sites K and N, depth sensors were placed underneath the canopy and in the open, while at the Ranger Station and TLS Site A, snow depth sensors were in the open. All ultrasonic sensors were used to determine relative snow depth changes between the ALS flight and TLS scan, as the lidar surveys did not always occur on the same day. For instance, between 8 and 9 February, snow depth decreased at Sites K, N, and A by 1-3 cm. Similarly, between 15 and 16 February, snow depth decreased by 1-5 cm across all monitored sites. Lastly, between 16 and 17 February, snow depth decreased by 1-4 cm and was unchanged at TLS Site A.

Effect on results

Differences reported within the main text should not be adversely affected due to changes in snow depth between survey dates. Using the observed changes in snow depth from compaction, we note that median differences reported in Table S3 and Table 2.2 could decrease by a maximum of 3-4 cm at TLS Sites A, B, K, P, and the Ranger Station. Median snow depth differences at these sites could therefore range from -2 – 10 cm instead of 1 – 13 cm (Table S3).

TLS Site N had a TLS survey one day before the ALS survey, while the aforementioned sites had a TLS survey after the ALS survey. At site N there was 1-5 cm of snow compaction at the site between the TLS and ALS survey. However, in general ALS still recorded higher snow depth values. Similarly, the magnaprobe observations took place one day after the ALS survey where snow depth was observed to compact and/or melt, but magnaprobes generally recorded more snow depth

than the ALS observations. Both the comparison at Site N and the comparison to the magnaprobes implied that snow depth differences are dominated by uncertainties in the accuracy of the instrumentation, different viewing perspectives, and inherent survey errors, their combined influence being of greater magnitude than snow compaction and melt between surveys.

2.13 Appendix D: Sensitivity between using the lowest ground point or the average of the ground points

Sensitivity tests between using the lowest ground point or the average of the ground points to grid snow-off and snow-on bare-earth models from ALS and TLS (Section 3.a.) showed that the greatest agreement was when we used the lowest of the ground points to grid bare-earth models. However, results were not much different. For instance, the median snow depth difference between all ALS and TLS data increased 1 cm when using the average of the ground points to create bare-earth models instead of the lowest grid point. Across all sites, the median snow depth difference between ALS and TLS ranged from 1-15 cm using the average of the ground points to grid the 1-m spatial resolution bare-earth models, instead of 1-13 cm when using the lowest ground point (Table S3; Table S7). The most sensitive site was TLS Site A, where snow depth differences between ALS and TLS were 7 cm higher using the average of the ground points at 1-m spatial resolution rather than the lowest ground point (Table S3; Table S7). We found that the TLS snow-off bare-earth model was the most sensitive to the gridding decision. Shrubs in the snow-off TLS data were being classified as "ground," and using the average of the TLS snow-off ground points increased the elevation of the snow-off TLS bare earth model, ultimately deriving less snow depth than when using the lowest ground point to create the bare-earth model.

Similar to the median snow depth difference, there were little change in other metrics when using the average ground points instead of the lowest ground point to grid the bare-earth models. The difference in standard deviation between ALS and TLS snow depth data at 1-m spatial resolution ranged from -7 to 1 cm depending on the TLS site no matter whether we used the average of the ground points or the lowest ground point to create the bare-earth model (Table S4; Table S8). The RMSD between ALS and TLS snow depth data at 1-m spatial resolution ranged from 8-31 cm using the average of the ground points, instead of 10-28 cm using the lowest ground point to grid the bare-

earth models (Table S5; Table S9). Lastly, the mean absolute difference between ALS and TLS snow depth data at 1-m spatial resolution ranged from 6-22 cm using the average of the ground points, instead of 7-20 cm using the lowest ground point to grid the bare-earth models (Table S6; Table S10).

2.14 Appendix E: Suggestions for future evaluations of airborne lidar

This study used ALS data that was surveyed from 1000-1100 m above ground level (AGL), resulting in point densities of around 18 pts/m^2. However, airborne lidar is often flown at higher altitudes to maximize aerial coverage during flight times. Uncertainty in ALS surveys generally increase with flight altitude due to angular uncertainties in the inertial measurement unit and boresite calibration. Furthermore, the laser beam footprint increases with flight height. This reduces the return energy magnitude, and in steep terrain can adversely affect the 3-D positional accuracy of the elevation point (for both discrete and waveform-recoding systems). Lastly, flying at higher AGL altitudes decreases the ground point density (for given lidar system settings) and can reduce point densities to around 1-4 pts/m^2 (Painter et al., 2016). While ground point densities can be artificially reduced and examined using this data, the influence of angular uncertainties, which increase with flight height and a changing footprint, could be explored in future comparisons if multiple flight altitudes are included in the ALS survey.

While the airborne survey was at a relatively low AGL (~1000 m), ALS data were not spatially complete in heavily forested areas at 1-m spatial resolution (Table 2.2). To have a spatially complete dataset, values are often interpolated using a void filling routine. Zheng et al. (2016) interpolated areas underneath the canopy with areas in the open and found that this risked overestimating snow depth by 10 cm. TLS data were also not spatially complete in the forest, due to the spatial configuration of the scan positions, and therefore we could not properly assess the effect of a void filling routine on the spatial variability and magnitude of snow depth. We advocate that future studies use ground-based observations to identify proper void filling routines

and determine their effects on the magnitude and spatial variability of snow depth underneath the canopy.

Furthermore, future ground validation studies of remote sensing products should attempt to minimize geolocation errors in ground observations, reduce different viewing perspectives, and ground control remote sensing observations to minimize potential vertical and horizontal offsets. Future ground observations should take advantage of marked locations that can be identified while in the field and within the remote sensing data. Known locations could include unique trees identified from a snow-off ALS survey or unique man-made structures. Additionally, utilizing drone based lidar would yield high point density observations, view the terrain from the same perspective as airborne lidar scans, and provide greater flexibility than TLS in covering larger areas. Lastly, using ground control will reduce uncertainty in the vertical and horizontal position of the lidar returns (Text S1.a.). This will allow quantification of absolute errors, rather than relative differences, within each snow-off or snow-on dataset. This would also improve comparisons of spatial variability between other independent datasets (e.g. terrestrial lidar, structure-from-motion, stereo-based satellite imagery, or synthetic aperture radar) to ALS snow-off and/or snow-on data.

Chapter 3 Snow depth variability at the forest edge in multiple climates in the western United States

William Ryan Currier & Jessica D. Lundquist

Department of Civil and Environmental Engineering, University of Washington, Seattle, WA, USA

Note: This chapter has been published in its current form as an article in Water Resources Research (Currier & Lundquist, 2018); the only differences are in section, figure, and table numbering. It is used here by permission of John Wiley and Sons.

3.1 Abstract

Snow depth variability between different sides of the forest edge was analyzed using airborne lidar in the Olympic Mountains, WA; Tuolumne River Watershed, CA; Jemez Caldera, NM; and the Boulder Creek Watershed, CO. At Boulder Creek there were statistically significant snow depth differences between leeward and windward forest edges (mean: 38%), which were likely the result of cold winter temperatures (-5 - -10°C), substantial wind speeds (>10-12 m s^{-1}), and the forest architecture. In the Olympic Mountains, wind speeds were similar to Boulder Creek, but snow depth differences between forest edges were not significantly different, likely due to winter temperatures near 0°C and a more continuous forest distribution. At Jemez, forest shading likely caused significant snow depth differences between north and south-facing forest edges (mean: 32%). Tuolumne had similar incoming solar radiation to Jemez, but only two of the four sites contained significant snow depth differences between north and south-facing forest edges (14% and 31%). The Tuolumne sites without significant edge differences received less direct solar radiation due to shading by surrounding topography. At Jemez, Boulder Creek, and Tuolumne, snow depth differences between forest edges were greater than or equal to differences between exposed and under canopy areas. Furthermore, at Jemez and Tuolumne, forest-edge snow depth differences were similar to snow depth differences between different aspects in exposed areas. Therefore, snow depth differences between forest-edge classifications are of similar magnitude to classifications currently used to represent sub-element heterogeneity within hydrologic models. Therefore, representation of forest-edge variability within models should be explored.

3.2 Introduction:

Across a distance of 100-m, i.e., the hillslope scale (Clark et al., 2011), snow depth and snow water equivalent (SWE) can vary on the order of several meters or 100-300%. This variability is a function of the topography, meteorological conditions, and forest architecture. Understanding and predicting snow depth's spatial variability at the hillslope scale based on these interactions improves the prediction of processes at the watershed scale, such as streamflow magnitude, timing, and temperature, particularly during late summer flows (Clark et al., 2011; Leach & Moore, 2014; Luce et al., 1998, 1999; Lundquist et al., 2005; Lundquist & Dettinger, 2005; Sun et al., 2018). Furthermore, understanding snow depth's spatial variability is valuable for ecologists predicting species distributions (Carlson et al., 2015; Dedieu et al., 2016; Ford et al., 2013), and for simulating land-atmosphere interactions (Liston, 1999, 2004).

Prior work has shown significant snow depth variability along forest edges (Broxton et al., 2015; Church, 1933; Hiemstra et al., 2002, 2006; Musselman et al., 2008). In this manuscript, we used high-resolution (1-3 m) digital elevation models (DEM) and canopy height models (CHM) to test two hypotheses regarding the amount of snow located along the forest edge, labeled HP1 and HP2.

(HP1) Motivated by previous work that has showed the importance of forest shading on forest-edge snow depth distributions (Golding & Swanson, 1978; Lawler & Link, 2011; Musselman et al., 2008, 2015; Seyednasrollah & Kumar, 2014), we tested whether north-facing forests edges contained statistically greater snow depths than south-facing forest edges.

(HP2) In addition, previous work has also demonstrated the importance of scour and wind related deposition along forest edges (Brandle, J.R., Finch, 1991; Geddes et al., 2005; Hiemstra

et al., 2002, 2006; Tabler, 2003), and therefore we tested whether leeward forest edges have statistically greater snow depths than windward forest edges.

To determine which processes affect snow depth differences along the forest edge between various climates, we tested HP1 and HP2 at four different regions within the western United States. Using these results along with a comparison of meteorological data, we provide insight into why snow depth variability along forest edges differs between regions. Furthermore, we related the snow depth differences between different sides of the forest edge to the variability within the rest of the domain. For instance, we compared forest-edge snow depth differences to snow depth differences between exposed and forested areas, as well as snow depth differences between different slope aspects within exposed areas. Ultimately, we used the forest-edge snow depth distributions as an observational basis to discuss conceptual ideas for simulating this heterogeneity within a model element.

This paper is organized as follows: Section 3.3 provides background on hillslope-scale snow processes and sub-element spatial representations within current hydrologic models. Section 3.4 details the locations of our study sites and the data used. Section 3.5 describes how we classified different domains and the statistical tests used in this study. Section 3.6 presents our results. Section 3.7 provides insight into why forest-edge snow depth distributions differed between sites and discusses the hydrologic modeling implications of our results. We conclude in section 3.8.

3.3 Background

Forest and topographic processes affecting snow depth variability

Topography and vegetation both influence the accumulation and ablation of snow at the hillslope scale. In windy locations, more snow can accumulate on the leeward side of a hillslope due to preferential deposition (M. Lehning et al., 2008; Mott et al., 2010; Mott & Lehning,

2010), as well as redistribution of already fallen snow from the windward location (Elder et al., 1991; Greene et al., 1999; Liston & Sturm, 1998; Pomeroy & Gray, 1990). Furthermore, in the northern hemisphere, north-facing slopes receive less incoming solar radiation and can experience lower melt rates than south-facing slopes (Grünewald et al., 2010). However, the magnitude of this effect varies as a function of slope, aspect, latitude, cloudiness, snow albedo, and the horizon angle.

Similarly, forests affect ablation rates by diminishing turbulent heat fluxes and reducing incoming solar radiation (Table 3.1) (T. E. Link et al., 2004; T. Link & Marks, 1999; Musselman et al., 2008, 2015; Veatch et al., 2009). Simultaneously, snow receives enhanced longwave radiation from the forest, which increases the melt rate, but the enhancement of longwave radiation has a more localized effect (Table 3.1) and varies between sun-lit and shaded forest edges (Lawler & Link, 2011; Musselman & Pomeroy, 2017; Seyednasrollah & Kumar, 2014; Webster et al., 2016, 2017; Woo & Giesbrecht, 2000).

Throughout the winter, forests also influence the accumulation of snow at the forest edge (Table 3.1). As the forest attenuates the wind speed, snow that has previously been scoured or snow that is falling from the atmosphere can be preferentially deposited and stored on the leeward side of the forest (Brandle, J.R., Finch, 1991; Geddes et al., 2005; Hiemstra et al., 2002, 2006; Tabler, 2003). We therefore combine two individual processes, snow redistribution and preferential deposition of snow on leeward forest edges, into the term wind related deposition, as data presented herein are insufficient to separate these two processes.

Modeling sub-element variability within existing snow models

Many of these physical processes are implemented in a variety of snow models, such as ALPINE3D (Michael Lehning et al., 2006) and SnowPALM (Broxton et al., 2015), but these

models often require explicit, high-resolution (< 10 m) simulations to resolve the hillslope-scale heterogeneity. Snow models that contain model element areas, or grid cells, greater than the process scale have developed parameterizations to address snow depth or SWE's variability within the model element.

Implicit representations assume processes affecting the snowpack behave linearly, and therefore physical characteristics within the model element can be averaged linearly (Blöschl, 1999; Slater et al., 2001). For instance, consider a model element that has a discontinuous forest distribution. An implicit representation of forest-snow interactions within this model element would linearly scale a vegetation characteristic (e.g. tree height) with the fractional representation of other land cover types so that the magnitude of the physical process (e.g. forest-snow interception) represents the average effect over the entire model element. Broxton et al. (2015) showed that an implicit representation of forest-snow interactions resulted in different simulations of physical processes (e.g. interception, wind redistribution) and less overall SWE than an explicit representation through high-resolution simulations, reflecting nonlinearities within forest-snow interactions.

Snow heterogeneity can be accounted for with sub-element probability distributions (Clark et al., 2011; Essery & Pomeroy, 2004a; Liston, 2004; Luce et al., 1999; Luce & Tarboton, 2004). Sub-element probability distributions assume a generally non-gaussian parametric distribution, which depends primarily on the coefficient of variation (Liston, 2004; Luce & Tarboton, 2004). Sub-element probability distributions have successfully been implemented for lumped and gridded model elements where they effectively simulated more realistic melt out dates and improved late-season streamflow (Clark et al., 2011; Luce et al., 1998, 1999), as well as land-atmospheric fluxes (Liston, 2004).

Another approach to capture the sub-element variability is through tiling, which groups different classifications based on vegetation types, elevation, or a combination of these, and assigns each classification a proportion of the model element. Therefore, snow depth variability is accounted for by independently simulating the physical processes unique to each classification. This effectively increases model resolution and requires unique meteorological conditions for each classification but reduces the computational load relative to high-resolution simulations by lumping areas that are hydrologically similar together (e.g. Moore, 1985). Tiling is often implemented within regional scale models such as the Variable Infiltration Capacity model (Andreadis et al., 2009; Liang et al., 1994; Nijssen et al., 2001) to explicitly represent processes related to elevation (e.g. orographic precipitation enhancement and temperature lapse rates), as well as those related to vegetation (e.g. differences in radiation and forest-snow interception). Tiling has also previously been used in the Arctic to simulate lateral exchange of blowing snow between model elements that are bare of vegetation to those filled with shrubs (Essery & Pomeroy, 2004b; MacDonald et al., 2009).

We note that implicit representations, sub-element probability distributions, and tiling are not mutually exclusive. For instance, within each tile, finer-scale processes could be implicitly represented, or each tile could be assigned its own probability distribution. Furthermore, land-atmospheric-fluxes within sub-element probability distributions are often implicitly represented (Liston, 2004).

In this paper, we built classifications based on forest and topographic processes using high-resolution (1-3 m) DEMs and CHMs to examine gridded snow depth observations. We used the forest-edge classifications and snow depth data to test whether forest-edge classifications based on solar and wind directions would include statistically different snow depths (HP1-HP2), and

thus require more explicit representation within sub-element model parameterizations. We leave the testing and evaluation of different sub-element model parameterizations for future work.

3.4 Location and Data

Lidar-derived snow depth data, lidar-derived canopy height models (CHMs), and meteorological data were collected from study sites in four different regions across the western United States (Figure 3.1). These sites included Olympic National Park, WA; Tuolumne River Watershed, CA; Jemez Caldera, NM; and the Boulder Creek Watershed, CO, which have different forest cover densities and tree heights (Table S3). For the four different study sites within the western United States, we specifically identified four 1000-m by 1000-m domains that were at least partly below tree line and where the topography exhibited various slope and aspects within each domain. All four sites were classified into different snow climates using the Sturm et al. (1995) classification on a 30 arcsec grid. The four sites in the Olympic Mountains were all classified as maritime. Boulder Creek had three of the four sites classified as taiga and one site classified as tundra (Devils Thumb Lake). Tuolumne had two sites classified as taiga (Dana Meadows and Dana Meadows South) and two sites classified as tundra, while sites at Jemez were all classified as warm forest. Warm forest was previously referred to as alpine in Sturm et al. (1995) and is used to describe relatively warm regions with continental precipitation, and low wind speed. While Tuolumne and Boulder Creek both contained similar snow climates, we note that the sites evaluated in Tuolumne were generally warmer, had higher incoming shortwave radiation, and were less windy than those at Boulder Creek (Figure 3.1).

Airborne lidar data

The Airborne Snow Observatory (ASO) (Painter et al., 2016) collected lidar observations in Olympic National Park, WA on 29-30 March 2016, when snow depth at Waterhole was about

92% of peak. These data were post-processed to snow depth rasters at a 3-m gridded resolution (Painter et al., 2016). In addition, ASO flew over the Tuolumne Watershed, CA on a semi-weekly basis between 26 March 2016, when snow depth at the Dana Pillow was about 80% of maximum, and 25 June 2016, when snow depth was about 2% of maximum, to provide snow depth derived rasters at 3-m resolution throughout the ablation season. We primarily show results using the 26 March 2016 data and note when discussing spatial snow depth patterns using snow depth datasets from later in the ablation season.

The National Center for Airborne Laser Mapping (NCALM) collected snow-on flights over Jemez, NM between 27 March and 3 April 2010, when the nearby Quemazon SNOTEL site showed snow depth was at 64% of peak. Furthermore, NCALM collected snow-on flights over the Boulder Creek Watershed in Colorado on 20 May 2010, when the snow depth at the Niwot SNOTEL site was at 55% of peak. For both sites, the first return lidar data and bare earth models (snow-on and snow-off) were provided at 1-m resolution and are further described in Harpold et al. (2014). Following methods in Harpold et al. (2014), snow depth rasters were derived by taking the difference between the bare earth models during the snow-on and snow-off periods.

For both NCALM and ASO data, the CHM was calculated by taking the difference between the bare earth model and a model based on first returns during the snow-off flights. Following previous studies, a binary canopy mask was derived using canopy height values that were greater than 2 m (A A Harpold et al., 2014; Tennant et al., 2017; Zheng et al., 2016). Furthermore, for all lidar datasets, any negative or zero values were removed from the analysis (Table S3). Zero snow depth values were present primarily within forested areas of the ASO lidar datasets and generally appeared to be unrealistic based on adjacent snow depth values and nearby time-lapse cameras, which showed snow underneath the canopy. Meanwhile, negative snow depth values at

Boulder Creek, CO and Jemez, NM were found in steep rocky outcrops where landslides were possible or where lidar observations are more prone to vertical errors due to slight horizontal errors (Deems et al., 2013; Hodgson et al., 2005). Furthermore, negative values existed over lakes in the NCALM data where aerial imagery showed a changing water level between the snow-on and snow-off flights. Meanwhile, lakes were removed from the ASO dataset with polygons from the National Hydrography Dataset. We note that the results were insensitive to the decision to remove zero or negative snow depth values, and in section 3.7.3, we discuss the sensitivity of our results to lidar accuracy.

Meteorological data

In Olympic National Park, the Northwest Modeling Consortium (Mass et al., 2003) provided wind speed and wind direction data from the Weather Research and Forecasting (WRF) model (Skamarock et al., 2008) for water year (WY) 2016 . Over Washington state, WRF used NCEP's Global Forecast System as lateral boundary conditions along with the Thompson microphysical scheme (Thompson et al., 2008) at a spatial resolution of 1.33 km. Similarly, in the Tuolumne Watershed, CA, WRF data were provided by Mimi Hughes at a 6-km spatial resolution using the North American regional reanalysis data for lateral boundary conditions (Mesinger et al., 2006) and the Thompson microphysical scheme during WY 2008 and 2014 (Hughes et al., 2017). Wind directions from the 6-km WRF runs in the Tuolumne Watershed were predominantly from the southwest at our study sites for both WY 2008 and 2014, and therefore we assume the predominant wind direction was consistent for WY 2016 as well. Wind speed and direction from the 6-km WRF run were also downscaled using Micromet (Liston & Elder, 2006) with a 250-m DEM and showed a negligible difference in the most frequent wind direction from the 6-km resolution at our study locations. Wind speeds and directions at the Jemez River Basin Critical

Zone Observatory in northern New Mexico were obtained from the Valles Caldera Mixed Conifer (MCon) eddy covariance tower (Ameriflux US-Vcm), while wind data for the Boulder Creek Watershed were gathered from the Niwot eddy covariance tower (Ameriflux site US-NR1). All other meteorological information is described in Table S2 (Bohn et al., 2013; Currier et al., 2017; Hughes et al., 2017; Lundquist & Huggett, 2010; Mass et al., 2003).

3.5 Methods

Classifications

In each study site, snow depth distributions within four 1000-m domains were broken into six different classifications (Figure 3.2). The six classifications included forested areas, forest edges, and exposed regions. The forest edge classification was based on the CHM, solar direction, and primary wind direction, while the length of the forest edge classification varied based on a range of literature values (Table 3.1). We defined exposed classifications as areas that were not underneath the canopy and not along the forest edge. Therefore, the fractional area of the exposed classification changes with the length of the forest-edge classification. The exposed classification was broken into two sub-classifications based on the slope with respect to the predominant wind or solar direction.

We added directionality to the forest-edge classification to test whether snow was redistributed primarily from wind or whether there were snow depth differences due to forest shading. Specifically, we classified areas within the forest-edge as directly north-facing (NFE) or leeward (LWFE) of the forest and as directly south-facing (SFE) or windward (WWFE) of the forest. All of these classifications were tested, but only the pair with the greatest difference for a location are shown, specifically, north-facing and south-facing in Tuolumne, CA and Jemez, NM, and leeward and windward in Olympic National Park, WA and at Boulder Creek, CO. The

classification labeled “overlapping forest edge (OFE)” represents grid cells where the NFE/LWFE and SFE/WWFE forest-edge classifications overlap (Figure 3.2).

The extent of the forest edge classification varied based on literature values (Table 3.1). The classification algorithm searched out from each forest grid cell (tree height >2 m) using its CHM value and selected forest-edge search distance. The algorithm classifies areas as a forest edge if the canopy height is less than 2 m and within a given forest-edge search distance. When classifications were defined based on solar direction, north-facing forest edges and south-facing forest edges were classified using forest-edge search distances of 0.5, 1, 2, and 3 H, where H is the tree height from the canopy height model. When the classifications were defined based on the predominant wind direction, the forest edges were classified using forest-edge search distances of 1, 3, 6, and 10 H because wind related deposition has a larger expected extent than forest shading (Table 3.1).

Similar to the forest edges, exposed regions were also sub-classified based on aspect. We classified exposed regions as either north-facing slopes (NSlp) or leeward slopes (LWSlp) and compared these classifications to south-facing (SSlp) or windward slopes (WWSlp). As above, all were tested, but only the pair with the greatest difference for each location are shown. Slope classifications were only determined using the slope’s aspect and not magnitude. Leeward forest edges and slopes were based on the most frequent wind direction using the nearest WRF grid cell or nearest Ameriflux tower.

Statistical Significance Tests

To test whether snow depth within the different forest-edge classifications were statistically different from one another (e.g. north-facing forest edges vs. south-facing forest edges) we used the non-parametric Wilcoxon rank-sum test (Wilcoxon, 1945), with the large sample

approximation (Helsel & Hirsch, 2002) and an alpha value of 0.05 for sample sizes greater than ten. To remove spatial autocorrelation, the classification maps and snow depth data were subsampled every 40-m (Figure 3.3).

Variogram analysis previously showed that there is a scale break in snow depth at 15-40 m (Deems et al., 2006) and in forested areas the scale break was even less (Trujillo et al., 2007, 2009). Furthermore, scale breaks were found to be consistent between years with different accumulation patterns (Deems et al., 2008) and for lidar datasets at a spatial resolution between 1.5 and 5-m (Fassnacht & Deems, 2005). Similarly, we found correlation lengths at our sites that were similar to the previously mentioned scale breaks (Figure S1), suggesting that 40-m subsampling should be sufficient to remove autocorrelation within our study sites. This was further supported by a Morans I test (Moran, 1950), which showed that subsampling these data provided a decrease in spatial autocorrelation from strong to weak (Table S1) (Griffith, 2009).

These subsampled data may not fully represent the variability captured within the domain. Therefore, we shifted the sampling locations (Figure 3.3, black squares) and repeated the Wilcoxon rank-sum test. Each shift in the sampling location was 3 m, either in latitude or longitude, resulting in potentially 169 rank-sum tests for each domain. To fulfill the large sample approximation requirement (Helsel & Hirsch, 2002), a rank-sum test was only performed when the sample size for each classification was at least 10.

3.6 Results

Boulder Creek, CO

In Boulder Creek, CO the dominant process controlling snow depth variability along the forest edge appeared to be wind related deposition (Figure 3.4, Table 3.2). Across the four sites, the median snow depth value of leeward forest edges differed the most from windward forest

edges when the forest-edge search distance was at 6H (38%). Using the 6H forest-edge search distance, the Wilcoxon rank-sum tests at three out of the four sites indicated that snow depth along leeward forest edges was statistically greater than snow depth along windward forest edges at 100% of the subsampled locations (section 3.5.2). When each 1000-m domain was classified based on solar direction, the greatest difference in snow depth between north and south-facing forest edges was when the forest-edge search distance was at 0.5 H (13%), but the differences were not statistically significant, therefore rejecting HP1 and supporting HP2.

When we compared the difference between median snow depth values for leeward and windward forest edges to the snow depth difference between leeward and windward-facing slopes, we found that the differences between slopes were greater (53%) than between forest edges (38%; Table 3.2). However, the difference between the median snow depth value for leeward and windward forest edges was greater than differences in the median snow depth value for exposed (combining leeward and windward facing slopes) and forested classifications (17%). This implies that at these locations in Boulder Creek, wind related deposition as a result of the forest has a greater influence on snow depth variability than processes controlling snow depth beneath the forest, such as forest-snow interception and subsequent sublimation.

Interestingly, we found that snow depth along leeward forest edges was greater in areas that were also on leeward slopes, superimposing the effects from the forest and topography on wind related deposition. For instance, across all four sites, the median snow depth value in areas that were both leeward of the forest edge and on leeward slopes had a 20% greater median snow depth value than leeward forest edges that were on windward slopes. However, snow depth in areas that were leeward of the forest edge and on windward slopes were still 17% greater on average than windward forest edges.

At Jasper Lake, where 75% of the subsampled snow depth values reported statistically significant differences between leeward and windward forest edges, the snow depth difference between leeward and windward forest edges was 10%. This implies that at Jasper Lake, there is more snow on leeward forest edges than windward forest edges, but it's not as substantial as it is at the other three locations within Boulder Creek, CO.

We note that when the CHM and bare earth models were gridded to 3-m spatial resolution from the original point cloud data, results were generally consistent, as there were still greater than 30% differences on average between leeward and windward forest edges. Furthermore, across all four sites, the percent difference between the median snow depth values for leeward and windward forest-edge classifications were similar when the forest-edge search distances were 3H (32%) and 10H (34%), respectively. Lastly, at Jasper and Albion Lake, leeward of ribbon forests, some snow drifts were classified as overlapping forest edges. This implied that either more detail on the forest morphology is needed to improve the classification of leeward forest edges or that drifts preferentially form in areas that are sheltered from multiple directions (see section 3.7.1).

Jemez Caldera, NM

At Jemez Caldera, NM, forest shading appeared to be the dominant process controlling snow depth variability along the forest edge (Figure 3.5; Table 3.2). Across the four sites, the median snow depth value of north-facing forest edges differed the most from south-facing forest edges when the forest-edge search distance was at 1H (32%). At all four sites, the Wilcoxon rank-sum tests for 100% of the subsampled locations indicated that snow depth along north-facing forest edges displayed statistically greater snow depth than south-facing forest edges when the forest-edge search distance was at 1H. When the forest-edge classifications were based on the most

frequent wind direction, the snow depth differences between median snow depth values for leeward and windward forest edges were less than 2% across all four forest-edge search distances, therefore rejecting HP2 and supporting HP1.

The snow depth differences between the median values for north and south-facing forest edges were generally similar to the snow depth differences between median snow depth values for north-facing and south-facing slopes (28%), which had snow depth differences that were statistically significant at all subsampled locations. Furthermore, the snow depth differences between the median values for north and south-facing forest edges were similar to the differences between the median values for exposed and forest classifications (27%). This implies that at these locations in Jemez, forest shading had a similar degree of influence on snow depth variability within the domain as did radiative differences between north and south-facing slopes or forest-snow processes affecting snow depth underneath the forest.

Similar to Boulder Creek, we found that snow depth along north-facing forest edges was greater in areas that were also north-facing slopes, superimposing the effects from the forest and topography on forest shading. For instance, on average, the median snow depth value in areas that were both in north-facing forest-edge classifications and on north-facing slopes had a 33% greater median snow depth value than north-facing forest edges that were on south-facing slopes. Meanwhile, the median snow depth values for north-facing forest edges that were on a south-facing slope were also greater than the median snow depth values for the south-facing forest edge classification using all slope aspects (23%).

Furthermore, we note that when the CHM and bare earth models were gridded to 3-m spatial resolution from the original point cloud data, results were similar. At 3-m spatial resolution, the results showed that on average there were greater than 20% differences between median snow

depth values for north and south-facing forest edges when the forest-edge search distance was 0.5 to 2 H. Lastly, across all four sites, the percent difference between the median snow depth values for north and south-facing forest-edge classifications were similar when the forest-edge search distances were of 0.5H (29%), 2H (27%), and 3H (22%), respectively.

Tuolumne River Watershed, CA

In the Tuolumne River Watershed, CA forest shading appeared to be the dominant process controlling snow depth variability. At the 2H forest-edge search distance, across all sites, the median snow depth value of the north-facing forest edge was 14% greater than the median snow depth value for south-facing forest edges. Using this classification, the Wilcoxon rank-sum tests showed statistically significant snow depth differences between north and south-facing forest edges at Dana Meadows and Dana Meadows South, where snow depth differences between median values for north-and south-facing classifications were 14% and 31%, respectively. At Lyell and Matterhorn Canyon, the subsampled snow depth differences between north and south-facing forest edges were 5% and not significant, which was likely the result of topographic shading from terrain outside the analyzed domain (see section 3.7.1).

Meanwhile, on average across all sites, the difference between median snow depth values for leeward and windward forest-edges was 8% or less depending on the forest-edge search distance. Furthermore, the Wilcoxon rank-sum tests showed that snow depth from leeward and windward classifications were not statistically different, except at Dana Meadows South. Therefore, results support HP1, specifically at Dana Meadows and Dana Meadows South, because forest-edge classifications showed greater differences than wind related deposition classifications. At both Lyell and Matterhorn Canyon results were not statistically different for either forest shading or wind related deposition classifications.

At Dana Meadows and Dana Meadows South, the snow depth differences between north and south-facing forest edges were either greater than or equal to the snow depth difference between north and south-facing slopes. However, at Lyell and Matterhorn Canyon, the greatest snow depth differences were between north and south-facing slopes. Furthermore, snow depth differences between north and south-facing forest edges were greater than or equal to snow depth differences between exposed and forested areas.

Similar to Boulder Creek, CO and Jemez Caldera, NM, we found that snow depth along the forest edge was greatest when the forest-edge aspect aligned with the slope aspect. On average, the median snow depth value in areas that were both in the north-facing forest-edge classification and on a north-facing slope had a 15% greater median snow depth value than north-facing forest edges that were on south-facing slopes. Meanwhile, the median snow depth value for north-facing forest edges that were on a south-facing slope were greater than the median snow depth value for the south-facing forest edge classification using all slope aspects (8%).

As the season progressed, the differences between north and south-facing forest edges generally remained the same for each site and there was no change in the statistical significance results. We also note that the difference between north and south-facing slopes did not change significantly throughout the melt season. Lastly, despite the results supporting HP1, we reiterate the uncertainty in the wind data described in section 3.4.ii, and therefore further discuss the results in context with the potential of a poorly resolved wind field in section 3.7.1 and 3.7.2.

Olympic National Park, WA

In Olympic National Park, WA, snow depth differences between either leeward and windward forest edges, or north and south-facing forest edges were not statistically significant (Figure 3.7). On average, the greatest snow depth differences, across the four sites, were when

the forest edges were classified based on the most frequent wind direction and the length of the forest edge was 3H. Using this classification, the snow depth difference between median values was 13% (Table 3.2). However, in the four domains, the results were not statistically significant, therefore rejecting HP1 and HP2.

In Olympic National Park, the greatest snow depth differences appeared between leeward and windward facing slopes, where on average the difference between slopes was 78%. Furthermore, the difference between snow depth in exposed and forested areas was on average 54%, indicating that processes affecting the snow depth distribution along the forest edge (Table 3.1) were not responsible for the dominant modes of heterogeneity in Olympic National Park, WA.

3.7 Discussion

Variation in Forest-Snow Processes at the Forest Edge by Study Site

At Boulder Creek, CO, we found that wind related deposition was likely the dominant process controlling snow depth variability between forest edges. We believe that snow drifts on the leeward side of the forest were due to a combination of cold mean winter temperatures (-5 – -10°C), strong winds coming from the west (>10 – 12 m s^{-1}), and the forest distribution. The Boulder Creek, CO sites contained ribbon forests (Billings, 1969; Hiemstra et al., 2002, 2006; Liston, 1999), and therefore the forests served as wind breaks (Brandle, J.R., Finch, 1991) which led to the preferential deposition of snow on the leeward side of the forest.

Interestingly, in the Olympic Mountains, WRF wind speeds at 10 m indicated wind speeds that were similar to or greater than those measured at the Boulder Creek Ameriflux Tower (Figure 3.1), even when wind speeds were filtered to snowfall events. Despite high wind speeds, the Olympic Mountains did not have statistically significant snow depth differences between

leeward and windward forest edges. In Olympic National Park, the forests were generally more continuous and did not contain ribbon forests. Furthermore, in the Olympic Mountains, the mean winter temperature was around 0°C (Figure 3.1), and the wet and heavy snowpack could generally resist scour from high winds (LaChapelle, 1958; L. Li & Pomeroy, 1997). Therefore, the snow depth differences between slope aspects, as well as the snow depth differences between exposed and forested areas, implies that snow depth variability was likely due to wind related deposition across topographic ridges during snowfall events (M. Lehning et al., 2008; Mott & Lehning, 2010) and forest-snow interception (Dickerson-Lange et al., 2017; Martin et al., 2013; Pascal Storck et al., 2002), rather than from forest shading or the forest serving as a wind break.

The snow depth data from ASO in the Olympic Mountains was collected early in the ablation season when snow depth was around 92% of peak. We therefore evaluated NAIP imagery from later in the season, and consistently found that snow was present in exposed areas but not underneath the forest or along the forest-edge. This supports conclusions from Dickerson-Lange et al. (2017), which showed that for areas similar to the Olympic Mountains, snow depth heterogeneity is primarily the result of accumulation differences (e.g. forest-snow interception) rather than ablation differences. Furthermore, this supports the conclusion that the generally cloudy conditions in the winter and spring (Figure 3.1) did not lead to radiative differences between different sides of the forest edge, and therefore there was not greater snow retention along north-facing forest edges in the Olympic Mountains (Figure 3.1).

Across all the sites, we note that a classification between leeward and windward forest edges could be improved with more detailed meteorological data and by including the length, width, and porosity of the forest patches. Previous studies suggested that when forest porosity, defined as the ratio of open area to total frontal area of the trees, becomes greater than 50%, snow will

begin to be deposited on the windward side (Tabler, 2003). Furthermore, the deposition of snow on the leeward side was more effective when the length of the forest (length perpendicular to the wind direction) was at least ten times the height of the tree (Brandle, J.R., Finch, 1991; Brandle & Nickerson, n.d.; Tabler, 2003). Lastly, consistent with previous studies, we note that leeward snow drifts generally begin several meters from the leeward edge of the forest (Hättenschwiler & Smith, 1999; Hiemstra et al., 2002, 2006; Tabler, 2003), which was reflected in the 1 H vs. 3-10H forest-edge search distances at Boulder Creek.

In Jemez, NM there were statistically significant snow depth differences at all sites between north-facing and south-facing forest edges, which was consistent with previous findings (Musselman et al., 2008; Veatch et al., 2009). At the four sites in Jemez, NM, the horizon angle was always lower than the sun's elevation angle at each daylight hour on 1 February, and therefore the sites at Jemez, NM received little topographic shading from outside the examined 1000-m domains. Interestingly, despite Jemez, NM and Tuolumne, CA differing by only two degrees in latitude and having similar monthly mean solar radiation, two of the sites in Tuolumne, CA (Lyell and Matterhorn Canyon) did not have significant differences between north and south-facing forest edges. Both Lyell and Matterhorn Canyon were surrounded by steep topography, which shaded the entire area. This likely explains the lack of significant snow depth differences between north and south-facing forest edges at these two locations. For instance, on 1 February, at Lyell and Matterhorn Canyon the sun was beneath the horizon angle 30% and 40% of the daylight hours, respectively. Meanwhile, at Dana Meadows and Dana Meadows South, the sun was beneath the horizon angle only 10% of daylight hours. This suggests that in areas with significant amounts of solar radiation, such as Tuolumne and Jemez, it is important to consider the amount of direct radiation received throughout the day while the

sun's elevation angle is still low when determining whether forest shading will cause significant snow depth variability.

In Tuolumne, CA, snow depth variability appeared to be predominantly controlled by variation in incoming radiation, but additional radiation and wind observations would better support this conclusion. For instance, the results from multiple ASO overpasses in Tuolumne suggested that snow depth distributions were primarily set up by radiative differences before 26 March 2016 and that ablation after 26 March 2016 was relatively uniform between classifications. Relatively uniform melt rates later in the season have previously been observed and explained by an increase in the solar elevation angle throughout the ablation season (Anderton et al., 2004; Egli & Jonas, 2009). Furthermore, the wind magnitudes and directions for this study site were less certain than the other three study sites (see section 3.4.2). Therefore, in Tuolumne, it is possible that forest shading and wind related deposition both have an impact on forest-edge snow depth variability because winds were likely steered through Tioga Pass and were probably predominantly from the south despite WRF indicating southwesterly flow in the lower atmosphere.

Modeling application

These results highlight forest-edge snow processes that should be resolved within high-resolution simulations. Furthermore, these results advocate that sub-element model parameterizations explore the representation of forest-edge variability within hydrologic models. We note that the variability exhibited between forest edges would not necessarily be resolved by any but the highest-resolution simulations (Broxton et al., 2015) because results suggested that slope (topographic shading and wind-induced deposition) and forest-edge snow depth variability,

which existed in the 1000-m domain, also existed with a similar magnitude in the 50-m domain (see supplemental material).

Since the variability exhibited between forest-edge classifications is significant and as great as the snow depth variability between forest and exposed classifications, which are already accounted for in many models, the results suggest that exploration of a tiling parameterization might be one solution (Figure 3.8). Within each model element, each tile could independently simulate its own snowpack drawing on physical relationships that describe forest shading (Lawler & Link, 2011; Musselman et al., 2015; Seyednasrollah & Kumar, 2014), and wind related snow deposition (Brandle, J.R., Finch, 1991; Tabler, 2003). Actual implementation of a tiling parameterization would need to be adaptable to the climatic conditions, and the classifications (north vs. south or leeward vs. wind forest edges) would need to be assigned based on the appropriate physical process (forest shading vs. wind related deposition). Therefore, the hydrologic modeler should consider the magnitude and confidence in their meteorological data (i.e. mean winter temperature, incoming solar radiation, wind speed, and wind direction) as well as the forest distribution and surrounding topography, all of which changes significantly throughout a watershed.

Furthermore, we note that substantial heterogeneity remained within each classification, especially at Boulder Creek (Figure 3.4-3.7, Table S4). While tiles could simulate the median snow depth value for each classification within a model element, each classification could also be prescribed its own sub-element probability distribution using the coefficient of variation to account for finer scale variability within the classification (Liston, 2004; Luce & Tarboton, 2004). Therefore, the representation of the forest-edge variability within sub-element

parameterizations is non-trivial and warrants further research, specifically evaluating the parameterization's effect on streamflow and land-atmospheric interactions.

Results with respect to lidar accuracy

In an exposed area with little elevation relief, ASO has been shown to have a mean absolute error of less than 8 cm and an overall bias of less than 1 cm (Painter et al., 2016). In coniferous forests, other airborne lidar data, including NCALM, have been evaluated using snow-probe transects, individual acoustic snow depth sensors, and GNSS observations to have a root-mean-square-error of 10 – 31 cm and an overall mean difference of 1 – 13 cm depending on the study and canopy cover type (A A Harpold et al., 2014; Hopkinson et al., 2004; Reutebuch et al., 2003; Tinkham et al., 2014).

We believe our results should be robust despite potential inaccuracies within forested areas, as we largely focused on areas beside but not directly underneath the canopy. Snow depth differences between median values from different forest-edge classifications resulted in snow depth differences greater than mean absolute snow depth errors found within ASO (Painter et al., 2016). At three out of the four study sites in the western United States, snow depth differences between median values from exposed and forested areas were less than potential inaccuracies of airborne lidar within forested areas (Table 3.2). However, previous studies that used acoustic snow depth sensors at these sites showed snow depth differences between exposed and forested areas of similar magnitude (Adrian A. Harpold et al., 2015; Molotch et al., 2009; Rice & Bales, 2010). To better understand the uncertainties of ASO and NCALM lidar data and to further investigate snow depth variability beneath the canopy, we advocate future studies that further evaluate the spatial patterns of ASO and NCALM lidar data within forested areas.

3.8 Conclusions

Snow depths between different sides of the forest edge were significantly different at three of the four study sites, likely due to the interaction of unique climatic conditions (i.e. mean winter temperature, incoming solar radiation, wind speed, and wind direction) experienced within the entire domain, as well as the forest distribution. In Jemez, NM and Tuolumne, CA, where there was the greatest amount of incoming solar radiation, the statistically significant snow depth differences between the north and south-facing forest edges were likely the result of forest shading, specifically in areas where there was no topographic shading from the surrounding terrain. In the relatively cold and windy environment of Boulder Creek, wind related deposition and the presence of "ribbon forests," which served as wind breaks, likely influenced the statistically significant snow depth differences between leeward and windward forest edges. Meanwhile, in the relatively warm, cloudy, and windy Olympic Mountains, where there was a more continuous forest distribution and snow was more resistant to scouring due to the maritime environment, snow depth differences were not statistically significant between either north and south-facing or leeward and windward forest edges.

Forest-edges contain unique physical snow processes that result in statistically significant snow depth differences between different forest-edge classifications. The snow depth differences between forest-edge classifications were equal to or greater than the snow depth differences between exposed and forested classifications at Jemez, NM; Tuolumne, CA; and Boulder Creek, CO. The significant variability in snow depth at the forest edge justifies further exploration of sub-element model parameterizations to represent forest-edge snow depth variability and evaluate how those parameterizations affect model representations of late-season streamflow and land-atmospheric interactions. Future sub-element modeling parametrizations that account for

forest-edge snow depth distributions should consider the interaction between meteorological conditions, topography, and the forest distribution, all of which change throughout the watershed.

3.9 Tables

Table 3.1 Expected Extents of Forest-edge Processes

Forest-edge process	**Expected extent of the process**	**Citation**
Forest Shading	0.5-2 H	(Golding & Swanson, 1978; Lawler & Link, 2011; Musselman et al., 2015; Seyednasrollah & Kumar, 2014)
Enhanced longwave radiation from the forest	1-2 m or 0.5 H	(Lawler & Link, 2011; Musselman & Pomeroy, 2017; Seyednasrollah & Kumar, 2014; Webster et al., 2016; Woo & Giesbrecht, 2000)
Wind related deposition as a result of the forest	5-100 m or 3-10 H	(Brandle, J.R., Finch, 1991; Hiemstra et al., 2002, 2006; Tabler, 2003)

Table 3.2 Median Snow Depth Differences

Study site	(HP1) North vs. south[a] forest-edge difference [cm/%]	(HP2) Leeward vs. windward[b] forest-edge difference [cm/%]	North vs. south slope difference [cm/%]	Leeward vs. windward slope difference [cm/%]	Exposed vs. forested difference [cm/%]
Boulder Creek, CO *(0.5 H^a and 6 H^b)*	18 13%	57 38%$^+$	26 17%	87 53%$^+$	32 17%$^+$
Jemez, NM *(1 H^a and 1 H^b)*	31 32%$^+$	1 2%	19 28%$^+$	6 8%	19 29%$^+$
Tuolumne, CA* *(2 H^a and 1 H^b)*	21 14%	13 8%	32 19%$^+$	19 12%$^+$	25 16%
Olympic Mountains, WA *(0.5 H^a and 3 H^b)*	22 11%	29 13%	93 48%$^+$	148 81%$^+$	126 55%$^+$

The snow depth difference or percent differences between median values for different forest-edge classifications, slope classifications, and between exposed and forested areas. The mean difference from the four domains within each different study site was reported. See Figures 3.4-3.7 for snow depth differences per 1000-m domain and for each classification's snow depth value. Percent differences were normalized by the median snow depth value for the entire domain.

***** Results between north and south-facing forest edges were statistically significant at two of the four locations. The other two locations were shaded by the surrounding topography – see section 3.7.1 for more details.

$^+$ The snow depth differences between classifications were statistically significant. See text for more details.

[a] North and south-facing forest-edge search distances that provided the greatest difference in median snow depth values.

[b] Leeward and windward forest-edge search distances that provided the greatest difference in median snow depth values.

Table 3.3: Spatial autocorrelation is reduced for each domain and within each climate as Moran's Index is reduced with 40-m subsampling of the 1 or 3-m snow depth data.

Moran's Index					
Olympic National Park, WA	**Site Name**	**Waterhole**	**Hurricane Ridge**	**Mount Hopper**	**Anderson Pass**
	All Data Points	0.67	0.61	0.78	0.82
	40-m Subsampled Data Points	0.27	0.20	0.28	0.31
Tuolumne, CA	**Site Name**	**Dana Meadows**	**Dana Meadows South**	**Lyell Canyon**	**Matterhorn Canyon**
	All Data Points	0.76	0.75	0.80	0.87
	40-m Subsampled Data Points	0.21	0.12	0.30	0.28
Boulder Creek, CO	**Site Name**	**Jasper Lake**	**Devils Thumb Lake**	**Diamond Lake Trail**	**Albion Lake**
	All Data Points	0.90	0.96	0.96	0.91
	40-m Subsampled Data Points	0.20	0.30	0.44	0.31
Jemez, NM	**Site Name**	**Ameriflux Tower**	**Cerro del Medio Peak**	**Ameriflux North East**	**Caldera Valley**
	All Data Points	0.80	0.91	0.83	0.84
	40-m Subsampled Data Points	0.22	0.19	0.28	0.30

Table 3.4: Source of meteorological data for the most frequent wind direction and for display in Figure 3.1. To be consistent between climates, shortwave and longwave radiation were derived using MTCLIM with methods described in Bohn et al. (2013).

	Olympic National Park, WA	Tuolumne, CA	Boulder Creek, CO	Jemez, NM
Water Year	2016	2016	2011	2011
Snow Depth	Waterhole SNOTEL Site	CDWR Dana Snow Depth Sensor	Niwot SNOTEL Site	Quemazon SNTOEL Site
Relative Humidity (RH)	Waterhole SNOTEL Site	HOBO U23 Pro v2 at Dana Meadows -following methods of Lundquist & Huggett, (2010)	Niwot eddy covariance tower (Ameriflux site US-NR1)	Valles Caldera eddy covariance tower (Ameriflux US-Vcm)
Temperature	Waterhole SNOTEL site – corrected for using Currier et al. (2017)	HOBO U23 Pro v2 at Dana Meadows – following methods of Lundquist & Huggett, (2010)	Niwot eddy covariance tower (Ameriflux site US-NR1)	Valles Caldera eddy covariance tower (Ameriflux US-Vcm)
Longwave Radiation (LW)	MTCLIM (Bohn et al., 2013)	MTCLIM (Bohn et al., 2013)	MTCLIM (Bohn et al., 2013)	MTCLIM (Bohn et al., 2013)
Shortwave Radiation (SW)	MTCLIM (Bohn et al., 2013)	MTCLIM (Bohn et al., 2013)	MTCLIM (Bohn et al., 2013)	MTCLIM (Bohn et al., 2013)
Wind Speed & Wind Direction	Nearest WRF Grid Cell (Mass et al., 2003; Skamarock et al., 2008)	Nearest WRF Grid Cell (Hughes et al., 2017; Skamarock et al., 2008)	Niwot eddy covariance tower (Ameriflux site US-NR1)	Valles Caldera eddy covariance tower (Ameriflux US-Vcm)

Table 3.5: Average fractional forest cover within 1000-m domains, average tree height within 1-km domains, average percent of 1000-m domains that contains negative values (removed from the analysis), average percent of 1000-m domains that contains zero values (removed from the analysis). Negative snow depth values were not prevalent in ASO datasets due to a relative registration step that matched elevations of snow-free areas in both snow-on and snow-off data sets

Climatic Region	Average Forest Cover [%]	Average Tree Height [m]	Average Number of Negative Values [%]	Average Number of Zero Values [%]
Olympic National Park, WA	56.7	8.1	0.0	12.7
Tuolumne, CA	48.9	5.5	0.0	3.4
Boulder Creek, CO	24.0	6.7	5.0	0.0
Jemez, NM	38.9	9.4	2.5	0.0

Table 3.6: The mean and range of the coefficient of variation from the four 1-km domains for each classification within different regions of the western United States. In Tuolumne, CA and Jemez, NM, classifications were based on forest-shading and used tree height search distances of 2H and 1H, respectively. Olympic National Park, WA and Boulder Creek, CO had classifications based on wind related deposition and used tree height search distances of 3H and 6H, respectively.

Coefficient of Variation	**North-facing Slope**	**North-facing Forest Edge**	**South-facing Forest Edge**	**South-facing Slope**	**Underneath the Canopy**	**Overlapping Forest Edge**
Tuolumne, CA	0.28 0.14 – 0.47	0.31 0.21 – 0.37	0.32 0.25 – 0.40	0.33 0.16 – 0.53	0.55 0.50 – 0.61	0.30 0.27 – 0.34
Jemez, NM	0.17 0.16 – 0.18	0.28 0.23 – 0.40	0.42 0.34 – 0.63	0.26 0.18 – 0.32	0.37 0.29 – 0.49	0.31 0.25 – 0.44
	Leeward-facing Slope	**Leeward-facing Forest Edge**	**Windward-facing Forest Edge**	**Windward-facing Slope**	**Underneath the Canopy**	**Overlapping Forest Edge**
Olympic National Park, WA	0.25 0.23 – 0.30	0.39 0.29 – 0.44	0.42 0.27 – 0.47	0.59 0.25 – 0.94	0.73 0.62 – 0.87	0.47 0.39 – 0.51
Boulder Creek, CO	1.03 0.55 – 2.13	0.62 0.40 – 0.87	0.70 0.47 – 1.10	2.03 1.23 – 2.90	0.38 0.30 – 0.52	0.44 0.34 – 0.60

3.10 Figures

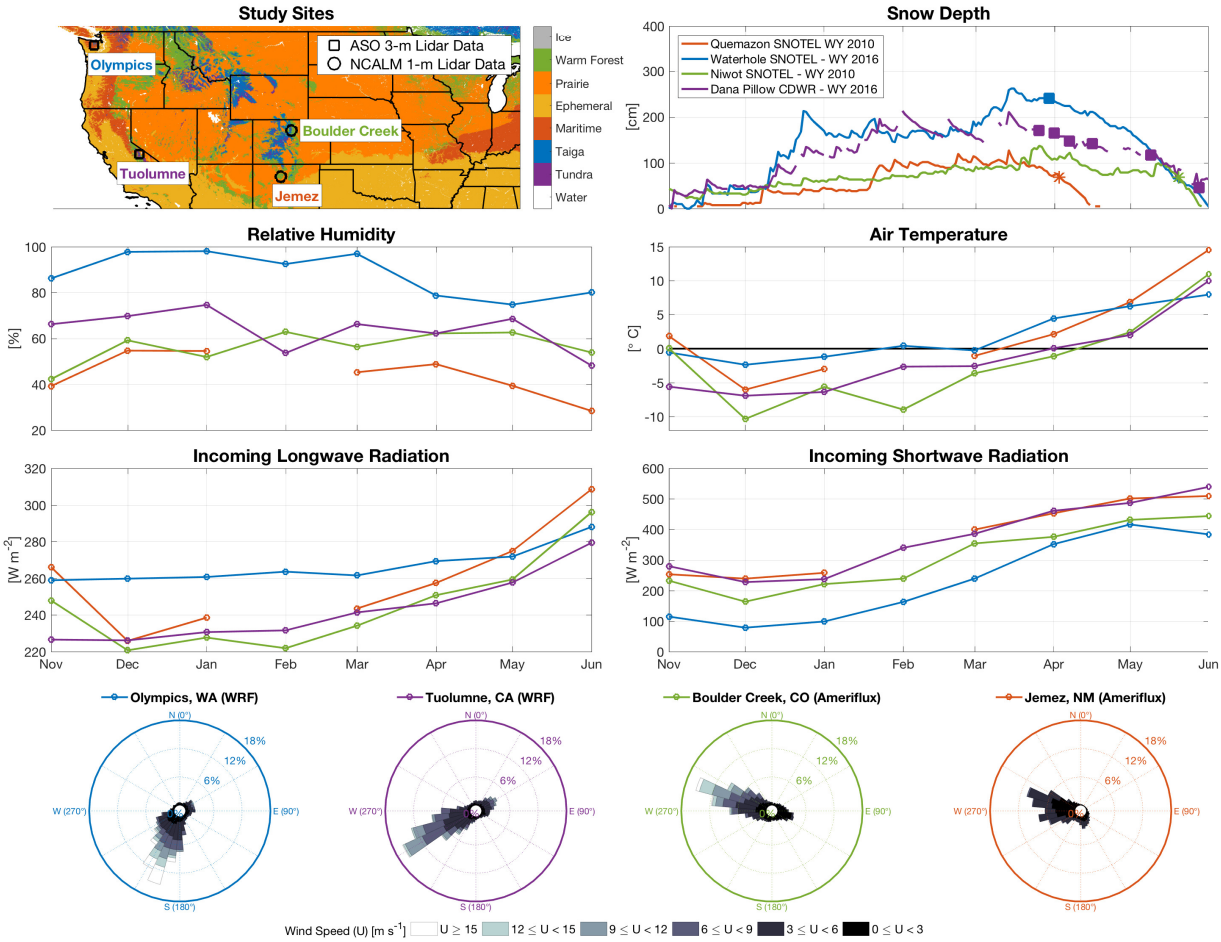

Figure 3.1 Location of NCALM and ASO lidar datasets within different snow climates as classified by Sturm et al. (1995). Monthly averages of meteorological variables as described in the text and Table S2. Wind roses for the Olympics and Tuolumne are shown as an example for the nearest WRF grid cells to the Waterhole SNOTEL site and CDWR Dana Pillow, respectively. Daily snow depth data is from the SNOTEL and CDWR snow pillow sites. A marker is used to represent the date of the lidar acquisition. Missing temperature and relative humidity data were prevalent at Jemez, NM in February and was not filled in. This limited the derivation of longwave and shortwave radiation

.

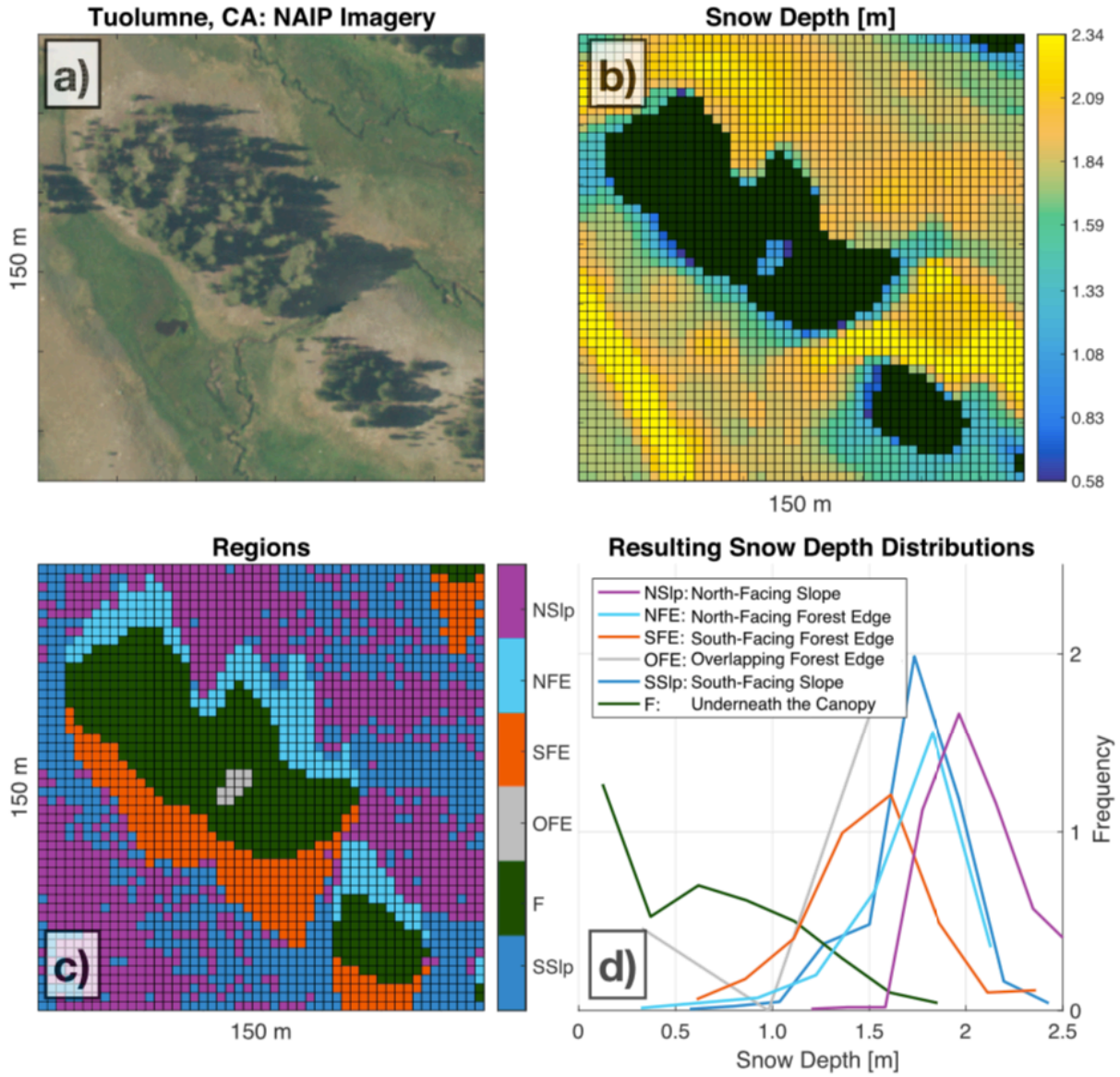

Figure 3.2 a.) Aerial image from the National Agriculture Imagery Program (NAIP) on 25 June 2016 in Dana Meadows, Tuolumne River Watershed, CA. b.) Gridded snow depth (3 m) from ASO. Dark green shading represents trees. c.) Classification of regions within a 150-m domain based on the CHM and DEM. The length of the forest edge was at 3 H. Acronyms of each region are defined in the histogram's legend. d.) Snow depth distributions for the six classifications.

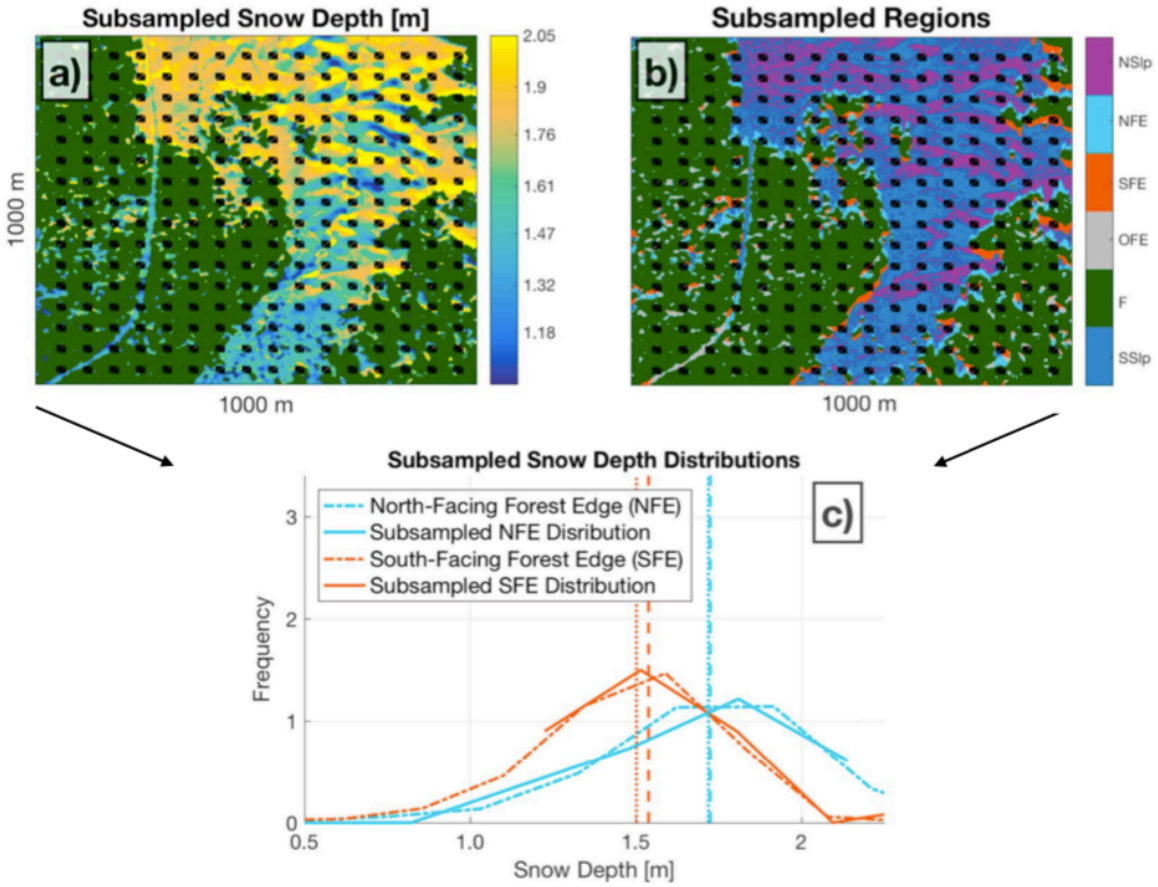

Figure 3.3 a-b.) An example of removing spatial autocorrelation through subsampling (black squares) to perform a hypothesis test between independent snow depth samples in Dana Meadows, CA on 26 March 2016. Green shading represents forested areas in a) and b). Acronyms for each classification are defined in Figure 3.2d. c.) Subsampling changed the sample size of the snow depth distribution for north-facing forest edges from 3899 to 25, and the median value (vertical lines) did not change. Subsampling changed the sample size of the snow depth distribution for south-facing forest edges from 3469 to 23, and the median values changed from 150 cm to 154 cm.

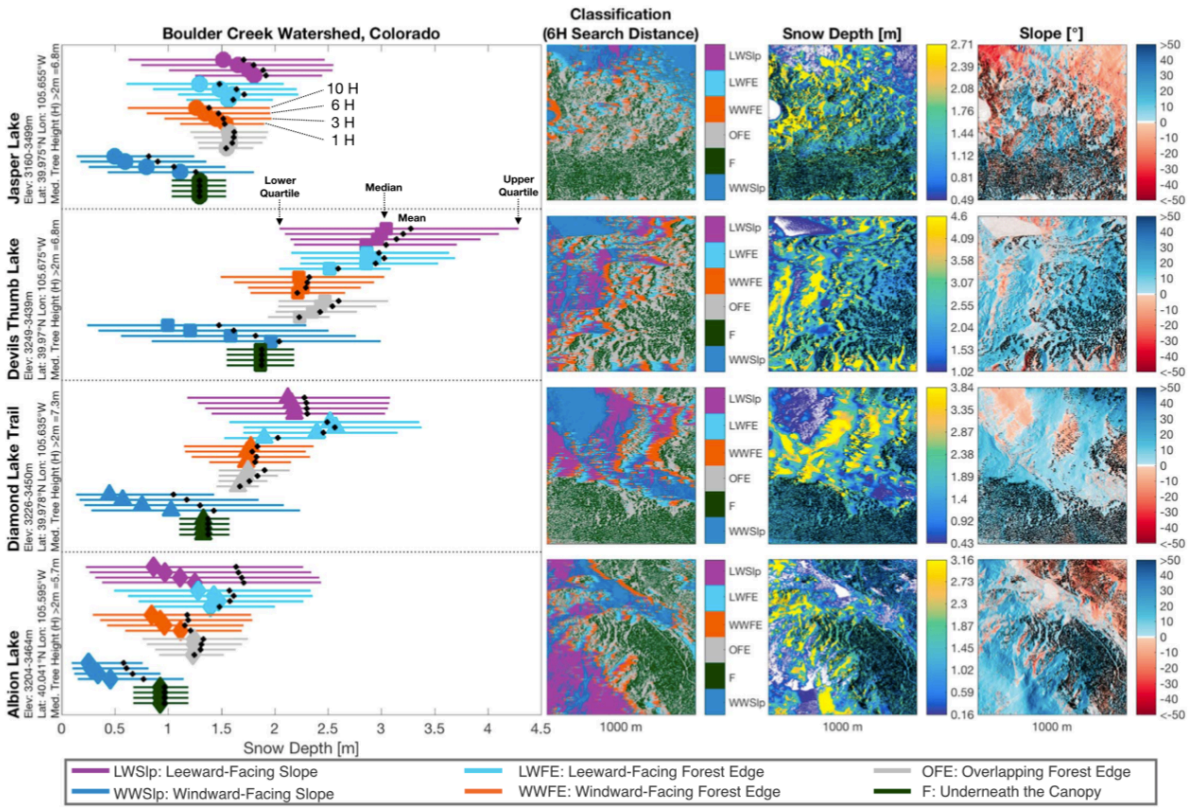

Figure 3.4 Snow depth distributions in the Boulder Creek Watershed, CO using four different forest-edge search distances (1, 3, 6, 10 H) at four different 1000-m domains. The canopy mask (black) is draped over the snow depth and slope maps for each domain to show how the slope and snow depth vary with respect to the forest. Latitude and longitude are for the center point of the domain. Each dot and line plot represent the median, mean, and interquartile range for a given forest-edge search distance classification in a specific domain. Forest-edge search distances increase along the y-axis.

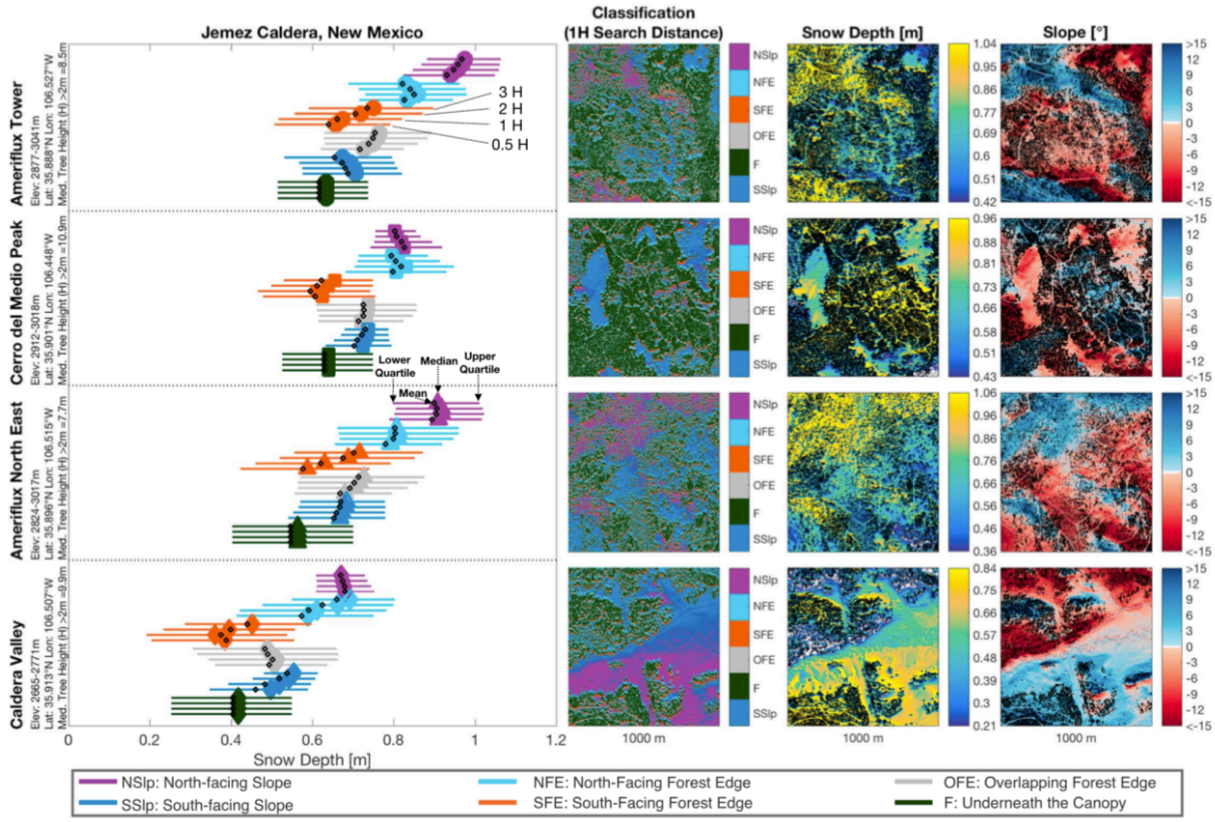

Figure 3.5 Snow depth distributions as the result of four different forest-edge search distances (0.5, 1, 2, and 3H) in Jemez, NM at for four different 1000-m domains. See Figure 3.4 for more information.

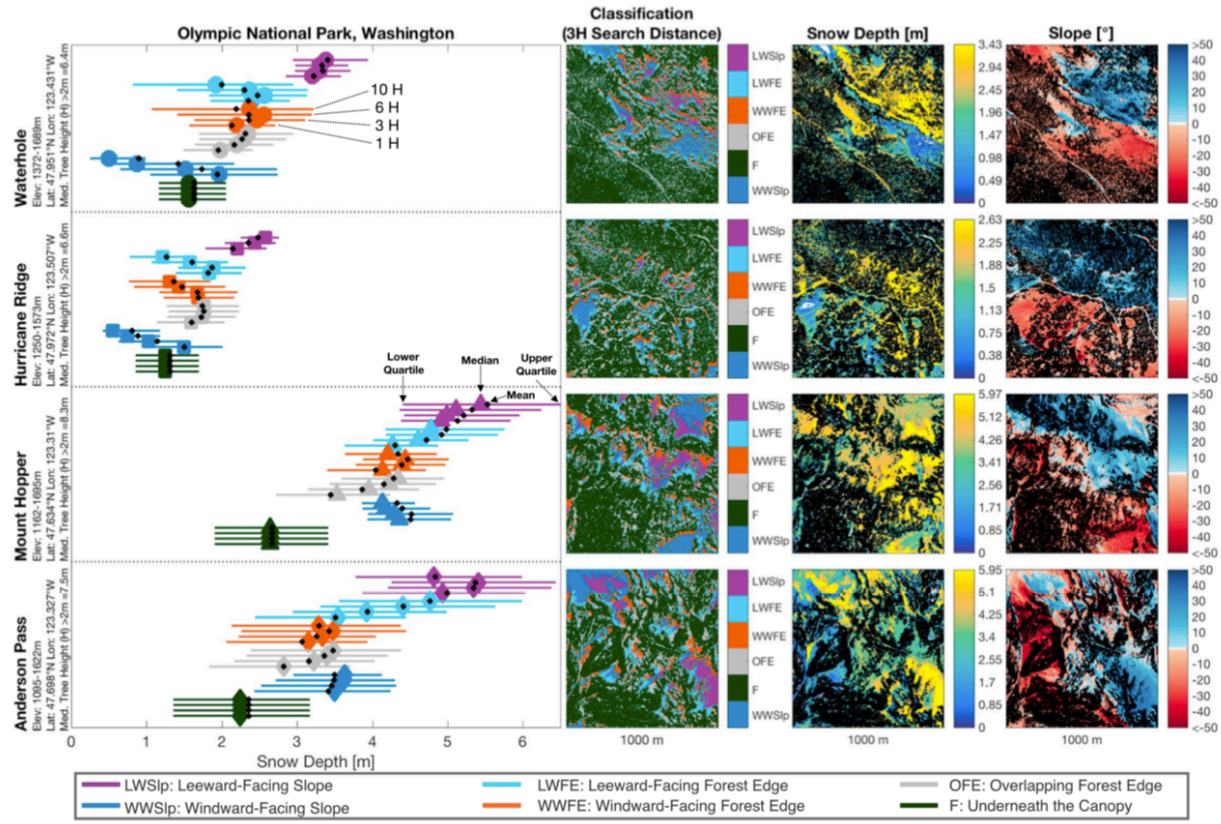

Figure 3.6 Snow depth distributions as the result of four different forest-edge search distances (0.5, 1, 2, and 3H) in Tuolumne, CA at four different 1000-m domains. See Figure 3.4 for more information.

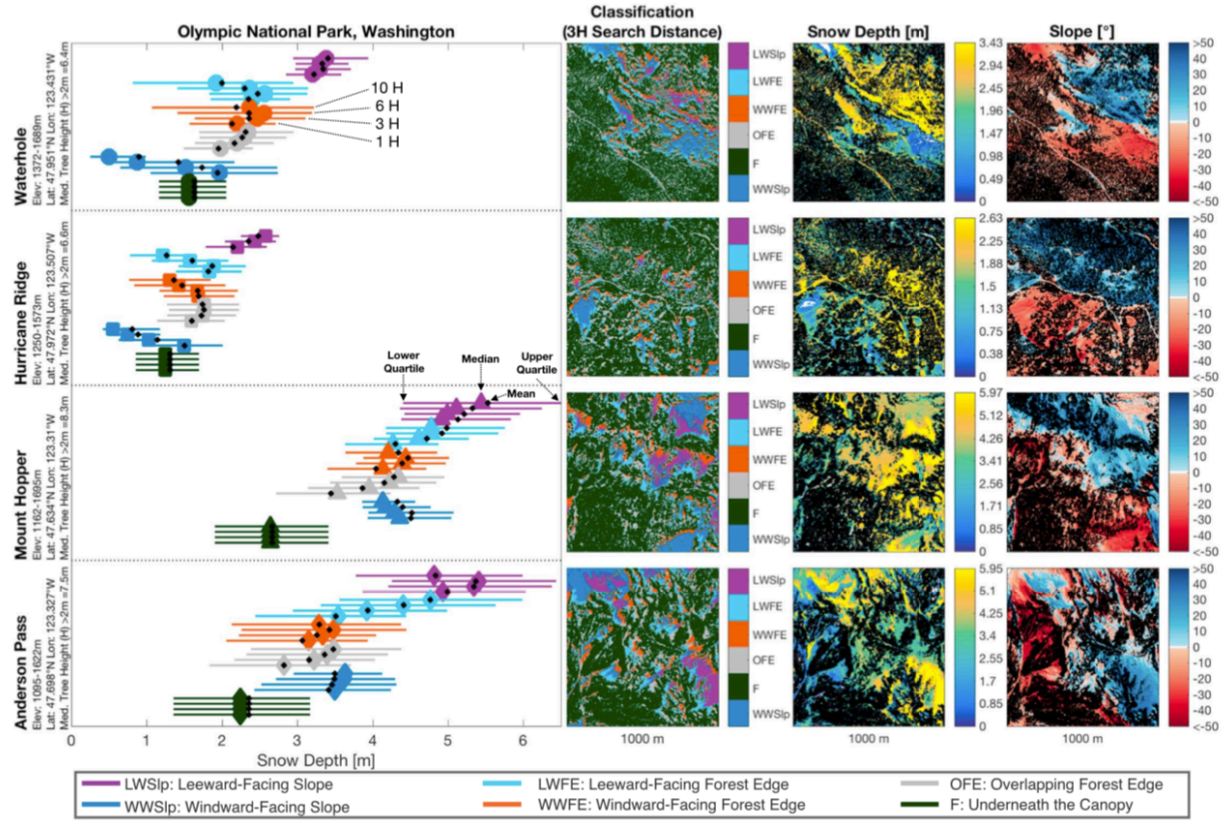

Figure 3.7 Snow depth distributions as the result of four different forest-edge search distances (1, 3, 6, and 10H) in Olympic National Park, WA at four different 1000-m domains. See Figure 3.4 for more information.

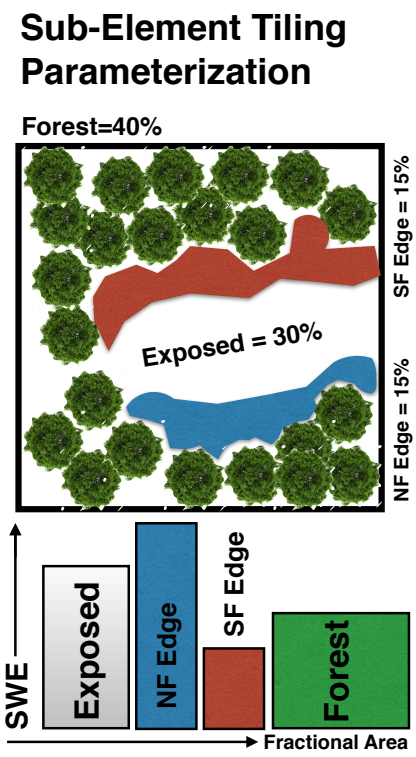

Figure 3.8 Conceptual diagram for a tiling approach to model forest-edge snow depth variability within a model element. In this diagram the model element is represented as a grid cell, and each classification could independently simulate its own mass and energy fluxes while total melt could be weighted by each classification's fractional area.

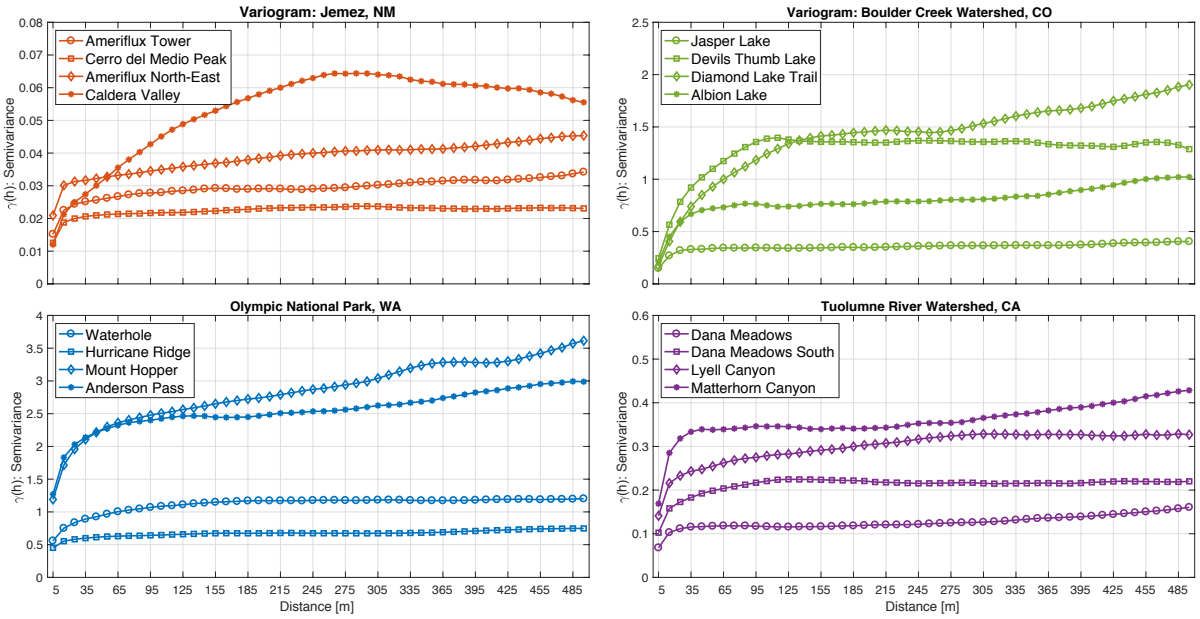

Figure 3.9 Snow depth variograms for each snow climate and each 1000-m domain using 10-m bin widths. The correlation length was estimated to be the distance where the semivariance reaches around 95% of the sill, or where the semivariance begins to no longer increase with distance.

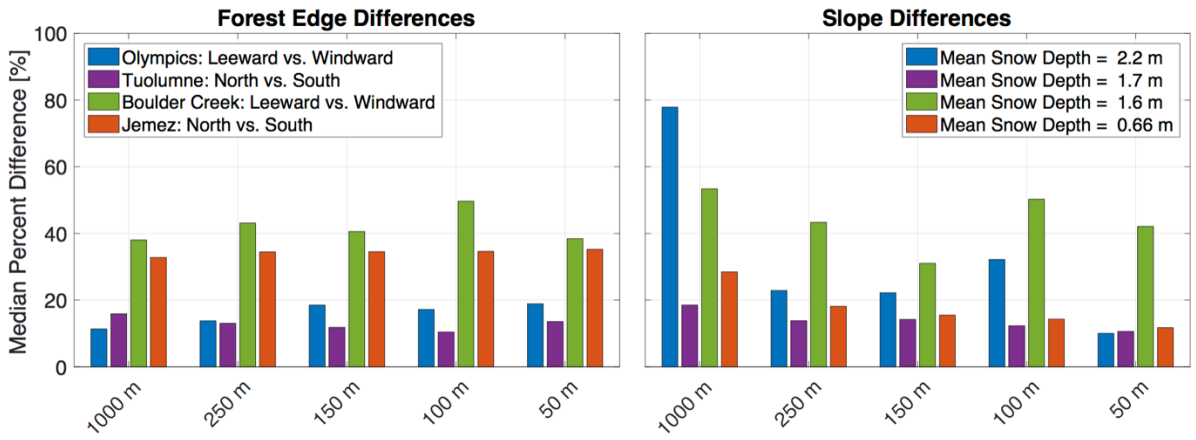

Figure 3.10 Median percent snow depth differences between the forest-edge and slope aspect at the four different regions in the western United States as a function of the analyses areal extent (See Text S2 for a more thorough explanation). In the Olympics, Tuolumne, Boulder Creek, and Jemez the forest-edge search distance classification was at 1, 2, 6, and 3H, respectively. The direction of the forest-edge classification is noted in the legend. Mean snow depths are shown to provide insight into what the median percent difference is with respect to snow depth differences.

3.11 Appendix A: Spatial autocorrelation

Spatial autocorrelation exists when values similar in space are more similar to one another than values farther apart. Moran's Index (Moran, 1950) is a measure of spatial autocorrelation that varies from negative one to positive one. Values of positive one indicate positive spatial autocorrelation. Positive autocorrelation is when similar values are clumped together within the domain. Negative one indicates data that has high values located closely to low values. Zero indicates that the values are randomly distributed and thus completely independent from one another. In general, values of 0.25 to 0.5 indicate weak spatial autocorrelation, 0.5 to 0.7 indicate a moderate spatial autocorrelation, 0.7 to 0.9 indicates a strong spatial autocorrelation and values of 0.9 to 1.0 denote a substantial amount of spatial autocorrelation (Griffith, 2009).

The high-resolution, non-subsampled snow depth data showed strong spatial autocorrelation according to Moran's Index (Table S1) (Griffith, 2009; Moran, 1950). In this study, Moran's Index was calculated using ArcMap's Spatial Autocorrelation (Global Moran's I) tool with all data points and the 40-m gridded subsample of the data points (Table S1). An inverse-distance-weight-matrix was used with a Euclidean distance method. The data were not row standardized.

Variogram's were computed using 10-m bin widths for distances between 10 and 500 m and were used to define the process scale (Figure S1) (Blöschl, 1999; Deems et al., 2006). Here, the process scale is the length at which various fluxes of mass and energy influence the snow depth. On a variogram the process scale is the region where the variance is increasing with distance. The correlation length is the distance at which the variance no longer increases with distance. Using log-log variograms this distance is referred to as a scale break. Values at distances less than the correlation length were interpreted to be spatially autocorrelated and thus subject to the

same process, while values at distances greater than the correlation length were interpreted to be uncorrelated or independent from one another.

Previous work has identified the scale break for snow depth at several sites in Colorado to be 40-m or less (Deems et al., 2006, 2008) and in forested areas the scale break to be even less (Trujillo et al., 2007, 2009), suggesting that the 40-m subsampling was sufficient. The Devils Thumb Lake and Diamond Lake Trail sites at Boulder Creek and the Caldera Valley site at Jemez all showed a larger correlation length than 40 m while the remaining sites showed correlation lengths of 40-m or less (Figure S1). This was due to processes within those particular domains that acted on a larger scale. For instance, at the Caldera Valley site in Jemez, NM there is a distinct north vs. south pattern within the snow depth data (Figure 3.7). We suspect that this is due to the differences in slope and thus differences in direct incoming shortwave radiation causing variation in ablation.

In places where the dominant processes act at larger scales than 40-m, the results from hypothesis tests that used the 40-m subsampling should be interpreted carefully. For instance, at Caldera Valley samples on north-facing and south-facing slopes may not be independent because at this site, the process scale is larger. However, subsampling at 40-m for different forest edges leads to independent sampling because forest shading has an expected extent less than 40-m (Table 3.1).

At sites where the variogram suggests that the process scale was larger than 40-m we decided to report the statistical significance tests for differences between slopes using 40-m subsampling because subsampling for all sites decreased Moran's Index values from strong spatial autocorrelation to weak spatial autocorrelation (Table S1) (Griffith, 2009). Furthermore, at sites with larger process scales, statistical significance tests were in agreement with the other sites that

had a smaller correlation length. In addition, at Devils Thumb Lake, Diamond Lake Trail, and Caldera Valley where it is subjective whether 40-m subsampling leads to independent observations within different slopes, the snow depth distributions between different slope aspects visually look different and differ by more than 27% (Figure 3.4 & 3.5).

3.12 Appendix B: Sensitivity to the areal extent of the analysis

To determine whether snow depth variability between forest edge and slope classifications existed within smaller areal extents, we repeated the snow depth comparisons by separating the 1000-m by 1000-m snow depth rasters into smaller areal extents. In addition, we also separated the corresponding classification maps into smaller areal extents. Specifically, we separated the 1000-m domain into 4 (250-m), 36 (150-m), 100 (100-m), and 400 (50-m) individual square domains. For clarity, we outline our analysis using the 150-m areal extents at Jemez with a forest-edge search distance of 1H as an example.

Within each of the 36, 150-m areal extents, we computed the percent difference between the median snow depth value for north and south-facing forest edge classifications (with the requirement that at least 5% of the area fell into each classification to ensure reasonable sample size). The mean of the percent differences between median snow depth values from each classification within the 36, 150-m domains was then computed, and the same analysis was repeated for the three other sites at Jemez. To report the general difference between north and south-facing forest edges at Jemez within the smaller areal extent, we then averaged and reported the mean percent differences between median snow depth values from north and south-facing forest edges.

This analysis was repeated for the other areal extents and for other classification-pairs (such as slope-aspect within exposed areas). For simplicity, we only report the results from the forest-edge search distance that showed the greatest difference in median snow depth values between forest edge classifications from the 1000-m analysis.

We found that when we separated the 1000-m domain into 4 (250-m), 36 (150-m), 100 (100-m), and 400 (50-m) individual square domains that the snow depth differences between

classifications were generally consistent despite changes to the areal extent (Figure S2). For instance, at Boulder Creek, CO, across all four sites, the 6H forest-edge search distance on average showed a 38% difference between the median snow depth value along leeward and windward forest edges (Table 3.2; Figure S2). Meanwhile, the snow depth difference between windward and leeward slope classifications was on average was 53% (Table 3.2; Figure S2). As the analysis was performed on smaller areal extents the average differences between forest edges and slopes remained around 38% and 53% for snow depth differences between forest edges and slopes, respectively. Similar results were also true for Jemez, NM and Tuolumne, CA. In Olympic National Park, WA there was generally little difference in snow depth between leeward and windward forest edges. However, there was an 81% snow depth difference between median values for leeward and windward slopes. At smaller areal extents the snow depth difference between leeward and windward slopes decreased to less than 35%.

Chapter 4 Explicit representation of radiation in forests affects simulated snow water equivalent and streamflow depending on forest characteristics.

William Ryan Currier[1], Ning Sun[2], Mark Wigmosta[1,2], Nicoleta Cristea[1], and Jessica D. Lundquist[1]

[1]Department of Civil and Environmental Engineering, University of Washington, Seattle, WA, USA
[2]Hydrology Technical Group, Pacific Northwest National Laboratory, Richland, WA 99352, USA

4.1 Abstract

At hillslope scales, significant spatial variability in snow depth occurs at forest edges, and between exposed and forested areas. To account for this variability, a tiling parameterization, which simulates four snowpacks (one per tile) per grid cell, each drive by their own unique radiation conditions, was incorporated into the Distributed Hydrologic and Soil Vegetation Model (DHSVM). The impact of the tiling parameterization on simulated snow water equivalent (SWE) and streamflow was examined in three watersheds and was based on classifications from high-resolution (1-3 m) vegetation maps. In Tuolumne, CA, the tile model had little effect on grid-cell average SWE and streamflow. In Jemez, NM, where forests are relatively sparse and trees were 10.2 m tall, the tile model's grid-cell average snow disappearance date (SDD) was 12 days earlier and peak streamflow occurred 20-days earlier than the original (single snowpack per grid cell) model formulation. In Chiwawa, WA, where forests were dense and trees were 17.2 m tall, SDD was 11 days later and streamflow increased up to 11-13% between mid-July and August. Despite statistically different snow depth distributions, forest edges had a relatively small effect on simulating streamflow (2-6%) due to small contributing areas. However, grid cell average ablation rates and streamflow were primarily impacted by exposed and forest tiles. The contrasting responses between watersheds were primarily controlled by the grid cells average fractional forest cover and the forest's radiation attenuation, which is a function of tree height and the sun's elevation angle. Lastly, the response to tiled grid cells highlighted nonlinear responses in SWE and streamflow to forest-snow interactions.

4.2 Introduction:

Snow depth variability at the hillslope scale (Clark et al., 2011) affects watershed scale processes, such as streamflow timing, magnitude, and temperature (Leach & Moore, 2014; Luce et al., 1998, 1999; Lundquist et al., 2005; Lundquist & Dettinger, 2005; Sun et al., 2018). Additionally, snow depth variability can drive ecological processes (Carlson et al., 2015; Dedieu et al., 2016; Ford et al., 2013; Hättenschwiler & Smith, 1999), and affect land-atmospheric feedbacks (Liston, 1999, 2004).

The spatial distribution of trees within a forest affects the spatial distribution of snow in a variety of climates (Church, 1933; Currier & Lundquist, 2018; Dickerson-Lange et al., 2015, 2017; Hiemstra et al., 2006; Lundquist et al., 2013; Mazzotti et al., 2019; Moeser et al., 2016; Musselman et al., 2008; Sun et al., 2018). Across multiple climates, significant hillslope scale spatial variability in snow depth occurs at forest edges (depending on orientation), and between exposed and forested areas (Broxton et al., 2015; Currier & Lundquist, 2018; Hiemstra et al., 2006). This small scale variability between forest edges is driven largely by differences in the amounts of shortwave and longwave radiation received between exposed and forested areas, or the orientation of forest edges (Golding & Swanson, 1978; Lawler & Link, 2011; Musselman et al., 2008, 2015; Musselman & Pomeroy, 2017; Seyednasrollah & Kumar, 2014; Webster et al., 2016, 2017; Woo & Giesbrecht, 2000).

Historically, even spatially distributed hydrologic models that implicitly represent forest characteristics and their effect on radiation have not resolved forest-edge snow processes. For instance, it is common to linearly scale a vegetation characteristic (e.g. LAI) with the fractional representation of the forest and other landcover types to represent the average magnitude of a physical process (e.g. canopy radiation attenuation) over the entire model element. At grid cell

resolutions larger than 10 m, the forest distributions impact on fine-scale variability, specifically at forest edges, begins to disappear causing less simulated snow water equivalent (SWE) and less snowmelt (Broxton et al., 2015).

In this study we present a method that explicitly accounts for differences in radiation between north and south-facing forest edges, as well as between exposed and forested areas, within grid cells of a distributed model applied at the watershed scale. To explicitly resolve forest-edge snow processes, we used high-resolution (1-3 m) vegetation maps to identify the fractional area of each tile within 90-150 m grid cells. Separate tiles were used to represent forest and exposed areas, as well as north and south-facing forest edges in each grid cell (Figure 4.1; Currier & Lundquist, 2018). Fractional area maps were used as input data for the tiling parameterization incorporated into the Distributed Hydrologic and Soil Vegetation Model (DHSVM) (Wigmosta et al., 1994, 2002). DHSVM was adapted to explicitly simulate radiation differences and unique individual snowpack's for north and south-facing edges, as well as exposed and forested areas (Figure 4.1).

We first compared simulated SWE to lidar-derived SWE in each tile. We then quantified the effect that the tile parameterization has on grid cell average SWE, evapotranspiration, and streamflow, compared to the implicit, forest-radiation parameterization within the non-tiled version of DHSVM, which uses a single snowpack per grid cell. This comparison was done for three different watersheds with different forest characteristics and meteorological conditions. We therefore determined the impact that simulated forest-edge snow depth variability has on streamflow and determined what forest characteristics controlled the response of SWE and streamflow within different watersheds.

4.3 Location and Data

Site overview

We chose three watersheds for our study that had publicly available lidar data and differed in forest characteristics, meteorological conditions, and elevation distributions (Figure 4.2; Table 4.1). The Upper Tuolumne contains primarily lodgepole pine (*Pinus contorta*) and generally has the shortest trees. The forest cover is less than half the watershed, as the watershed is mostly above tree line. The Jemez contains a variety of different tree species such as, Douglas fir (*Pseudotsuga menziesii*), white fir (*Abies concolor*), blue spruce (*Picea pungens*), limber pine (*Pinus flexilis*) and ponderosa pine (*Pinus ponderosa*). The trees in the Jemez were less dense than in the Upper Tuolumne and generally more dispersed. Furthermore, the Jemez received the highest amounts of incoming radiation throughout the winter (Table 4.1). Lastly, the Chiwawa received the least amount of incoming shortwave radiation and primarily consists of grand fir (*Abies grandis*) at low elevations and subalpine firs (Abies lasiocarpa) at high elevations. The Chiwawa had the densest and tallest canopy, with the greatest spatial coverage in forests (Table 4.1).

Model Input Data

4.3.2.i Upper Tuolumne River Watershed, CA, USA

Precipitation data were collected using methods described in (Lundquist et al., 2016). Missing air temperature data after July 11, 2015 at Dana Meadows CDEC were filled in using the average of two coincidently located HOBO temperature sensors. Relative humidity data were provided from the Dana Meadows CDEC tower. Shortwave and longwave radiation were provided from the CUES met tower that is 36-km south of Dana Meadows (Bair et al., 2018). Other methods were explored, such as MTCLIM (Bohn et al., 2013), or using observed

shortwave and empirically derived longwave radiation (Lundquist et al., 2016), but CUES data produced the best simulations.

Precipitation data from Dana Meadows were distributed throughout the watershed using 800-m PRISM data (Daly et al., 2008). Temperature data were lapsed with elevation by -6.5°C km^{-1}. Shortwave radiation data were topographically corrected for slope, aspect, and terrain shading within DHSVM. Incoming longwave radiation was temporally variable, but assumed uniform throughout the basin. Wind speeds were from observations at the Dana Meadows CDEC tower and uniformly distributed. Maps describing the vegetation type were provided from lidar data (Painter et al., 2016), and NLCD landcover classifications (Homer et al., 2015) (section 4.3.4). Model runs were between water year (WY) 2014 and 2017 at a 150-m spatial resolution and a 1-hr time step.

4.3.2.ii Jemez River Watershed, NM, USA

Model forcing data were provided from archived 13-year (WY 2001-2013) WRF runs at 4-km spatial resolution (Liu et al., 2017). WRF precipitation data were adjusted to properly simulate SWE at the Quemazon SNOTEL site (Figure 4.2). Precipitation multipliers were applied to individual snowfall events until the positive cumulative increase in modeled SWE matched the positive cumulative increase in observed SWE at the SNOTEL sites. Precipitation multipliers were applied to the rest of the domain. Adjusted winter precipitation data from WRF runs between WY 2008-2010 were on average 6.5% too high (entire WY 16%) compared to observations at the three SNOTEL sites and a USCRN gauge, but this is within the realm of uncertainty as winter precipitation data is notoriously difficult to measure (Goodison et al., 1998; Rasmussen et al., 2012).

The center of each WRF grid cell was input into DHSVM as a station, where precipitation data were further interpolated between WRF grid cells using PRISM. Temperature data were scaled by -6.5°C km^{-1} with elevation between WRF grid nodes. Maps describing the vegetation type were provided from lidar data (Harpold et al., 2014), NAIP imagery, and NLCD landcover classifications (section 4.3.4.). The model was run between WY 2005 and 2010 at a 150-m spatial resolution and a 1-hr time step.

4.3.2.iii Chiwawa Watershed, WA, USA

Model input data and configurations were consistent with (Sun et al., 2018), except for the vegetation maps. Vegetation maps were derived from NAIP imagery, NLCD landcover types, and lidar data where it was available (section 4.3.4). Model forcing data were provided from (Livneh et al., 2013). The model was run between WY 2008 and 2013 at a 90-m spatial resolution and a 3-hr time step to be consistent with (Sun et al., 2018).

Measured Snow Depth and Streamflow

Distributed snow depth data were derived from lidar data in the Upper Tuolumne at 3-m spatial resolution (Painter et al., 2016), and in a subset of the Jemez River Watershed at 1-m spatial resolution (Harpold et al., 2014) (Figure 4.2). Similar data were not available for the Chiwawa Basin. Lidar-derived snow depth generally has errors less than 10-cm (Painter et al., 2016) and the errors in the forest were comparable to errors in exposed areas (Currier et al., 2019; Mazzotti et al., 2019). DHSVM simulated SWE and does not directly simulate density or depth. Therefore, density was derived using methods in (Matthew Sturm et al., 2010) in combination with (M. Sturm et al., 1995). Additional SWE observations exist at snow pillows in all three basins (Figure 4.2). Snow pillows were used for model calibration in exposed regions (section 4.4.2.).

USGS stream gauge data were provided from the Jemez River Near Jemez, NM (USGS 08324000) gauge and the Chiwawa River Near Plain, WA (USGS 12456500). Streamflow data in the Upper Tuolumne were provided from (Lundquist et al., 2016) where we primarily focused on the Highway 120 gauge. Streamflow observations in Tuolumne experienced ice jams, which caused water to pond above the gauge, causing unrealistic observations of streamflow. We therefore only show observations and compute evaluation metrics from peak SWE until the end of the water year. Lastly, in the Jemez River Watershed, two Ameriflux Towers exist, which have observations of evapotranspiration. In WY 2010, towers were missing between 46-49% of the data from throughout the water year. Therefore, observations should be considered a low estimate of evapotranspiration.

Vegetation maps

Within each watershed, lidar-derived canopy height data were primarily used to classify north and south-facing forest edges. In the Jemez River and Chiwawa watershed, lidar data were only available over a subset of the watershed (Figure 4.2). In areas where lidar data were not available, canopy grid cells were identified using NDVI calculations from 4-band NAIP imagery at 1-m spatial resolution (Figure 4.3). Canopy grid cells were identified when the NDVI was greater than a threshold value, which was optimized based on a threshold value which showed the greatest agreement with the lidar-derived canopy mask (Figure 4.3). We chose a NDVI threshold of 0.27 and 0.02 in the Jemez and Chiwawa, respectively. Differences in NDVI thresholds were likely due to a combination of differences in species type (section 4.3.1.), plant health, and differences in the forest understory or amount of mosses and twigs within the trees (Huemmrich & Goward, 1997; Xiao & McPherson, 2005).

NDVI-derived canopy masks were classified into north and south-facing edges using methods described in (Currier & Lundquist, 2018). Search distances were based on tree height. Where canopy height data was not available, the average tree height from the lidar domain was uniformly used. Forest-edge search distances were 1 H, 2 H, and 1 H for the Jemez, Upper Tuolumne, and Chiwawa, respectively, where H represents the grid-cells tree height. Search distances were based on results from (Currier & Lundquist, 2018), which showed the greatest snow depth difference between north and south-facing edges was 1 H and 2 H for the Jemez and Upper Tuolumne, respectively. 1 H was chosen for the Chiwawa. Overlapping forest edge classifications (Currier & Lundquist, 2018), or areas that were classified as both north and south-facing edges were classified as exposed grid cells based on visual inspection of lidar-derived snow depth data. Overlapping areas showed both relatively low snow depths on the south side of the trees and areas of higher snow depth on the north side. Therefore, on average, overlapping areas showed values closer to what was represented in exposed areas.

The high-resolution classification map (1-3 m) were re-gridded to the model resolution (90-150 m) to create four unique maps. Each map represented the grid cell's fractional area that was exposed, forest, north, and south-facing edges. The sum of all four maps was equal to one.

Identifying canopy grid cells from NAIP imagery was particularly problematic in riparian areas or alpine areas that were noticeably green after snow melt. These areas had high NDVI values but did not contain vegetation greater than 2 m (Figure 4.3). To filter out these areas we used the NLCD 2011 vegetation classifications to identify areas where the NAIP to NDVI method misclassified areas as being a canopy grid cell. Therefore, if the NLCD 2011 map was not a mixed deciduous, evergreen, or mixed forest, the fractional exposed map was set equal to one (fractional forest, north, and south-facing maps were equal to zero). Lastly, if the fractional

forest area was greater than zero, the vegetation classification was relabeled an evergreen forest for simplicity.

4.4 Methods

Model Description

The DHSVM simulates SWE within a grid using a two-layer energy and mass balance snow model, which explicitly accounts for topography and vegetation cover (Wigmosta et al., 1994, 2002), typically at grid cell scale of 30-150 m. In grid cells with a canopy, the DHSVM simulates forest-snow interception, sublimation, mass release, and melt with a one-layer mass- and energy balance canopy model (P. Storck, 2000; Pascal Storck et al., 2002; Wigmosta et al., 1994, 2002). Transpiration is simulated with a Penman Monteith approach where canopy resistances in the overstory are calculated based on a function of temperature, vapor pressure, photosynthetically active radiation, and soil moisture (Monteith, 1965; Wigmosta et al., 1994). The DHSVM allows saturated subsurface flow to be transported to neighboring grid cells based on lateral saturated hydraulic conductivity and a decay coefficient to represent the exponential decrease in transmissivity with depth. For more details on additional processes and those described above see (Wigmosta et al., 1994, 2002).

Model Calibration and Baseline Simulations

The original version of DHSVM was manually calibrated, individually, at the three sites to provide plausible simulations of SWE and streamflow for three water years. The DHSVM was first run to simulate SWE at snow pillow locations within the basin (Figure 4.2; Figure 4.4, Table 4.2) and then at all grid cells within the basin to compare with LiDAR data when available (Table 4.2). Trade-offs were made to optimize simulated SWE. For instance, SWE in the Upper

Tuolumne was generally too low in comparison to the Dana Meadows snow pillow (12.8%), but simulated basin-average SWE was too high in comparison to lidar-derived SWE observations.

Nash Sutcliffe's Efficiency (NSE) metric was computed using daily values during the snow melt pulse (Figure 4.4, Table 4.2). NSE's were considered poor at the Jemez River Near Jemez gauge. The Jemez River Watershed is particularly difficult to simulate as roughly 90% of the precipitation is lost to evapotranspiration (Chang et al., 2014; Sanford & Selnick, 2013) making any errors in evapotranspiration translate into relatively high errors in simulated streamflow. Furthermore, ~8% of the annual streamflow was lost to inter-basin watershed diversions and withdrawals from agriculture (Fischer & Borland, 1983). Given reasonable precipitation data from WRF (section 4.3.2.ii), vegetation and soil parameters were adjusted to simulate a reasonable magnitude of evapotranspiration and streamflow. We found that in general, adjusting albedo or vegetation characteristics that control the net radiation at the snow surface in the forest we were unable to simultaneously simulate the timing of the snow melt pulse and provide reasonable comparisons to peak SWE at SNOTEL sites and lidar-derived, basin average SWE. Despite these efforts, streamflow simulations in the Jemez should primarily be considered with respect to baseline simulations rather than observations.

Radiation Balance

4.4.3.i Original Model

In the original framework of DHSVM, net shortwave radiation at the snow/soil surface for a grid cell with an overstory, is calculated as follows:

$$SW_{net}^{under} = (1-\alpha) * \left(SW_{in}\,(1-F) + F\left(SW_{dir}\tau + SW_{diff}\tau_d\right)\right) \quad (1)$$

where incoming shortwave radiation is partitioned into direct and diffuse components, SW_{dir} and SW_{diff}, respectively. The radiation partitioning is based on regression coefficients and a ratio

between the incoming atmospheric shortwave radiation and the solar constant. *F* is the fractional forest cover parameter, which varies spatially based on the derived maps (Figure 4.2, Section 4.3.4.). Furthermore, α, is the snowpack, or understory vegetation albedo. τ is the canopy transmittance coefficient for direct radiation, and τ_d is the overstory's transmittance coefficient for diffuse radiation. τ_d is a input parameter that varies based on vegetation type, while τ is calculated based on tree height (*H*), the sun's elevation angle (*el*), and an extinction coefficient (*k*) that is an input parameter which can vary monthly and by vegetation type.

$$\tau = \exp\left(\frac{-k * H}{\sin(el)}\right) \tag{2}$$

Outgoing and incoming longwave radiation for a grid cell with a canopy is calculated for the understory as follows:

$$L_{out}^{under} = \sigma {T_{srf}}^4 \tag{3}$$

$$L_{in}^{under} = L_d(1 - F) + \sigma {T_{can}}^4 F \tag{4}$$

where L_d, is the incoming atmospheric longwave radiation, σ is the Stefan-Boltzmann constant, T_{can} is the canopy temperature, which comes from the air temperature, and T_{srf}, is the snow or soil temperature. When calculating incoming longwave radiation using the improved radiation scheme within the DHSVM, *F* is converted to a view factor, *Vf*, where *Vf* is *F* multiplied by a canopy view adjustment factor. The canopy view adjustment factor is a calibration parameter to represent the sky view factor. In the case where there is no overstory, the incoming longwave for the understory is L_d.

Net radiation is calculated as

$$Net\ Rad = SW_{net}^{under} + L_{in}^{under} - L_{out}^{under} \tag{5}$$

Therefore, for a grid cell that has a canopy, radiation variability within a DHSVM grid cell, is a weighted average between radiation in an exposed area and radiation underneath the forest, where the weights per grid cell are based on the fractional forest cover parameter, F. Note that albedo, which is a function of snow surface temperature and the days since snowfall, is not a weighted average based on F as there is a single snowpack that evolves per grid cell.

4.4.3.ii Tile Model

Within the tile model, net shortwave radiation for the north and south-facing edges, as well as the forest and exposed areas is modeled as follows:

$$SW_{net}^{nf} = (1 - \alpha^{nf}) * \left(SW_{dir}\tau + SW_{diff}\tau_{nf}\right) \quad (7)$$

$$SW_{net}^{sf} = (1 - \alpha^{sf}) * \left(SW_{dir} + SW_{diff}\tau_{sf}\right) \quad (8)$$

$$SW_{net}^{Forest} = (1 - \alpha^{Forest}) * \left(SW_{dir}\tau + SW_{diff}\tau_{d}\right) \quad (9)$$

$$SW_{net}^{Exposed} = (1 - \alpha^{Exposed}) * SW_{in} \quad (10)$$

where τ_{nf} and τ_{sf} are model input parameters, which were both set to 0.75 in this study to represent that 75% of the diffuse radiation is incident at the snow/soil surface. Net shortwave radiation for the forest (9) and exposed (10) are based on exposed and forest components from equation (1) (Figure 4.5). Net shortwave radiation for the north edge is attenuated similar to the forest (9) but has different attenuation of diffuse radiation. Net shortwave radiation at the south-facing edge received non-attenuated direct solar radiation, but the diffuse radiation is partially attenuated by the forest (Figure 4.5).

Outgoing longwave radiation for all tiles is modeled identical to equation (3). Incoming longwave radiation for the forest and exposed regions is modeled identical to equation (4), where the F is equal to 1 for the forest tile and in the exposed tile F is equal 0. Incoming longwave radiation at north and south-facing forest edges is calculated similar to equations 3-4, but instead

F is replaced by an additional input parameter, F_{xf}. F_{xf} weights the magnitude to which the forest edge receives longwave radiation from the forest and the atmosphere.

$$L_{in}^{xf} = L_d\left(1 - F_{xf}\right) + L_{out}^{over} F_{xf} \quad (6)$$

where xf represents either the north-facing (nf), or south-facing (sf) edge.

Note that each model has its own snowpack that evolves independently and therefore albedo, surface temperature, and pack temperature, evolve independently as well. The radiation balance in the tile model is therefore independent of the F parameter. In the forest tile's longwave calculation, F is still used but is set to one and scaled by the canopy view adjustment factor to represent air space within the canopy. Therefore, for a tile model that only contains exposed and forest areas, the grid cell average incoming shortwave radiation and longwave radiation is the same as the original model.

Model parameters, k, F_{sf}, F_{nf} and the canopy view adjustment factor were all adjusted in the Jemez and Tuolumne so that simulations from the calibrated model would match the mean lidar-derived SWE for each tile within a grid cell (Table 4.3). For instance, using the high-resolution classification within a grid cell, we calculated the mean lidar-derived SWE for the north-facing edge to compare with the simulated north-facing SWE at a particular grid cell. For both the Jemez and Tuolumne, we chose four different model grid cells to adjust the parameters. In the Tuolumne, we used multiple lidar flights to look at observed and simulated SWE throughout the ablation season and near peak SWE. In the Chiwawa, we use model parameters from both Tuolumne and the Jemez, as we do not have lidar-derived SWE observations in the Chiwawa (Table 4.3).

Mass Balance

In the tile model, the forest tile is the only tile where canopy snow interception is simulated. Canopy snow interception for the forest tile is consistent with the original DHSVM framework and is described in (P. Storck, 2000) and (Wigmosta et al., 2002). In the tile model the *F* parameter was again set to one to ensure that the tile model has the same fraction of precipitation intercepted throughout the grid cell as the original model.

Since each tile evolves its own independent snowpack, each tile melts out at a different time, therefore each tile simulates evapotranspiration, using a Penman-Monteith approach (Monteith, 1965; Wigmosta et al., 1994, 2002), when snow is absent in the tile. After evapotranspiration is calculated for each snow-free tile, each tiles flux of evapotranspiration, snowmelt, and soil moisture are aggregated based on a weighted average within the grid cell. Grid cell average snowmelt is added to total surface water input, which infiltrates into the grid cell average soil reservoir using methods described in (Wigmosta et al., 1994). At the start of the next time step, each layer of each tile's soil moisture reservoir is reset based on the grid-cell average soil moisture for each soil layer.

Comparison Metrics

To compare melt out dates between grid-cell average SWE in the tile and original model as well as in-between different tiles, we compute the snow disappearance date for when 90% of the original models peak SWE disappeared, referred to as SDD_{90}. For instance, if the original model simulated 0.6 m of SWE, then the snow disappearance date would be determined based on when there was 0.04 m of SWE left for the tile model, or original model. SDD_{90} was used because the north-facing edge typically melts out the latest, causing the tile's grid cell average SWE snow disappearance date to be later than the original model even if the north-facing edge accounts for 1% of the grid cell.

4.5 Results

Effects on Grid-Cell Average SWE

In the Upper Tuolumne, the tile model had little effect on grid cell average SWE (Figure 4.6). For instance, at Dana Meadows, SDD_{90} differed by 1 day between grid cell average SWE from the tile model and the original model. At Dana Meadows, the greatest difference in SWE was between the exposed and forest tiles near peak SWE. Furthermore, the observations and model both showed that the north-facing edge had more SWE than the south-facing edge, but both of these simulated SWE that fell in-between forest and exposed SWE. The south-facing edge melted out more quickly than the other tiles and SDD_{90} is 9 days earlier than the tile model's grid cell average SWE (Figure 4.6). At Dana Meadows, the forest, exposed, and north-facing edges all experience similar ablation rates (Figure 4.7). However, because the forest tile accumulated less SWE as a result of snow interception, the forest had a SDD_{90} 4 days before the tile model's grid cell average SDD_{90}, while the exposed and north-facing edge both had a SDD_{90} that was two days after the tile model's grid cell average SDD_{90}. Across all forest grid cells, the south-facing edge melted out the quickest followed by the forest, north-facing edge, and exposed tile.

In the Jemez, the tile model increased grid-cell average ablation (Figure 4.7) as a result of relatively high ablation rates in the south-facing and exposed tiles (Figure 4.7). At a grid cell near the Mixed Conifer Ameriflux Tower, the tile model's grid cell average SDD_{90} was 12 days earlier than the original model's SDD_{90}. In the Jemez, the greatest difference in SWE was between north and south-facing edges. The north-facing edge contained the highest peak SWE and had a SDD_{90} 12 days after the tile models grid cell average SDD_{90}. Despite snow lasting longer on the north-facing edges, snow melt was accelerated with respect to the original model

due to relatively high net radiation values in exposed and south-facing edges, which resulted in relatively high ablation rates (Figure 4.7).

In the Chiwawa, the new tile model parameters derived for the Upper Tuolumne, rather than the model parameters from the Jemez, had the greatest effect on grid cell average SWE primarily to due to the choice in *k*. In the Chiwawa, using the Upper Tuolumne parameters, the ablation rate of the grid cell average SWE was reduced relative to the original model. For instance, the tile model's grid cell average SWE had a SDD_{90} 11 days after the original model. Similar to the Jemez, the exposed and south-facing tiles had the highest ablation rates and experienced the greatest amount of net radiation. The Chiwawa contained the highest tree heights on average (Table 4.1), which directly lead to high shortwave radiation attenuation and low ablation rates for north-facing and forest tiles (Figure 4.7).

Effects on Streamflow

In Tuolumne, there was little difference in streamflow between the tile model and the original model (Figure 4.8). The greatest percent difference occurred during the beginning of the rising limb and towards the end of the recession limb, when streamflow was relatively low. For instance, in a normal snow year (WY 2016), 10-day average streamflow increased 19% between April 3 and May 13. Between peak streamflow, which occurred between May 13 and July 12, 2016, there was a 1% decrease in 10-day average streamflow. Lastly, during the recession limb of the hydrograph, between July 22 and August 11, 2016 when streamflow decreased, there was an 8% increase in 10-day average streamflow. Similar patterns of changes in 10-day average streamflow with the hydrograph occurred in a low snow year (WY 2015) and in a high-snow year (WY 2017) (Figure 4.8).

In the Jemez, where snowmelt was accelerated using the tile model, there were major changes in streamflow between the tile mode and the original model (Figure 4.8). In all water years, the rising limb of the hydrograph occurred earlier, and in WY 2008 and 2010 peak 10-day average streamflow occurred 20-days earlier. As a result of earlier snow melt with the tile model, in April 2010, 10-day average streamflow with the tile model was on average 105% greater than the original model, but in May and early June streamflow was 41% less on average. Furthermore, this increased the NSE to 0.48 from -0.56 as the timing of peak streamflow better reflected the observed streamflow. Similar increases in NSE for the tile model were found in WY 2008 and 2009 (Figure 4.8), but NSE, were still generally poor for both the original and tile model.

In the Chiwawa, during the rising limb and near peak streamflow, streamflow was generally lower using the tile model. Streamflow during the recession limb was then increased. On average the tile model decreased streamflow by 2%, 6%, and 4% in April, May, and June, but increased late-season streamflow by 3, 8, and 9% in July, August, and September. The greatest increases in 10-day average streamflow using the tile model occurred in WY 2012, where 10-day average streamflow increased between 11-13% between July 22 and the end of August.

Evapotranspiration and total streamflow

Differences between simulations of total annual evapotranspiration and streamflow did not have a major effect between the original model and the tile model in all watersheds (Figure 4.9). In Tuolumne, during WY 2014, 2015, and 2016, the original DHSVM simulated ET/P ratios of 62%, 35%, and 19%, respectively. Evapotranspiration rates were generally consistent at around 325 mm $year^{-1}$, while precipitation amounts changed per year (Table 4.1). Using the tile model, DHSVM simulated 6%, 3%, and 2% less evapotranspiration than the original model in WY

2014, 2015, and 2016, respectively. The tile model simulated 7%, 2%, and 1% more streamflow than the original model, in WY 2014, 2015, and 2016, respectively.

In the Jemez, between WY 2008 and 2010, ET/P ratios were relatively consistent and on average 92% and 90% for the original model and tile model, respectively. Using the tile model, DHSVM simulated 2-3% less evapotranspiration than the original model on average between WY 2008 and 2010. Due to the relatively low streamflow magnitudes, the tile model simulated 5-25% more streamflow than the original model but the difference in magnitude of annual streamflow was only between 3-9 mm (Figure 4.9).

In the Chiwawa, between WY 2011 and 2013, ET/P ratios were relatively consistent and on average, 25% and 24% for the original model and tile model, respectively. Using the tile model, the DHSVM simulated 4-6% more evapotranspiration than the original model on average between WY 2011 and 2013. Lastly, the tile model simulated 2-3% less streamflow than the original model (Figure 4.9).

4.6 Discussion

Effect of forest edges on streamflow

To quantify the effect that forest edges have on streamflow, we ran the tile version of DHSVM with the same model parameters as before, but for each grid cell we incorporated the fractional area that north and south-facing edges represent into the exposed area (Figure 4.10). Therefore, these simulations only contain exposed and forested tiles but differ from the original model in that two independent snowpack's evolve as a result of radiation differences between exposed and forested areas (Figure 4.10). In all watersheds, we found that the tile model without forest edges, when compared to the original model showed similar results to those presented in section 4.5 (Figure 4.11).

In Tuolumne, the tile model without forest edges produces similar results, but with less of an increase in early season streamflow (Figure 4.11). For instance, during the rising limb of the hydrograph, between April 3 and May 13, 2016, 10-day average streamflow only increased 14% on average compared to the baseline simulation, relative to the tile model with forest edges that increased 10-day average streamflow 19%. Similarly, there was a 1-day difference in SDD_{90} between the original model and tile models grid cell average SWE, which is consistent with what we found when the tiles contained forest edges.

In the Jemez, when compared to the original model, the tile model without forest edges produced nearly identical results to the tile model with forest edges (Figure 4.11). For instance, the tile model without forest edges still shifts the timing of peak 10-day average streamflow 20 days earlier than the original model. Furthermore, in April 2010, 10-day average streamflow increased 99% on average, instead of 105%, compared to the baseline simulation. Lastly, in the Chiwawa, the tile model without forest edges increased late-season streamflow by 2%, 6%, and 7% in July, August, and September, compared to a 3%, 8% and, 9% with the tile model that contained forest edges.

Therefore, despite statistically different snow depth distributions (Currier & Lundquist, 2018) and differences in snow date disappearance between different tiles, forest edges generally increased the rising limb's streamflow by 5% and 6% in the Tuolumne and Jemez, respectively. Meanwhile in the Chiwawa, forest edges increased late-season streamflow by 2%. This was likely controlled by the forest edges' relatively low contributing area (Table 4.1) and because ablation rates between north and south-facing edges counteracted each other.

As a result, radiation differences at forest edges had a small effect on simulated streamflow. However, tiles that explicitly represent radiation differences between exposed and forested areas

did affect grid cell average ablation rates and streamflow in all watersheds. Therefore, using the fractional forest cover as a weight to average radiation between exposed and forested areas (equation 1 & 4) did not result in the same grid cell average SWE or streamflow than a model that partitions the radiation and simulates independent snowpack's, each with their own surface temperature, pack temperature, and albedo.

These effects on simulated SWE and streamflow highlight that forest-snow interactions are nonlinear. For instance, a nonlinear process with the model is the albedo scheme, which switches from an accumulation parameterization to a melting parameterization depending on whether the surface temperature is at 0°C or not. Furthermore, by separating the forest and exposed areas, interception only happens in the forest tile, causing less accumulation of SWE and less cold content in the forest. Due to dynamic changes in meteorological conditions, forest-snow interception, albedo, pack temperature, and surface temperature, it was difficult to quantify individual effects of all non-linear responses. We therefore highlight that linearly scaling a vegetation characteristic (e.g. *F*) to represent the grid-cell-average radiation does not result in a linear response in streamflow and SWE.

Forest characteristics effect response in SWE and streamflow to tiling

The impact that the tile model had on streamflow and grid-cell average SWE between watersheds was a function of the basin-average tree height, the watershed's latitude, the grid cells average fractional forest area, and the forest edges total contributing area.

Simulations in the Chiwawa, which used a tree height of 8.3 m (height of the trees in Tuolumne) instead of 17.2 m showed that grid cell average SDD_{90} was only 4 days later than the original model instead of 11 days later. Similarly, late-season streamflow only increased by up to 4% instead of 12%. While vegetation parameters controlling the radiation were consistent

between Tuolumne and the Chiwawa after changing the vegetation height, the Chiwawa's forest tile, still melted out slower in comparison to basin average SWE than it did in Tuolumne. This was controlled by the sun's elevation angle, which is lower at higher latitudes. The lower elevation angle decreased τ (equation 2) and therefore incoming shortwave radiation was attenuated more in the Chiwawa than the Tuolumne for the same tree height. In combination with a relatively high latitude and tall trees, the Chiwawa was 87% forested with a high forest density per grid cell. Therefore, the high radiation attenuation in the forest was the dominating effect, increasing late-season streamflow and decreasing ablation rates. Additionally, the north-facing edge, while a small contributing area (2%), did delay snow melt and contribute to the increase in late-season streamflow.

Simulations in the Jemez, which used a tree height of 17.2 m (height of the trees in the Chiwawa) instead of 10.2 m showed that grid-cell-average SDD_{90} was only 6 days earlier than the original model instead of 12 days earlier due to slower ablation rates in the forest from higher radiation attenuation. Furthermore, streamflow was still accelerated due to the low forest density and peak streamflow was still 20 days earlier although peak streamflow was decreased. For instance, compared to the original model streamflow in April 2010 increased 35% with 17.2 m tall trees compared to 105% when trees were 10.2 m. The average forest grid cell fraction that was forested was 57%, implying that in the Jemez, a significant fraction of the NLCD 2011 forest grid cells are actually exposed. Within exposed and south-facing edges, net radiation was much greater (Figure 4.5) and caused the snowpack to become isothermal more quickly and melt sooner.

Meanwhile, in the Tuolumne, there was little difference in SDD_{90} between the original model and the tile model. The response in streamflow was similar to the Jemez in that streamflow

increased during the rising limb even though streamflow magnitudes were relatively small. In the Upper Tuolumne, the average forest grid cell fraction that was forested was 70% (Table 4.1), which is a forest density in-between the Tuolumne and Chiwawa. Furthermore, in Tuolumne, 45% of the watershed was forested, with relatively small tree heights (Table 4.1). Despite smaller trees than the Jemez, the *k* value from model calibration was higher than the Jemez, which caused for the radiation attenuation in the forest to be higher in the Tuolumne than the Jemez. Therefore, tree heights, in combination with the extinction coefficient parameter *k*, and the average fractional forest coverage lead to a dampened response to the tile parameter than the Jemez. Furthermore, there was less forest cover in Tuolumne than the Jemez.

Future Work

Forest-edge longwave radiation values were tuned primarily based on F_{sf} and F_{nf} until SWE simulations for north and south-facing edges matched lidar-derived SWE observations. In both the Jemez and Tuolumne, the F_{sf} parameter was less than the F_{nf} parameter, which resulted in incoming longwave radiation values that were generally greater for north-facing edges than south-facing edges. In reality, observations of incoming longwave radiation show values to be higher on south-facing edges than north-facing edges (Musselman & Pomeroy, 2017; Webster et al., 2017). Higher incoming longwave radiation values on north-facing edges than south-facing edges in the model were possibly due to errors in modeling the magnitude of north-facing and south-facing net shortwave radiation. We note the τ_{dif} parameter was not very sensitive as the diffuse shortwave radiation was generally a small component of total incoming shortwave radiation. Therefore, future work should explore properly simulating the radiation differences by pairing observations of SWE with net shortwave observations and incoming longwave radiation between different sides of the forest.

In addition to determining the proper amounts of radiation from shortwave and longwave for different forest edges, future work should explore the proper extent of north and south-facing edges. For instance, forest-shading has a larger process scale, which varies from (0.5-2H) (Golding & Swanson, 1978; Lawler & Link, 2011; Musselman et al., 2015; Seyednasrollah & Kumar, 2014) than enhanced longwave radiation, which is around 0.5 H (Lawler & Link, 2011; Musselman & Pomeroy, 2017; Seyednasrollah & Kumar, 2014; Webster et al., 2016; Woo & Giesbrecht, 2000). Therefore the classification technique used in (Currier & Lundquist, 2018), which is equidistant for north and south-facing edges could be adapted so that south-facing edges account for a smaller contributing area and north-facing edges account for a larger contributing area.

Furthermore, there is still snow depth variability within each tile, which could be accounted for statistically, using sub-element probability distributions based on the coefficient of variation (Currier & Lundquist, 2018; Liston, 2004; Luce & Tarboton, 2004). Coefficients of variation could be computed from lidar-derived snow depth, other remote sensing platforms, or based on the distance to canopy edge (Mazzotti et al., 2019).

Additional Model Utility

Forest managers are actively changing the forest distribution to improve ecosystem health and maximize snow retention (Alexander & Watkins, 1977; Churchill et al., 2013; Dickerson-Lange et al., 2015; Ellis et al., 2013; Kittredge, 1953). Specific changes to the forest involve clear cutting (Alexander & Watkins, 1977), cylindrical gaps (Dickerson-Lange et al., 2015; Ellis et al., 2013; Golding & Swanson, 1978), and cutting strips in east west contours about the size of one three height (Anderson et al., 1976; Kittredge, 1953).

The tiling parameterization can be applied as a generic tool for forest managers to understand how changes in forest structure are expected to influence streamflow. For instance, forest managers can now use DHSVM to test impacts on streamflow from cylindrical gaps (Sun et al., 2018), or from strip cuts or any other technique that maximizes forest shading but does not shade the forest the same as forest gaps. Forest managers can determine the maximum forest shading they can have from strip cutting and then adjust the north-facing tile fraction to see the response in streamflow. Lastly, we note the tile model also offers a better comparison to point data. For instance, SNOTEL sites are often located in gaps within the forest, which might be shaded by the forest, or on the south-facing edges of the forest.

Computational Expense

Despite evolving three additional snowpack's, computational time increased only doubled in Tuolumne, and only increased 67% in the Jemez, and 95% in the Chiwawa. Increase in computation time was based on the length of the snow season within individual tiles and the fractional forest coverage in the basin. This makes a sub-element tiling parameterization an attractive approach to incorporate snow depth variability and capture differences in radiation between forests, forest edges, and exposed areas without increasing the spatial resolution of the model.

4.7 Conclusions

A tiling parameterization that explicitly simulated radiation differences within the forest was incorporated into DHSVM and based on classifications from high-resolution (1-3 m) vegetation maps. The tile parameterization simulated SWE between exposed and forested areas, as well as between north and south-facing edges, reasonably well compared to lidar-derived SWE observations. The impact that the tile model had on streamflow and grid-cell average SWE was

primarily a function of the basin-average tree height, the watershed's latitude, and the grid cell's average fractional forest area. In Jemez, NM, where forests were relatively sparse and trees were 10.2-m tall on average, the tile model's grid cell average snow disappearance date (SDD) was 12-days earlier and 10-day average peak streamflow occurred 20-days earlier than the original model. In contrast, in the Chiwawa, WA, where forests were dense and 17.2-m tall on average, the tile model's grid cell average SDD was 11 days later and streamflow increased up to 11-13% between mid-July and the end of August. Tree heights controlled the shortwave radiation attenuation in addition to an extinction coefficient parameter and the sun's elevation angle, which changed with latitude. Therefore, on April 1 in the Chiwawa 80% of the radiation was attenuated, compared to 48% and 42% in the Tuolumne and Jemez, respectively. In Tuolumne, CA, the tile model had less of an effect on streamflow and grid cell average SWE as the watershed was less forested and forests were denser compared to the Jemez.

Furthermore, despite statistically different snow depth distributions and radiation differences, forest edges had a relatively minimal effect on simulating streamflow (2-6%) in all basins due to low contributing areas. However, grid cell average ablation rates and streamflow were primarily impacted by tiled grid cells that explicitly represented radiation differences between exposed and forested areas. The response to tiled grid cells, which only contained forest and exposed areas, highlighted nonlinear responses in SWE and streamflow to forest-snow interactions as linearly scaling radiation based on the fractional forest cover did not result in a linear response in streamflow and SWE.

Table 4.1 Meteorological and watershed forest characteristics. *Mean tree height was calculated where lidar data was available within the watershed and the average height where vegetation greater than 2 m. $^{+}$Fraction of the watershed that is forested based on a coarsened (90-150 m) NLCD vegetation map. $^{\wedge}$Fraction of the watershed that is forested based on high-resolution (1-3 m) maps from NAIP imagery and

	Upper Tuolumne River Watershed, CA *Highway 120 Gauge*	**Jemez River Watershed, NM**	**Chiwawa River Watershed, WA**
General Watershed and Meteorological Statistics			
Watershed Size [km^2]	186	1222	446
Median and Range in Elevation [m]	3158 1314	2612 1719	1365 2034
Average Incoming Shortwave Radiation (Nov-April) [W m^{-2}]	175	223	153
Mean Winter Temperature (Nov-Mar) [°C]	WY 2014: -2.0 WY 2015: -5.2 WY 2016: -5.0	WY 2014: -2.6 WY 2015: -1.1 WY 2016: -3.0	WY 2011: -5.5 WY 2012: -6.0 WY 2013: -4.6
Basin Total Winter Precipitation (Nov-Mar) [mm]	WY 2014: 240 WY 2015: 723 WY 2016: 1127	WY 2014: 280 WY 2015: 206 WY 2016: 324	WY 2011: 1154 WY 2012: 1087 WY 2013: 759
Vegetation Characteristics I: Calculations based on high-resolution (1-3 m) vegetation maps derived from lidar or NAIP imagery.			
Mean Tree Height [m]*	8.3	10.2	17.2
Watershed Fraction$^{\wedge}$: Forested	39%	48%	80%
Watershed Fraction: North-Facing Edge	3%	6%	2%
Watershed Fraction: South-Facing Edge	3%	6%	2%
Watershed Fraction: Exposed	55%	40%	16%
Vegetation Characteristics II: Calculations based on coarsened (90-150 m) grid cells.			
Fraction of Watershed^{+}: Forested	45%	80%	84%
Average fraction of forest grid cell: Forested (Forest Density)	70%	57%	87%
Average fraction of forest grid cell: North Facing	5%	7%	2%
Average fraction of forest grid cell: South Facing	4%	6%	2%
Average fraction of forest grid cell: Exposed	21%	30%	11%

Table 4.2 Calibration performance metrics for simulated SWE at a point, where there were lidar data, and against streamflow for three different watersheds. *Metrics computed at snow pillows. +Metrics computed using available airborne lidar data. ^Metrics computed using stream gauge data.

	RMSE* [cm]	**Average Peak SWE Difference* [Modeled-Observed] [cm/%]**	**Difference in Snow Date Disappearance* [Modeled – Observed] [days]**	**Basin Average SWE Difference+ [Modeled-Observed] [cm/%]**	**Nash Sutcliffe Efficiency^**
Upper Tuolumne, CA: WY 2015-2017	**Dana:** 8.8 cm	**Dana:** -7.9 cm /-12.8 %	**Dana:** -8	**March 25 2016**: 2 cm / 26% **April 07 2016:** 5 cm / 9.5% **April 01 2017:** 7 cm / 6.8%	0.59
Jemez, NM WY 2008-2010	**Quemazon:** 3.3 cm **Vacas:** 9.8 cm **Senorita:** 9.7 cm	**Quemazon:** -3.8 cm/ -15% **Vacas**: -2.6 cm/ -10% **Senorita:** -1.6 cm/ -8%	**Quemazon:** 1 **Vacas:** -3 **Senorita:** -10	**Part of Basin - April 1 2010:** 1.9 cm / 10%	-1.63
Chiwawa, WA WY 2011-2013	**Trinity:** 12.2	**Trinity:** -0.1 cm / -1%	**Trinity:** 4	-	0.80

Table 4.3 Resulting model parameters based on calibration to streamflow and SWE observations from SNOTEL sites and lidar-derived basin average SWE.

	Tuolumne, CA	Jemez, NM	Chiwawa, WA
Parameters Adjusted During Calibration			
Snow Interception Efficiency *Snowfall fraction that can be intercepted in a precipitation event*	**0.6**	**0.4**	**0.6**
Maximum Resistance *Maximum cuticular resistance*	**4000**	**5000**	**4000**
Minimum Resistance *Minimal stomatal resistance*	**660**	**250**	**660**
Root Zone Depth *Depth at which roots can extract water for each soil layer (top to bottom)*	**0.75 1.0 0.2**	**1.5 1.0 0.5**	**0.1 0.15 0.2**
Overstory Root Fraction *Fractional area of roots from the overstory for each soil layer (top to bottom)*	**0.35 0.4 0.4**	**0.35 0.35 0.35**	**0.2 0.4 0.4**
Fresh Snow Albedo *Albedo after a snowfall*	**0.85**	**0.85**	**0.81**
Albedo Accumulation Lambda *Controls the decay of albedo when snow surface temperature is less than 0°C*	**0.92**	**0.89**	**0.85**
Albedo Melting Lambda *Controls the decay of albedo when snow surface temperature = 0°C*	**0.57**	**0.84**	**0.68**
Albedo Accumulation Min *Minimum snow albedo when snow surface temperature < 0°C*	**0.7**	**0.7**	**0.4**
Albedo Melting Min *Minimum snow albedo when snow surface temperature = 0°C*	**0.5**	**0.6**	**0.3**
Parameters adjusted to match observed SWE for each tile *Parameters are applied to both original and tile model*			
Fractional North Facing Coverage *Controls the amount longwave radiation received at the south facing edge*	**0.625**	**0.55**	**--**
Fractional South Facing Coverage *Controls the amount longwave radiation received at the south facing edge*	**0.25**	**0.4**	**--**
Diffuse Radiation Attenuation *Extinction of diffuse radiation in the forest*	**0.215**	**0.215**	**--**
Diffuse Radiation Attenuation NF *Extinction of diffuse radiation at the SF edge*	**0.75**	**0.75**	**--**
Diffuse Radiation Attenuation SF	**0.75**	**0.75**	**--**

Extinction of diffuse radiation at the SF edge			
Monthly Light Extinction *Input parameter into tau for shortwave radiation extinction in forest and NF edge*	**0.065**	**0.045**	**--**
Canopy View Adjustment Factor (SVF) *Controls the amount of longwave received in forest grid cell or forest tile*	**0.8**	**0.75**	**--**

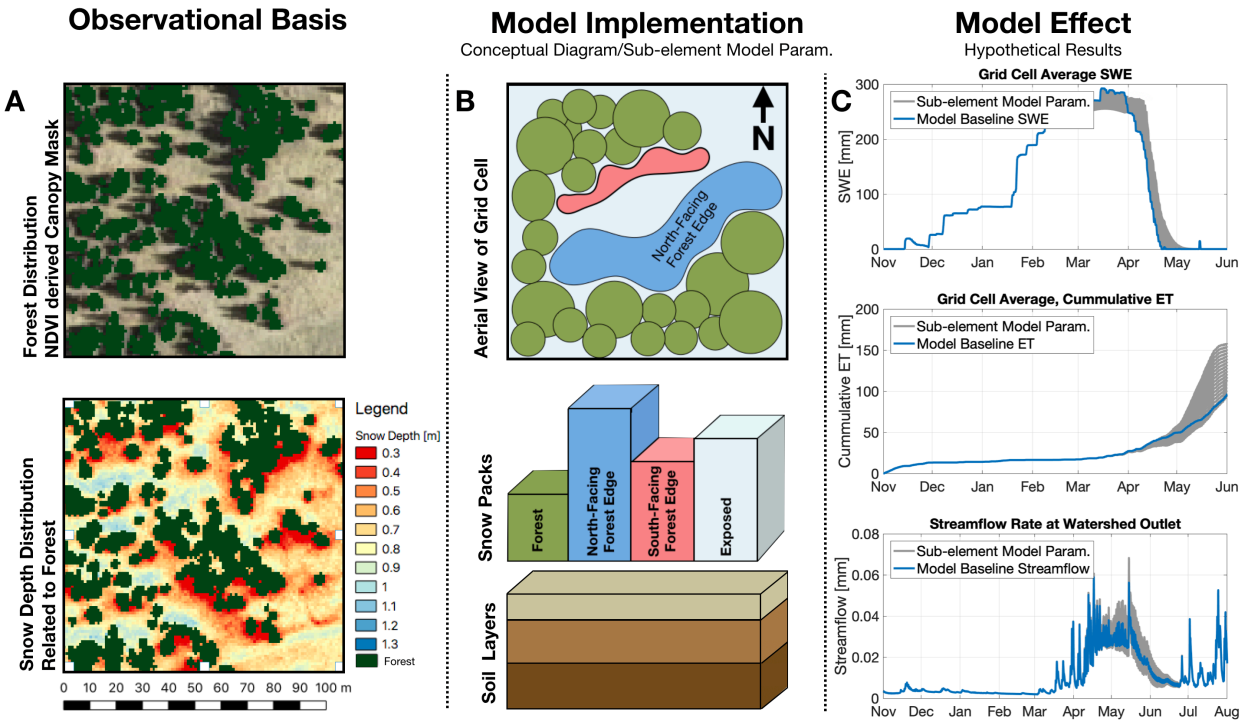

Figure 4.1 A) Deeper snow north of the NDVI-derived canopy mask, with shallower snow on the south-side of the trees in Jemez Caldera, NM, USA. B) Spatial heterogeneity of snow is accounted for with four simulated snowpacks per grid cell driven by unique radiation conditions. Each snowpack melts independently, providing water to a shared 3-layer soil reservoir. C) We seek to understand the effect that this model restructuring has on grid cell average SWE, cumulative ET, and streamflow.

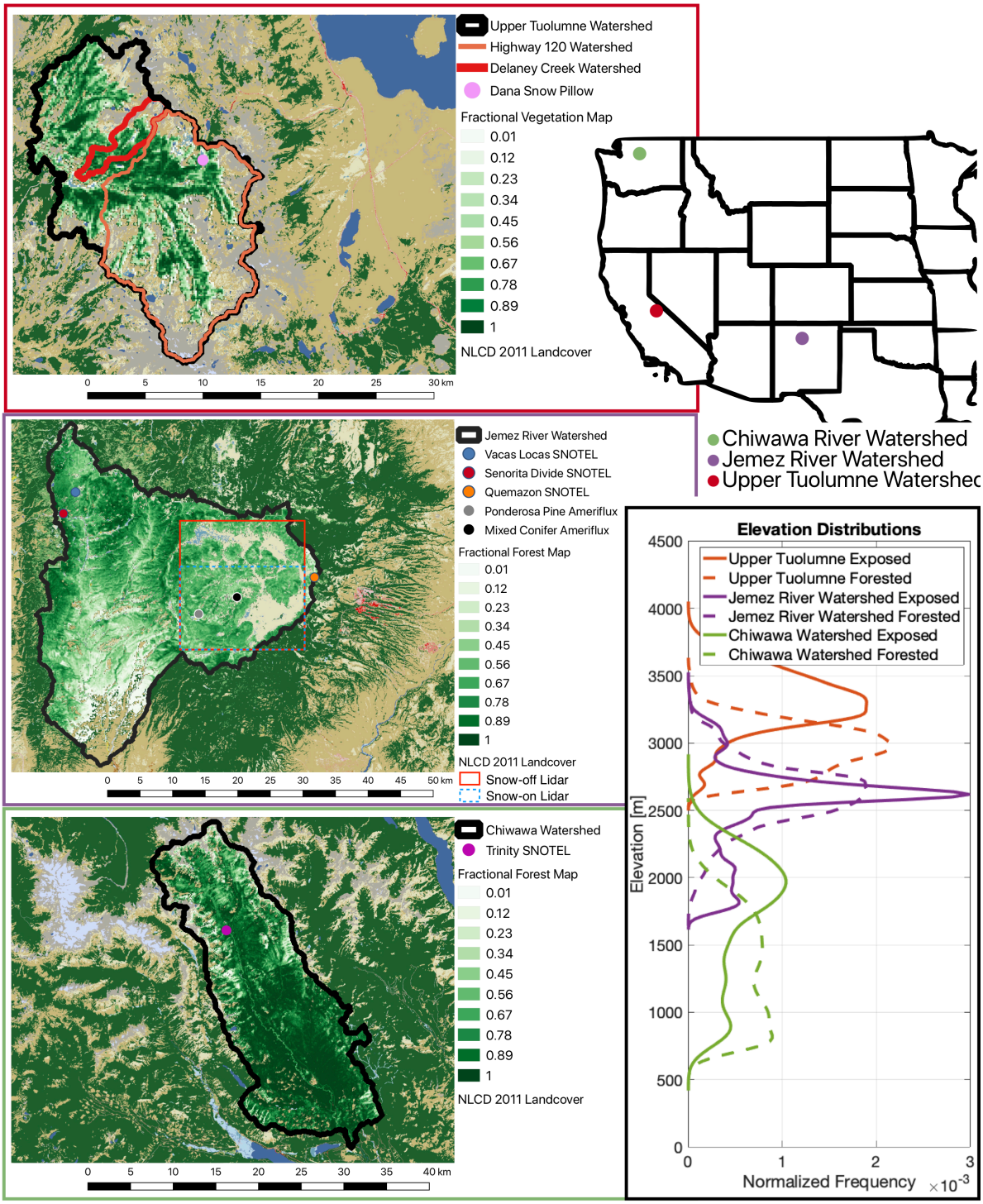

Figure 4.2 Basin delineations, fractional forest maps derived from lidar, NAIP, and NLCD 2011 data used within the original and tile version of DHSVM for three different watersheds. Watersheds organized based on elevation. SNOTEL sites contain observations of precipitation and SWE used for evaluating precipitation and evaluating SWE simualtions in exposed areas.

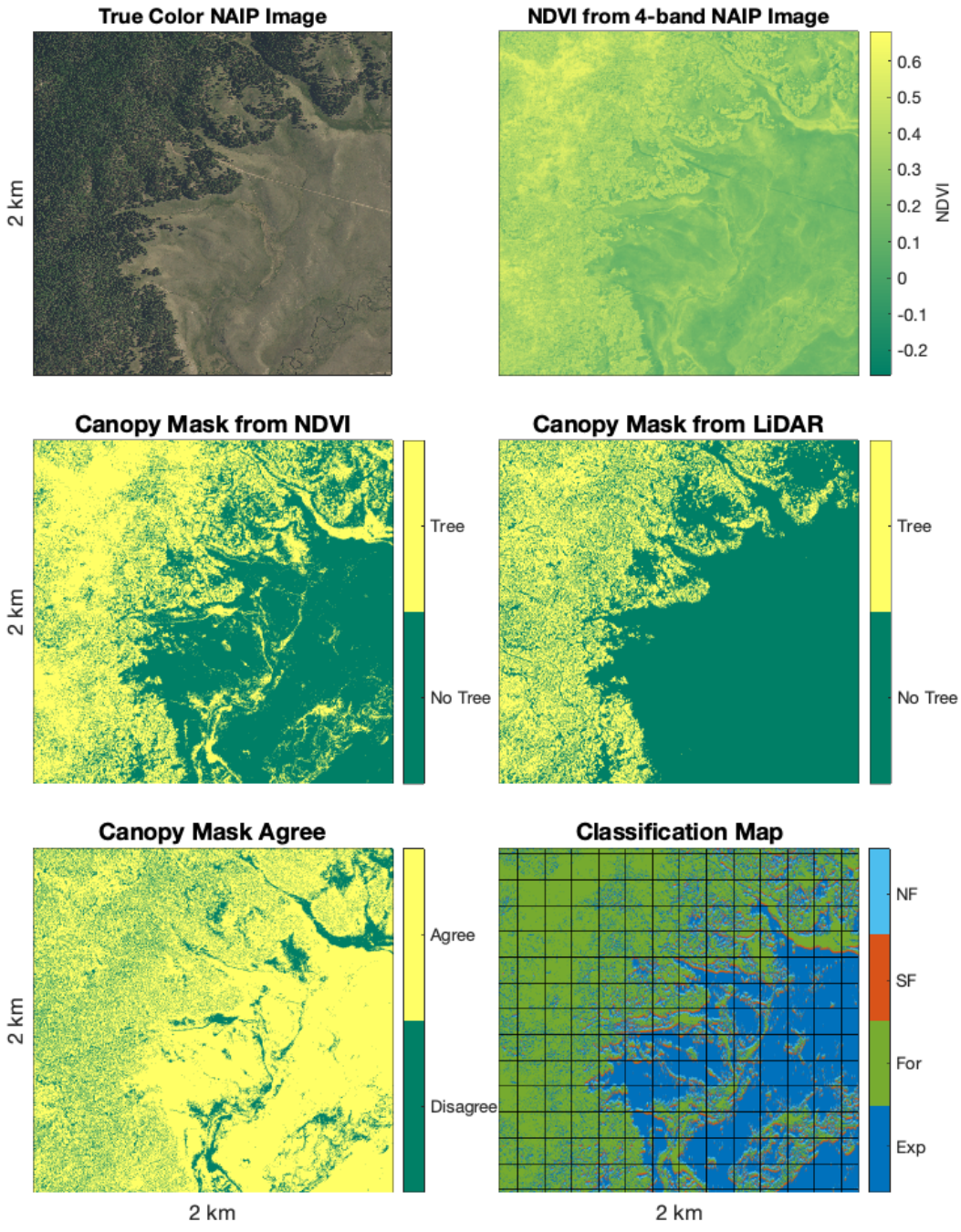

Figure 4.3 Example of using NAIP imagery to calculate NDVI and threshold NDVI to create a canopy mask. The resulting canopy mask used classification techniques described in (Currier & Lundquist, 2018) to classify north and south-facing edges, in addition to exposed and forest areas. The NAIP imagery agreed at 80 percent of the pixels within the 2-km domain. The classification map is further masked out using NLCD 2011 vegetation classifications (Section 4.3.4).

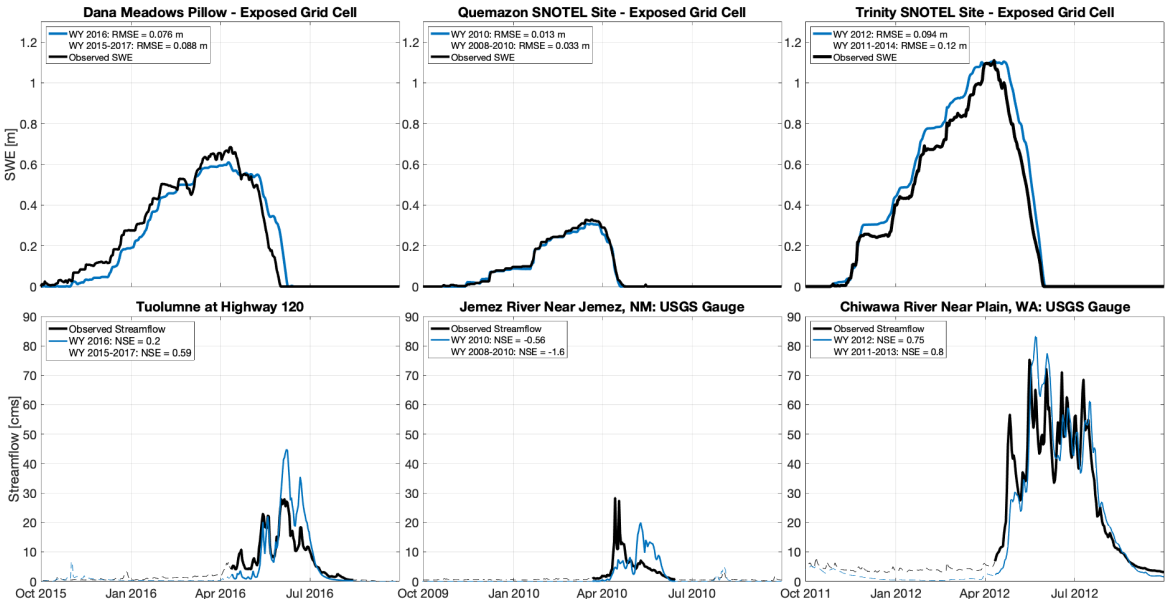

Figure 4.4 Model calibration results for a representative water year at snow pillow and stream gauges. Left column: Upper Tuolumne simulations during an average water year – WY 2016. Middle Column: Jemez River Watershed in WY 2010 when lidar observations of snow depth exist. Right Column: Chiwawa watershed calibrated simulations of SWE and streamflow.

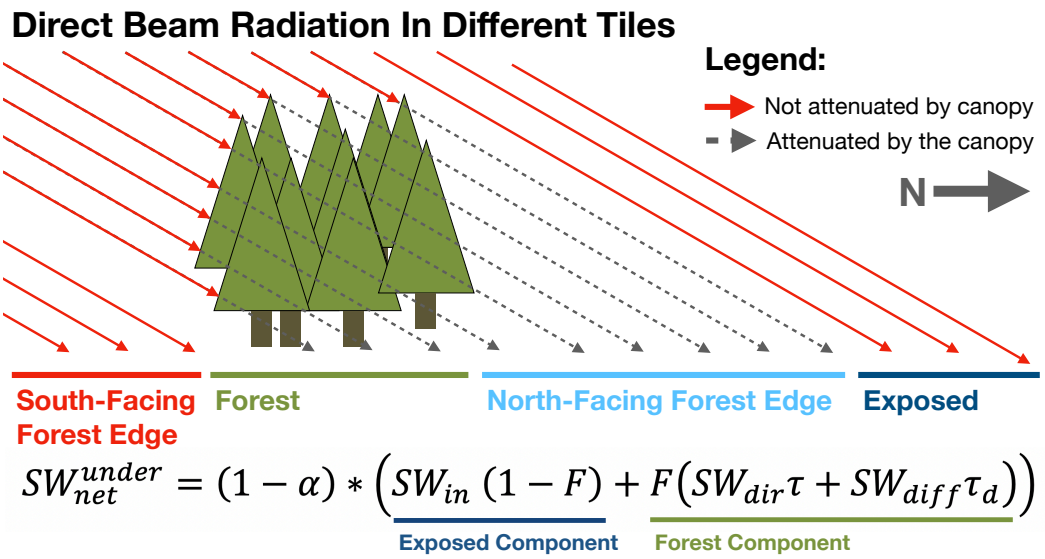

Figure 4.5 Example of direct beam radiation for different components of the tile model. Partitioning and derivations of equations 7-10 are based on the equation for net radiation in the original DHSVM (equation 1).

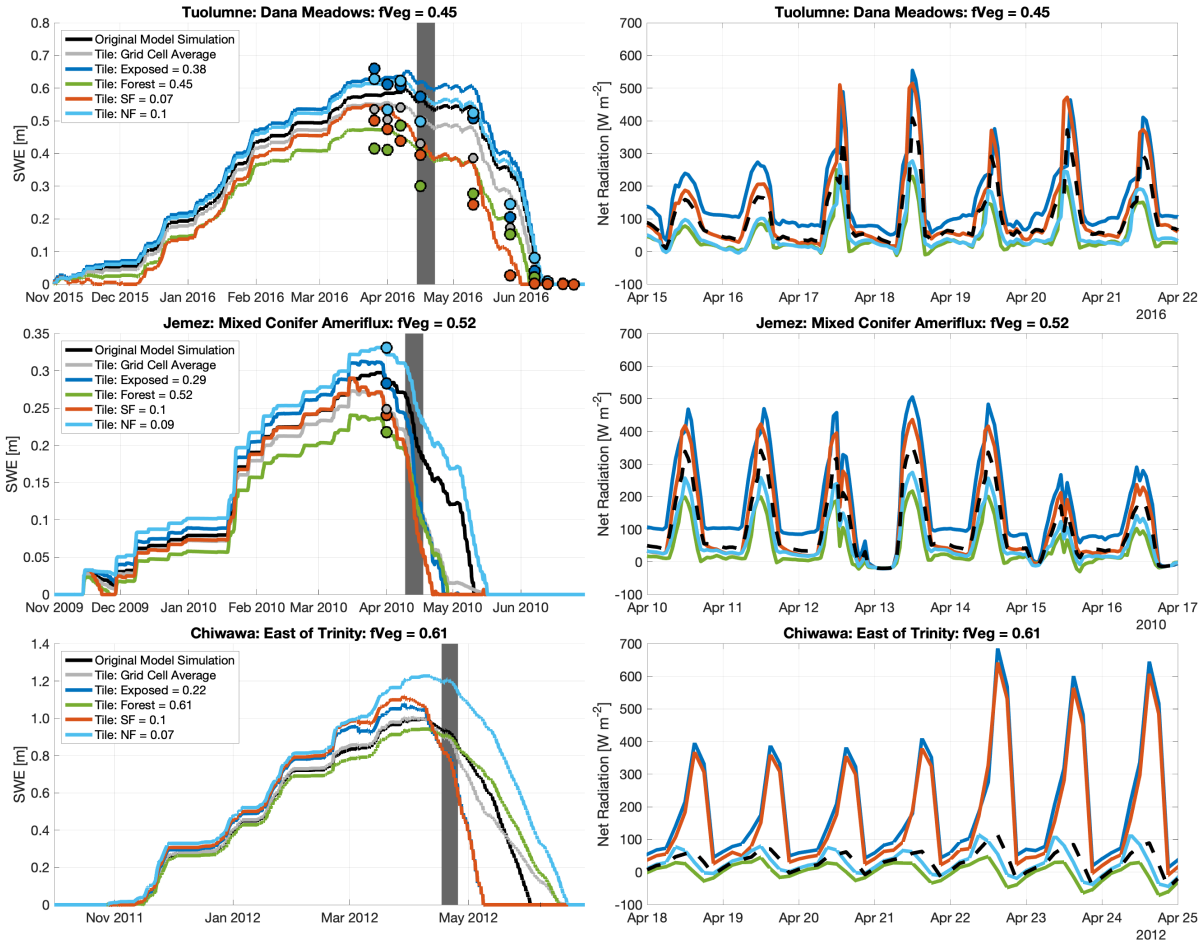

Figure 4.6 Left column: Example simulations of SWE for different tiles at an individual grid cell for each watershed in response to different radiation conditions. Circles show the mean lidar-derived SWE for each tile within the grid cell and the grid cell average SWE. Numbers in legend refer to the fractional area of each tile within the grid cell. Right column: Net radiation simulations for each tile in the original model during a week in the ablation season shading in left column.

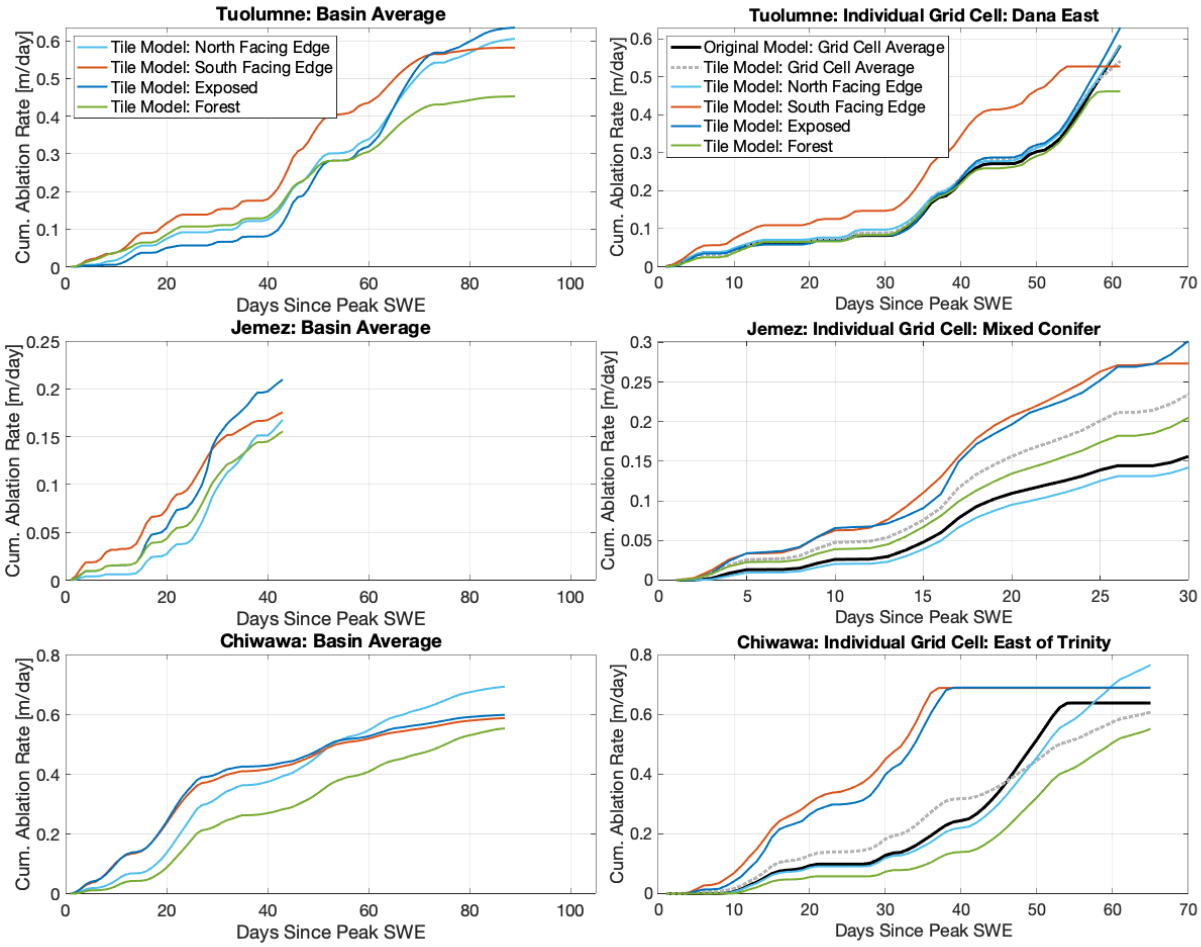

Figure 4.7 Basin average daily ablation rates for each tile compared to daily ablation rates for the example grid cells shown in Figure 4.5. Ablation rates were calculated based on the day of peak SWE in the original model.

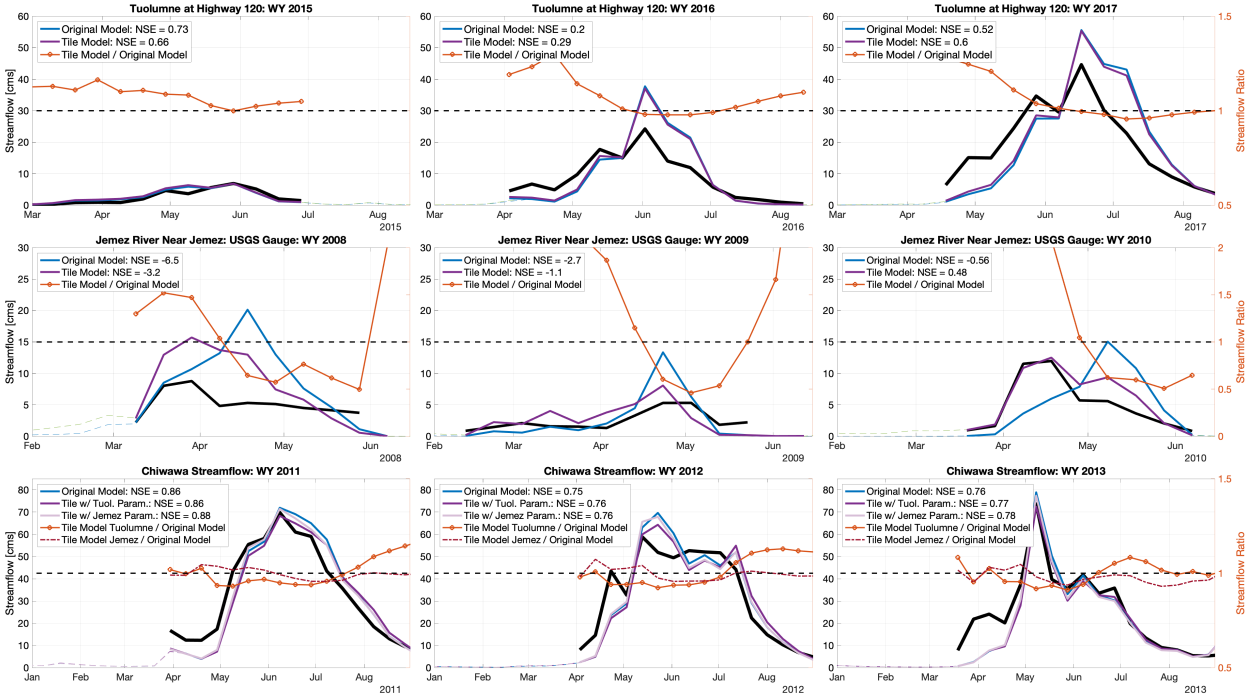

Figure 4.8 Simulated 10-day average streamflow and observed streamflow (black) over three water years (columns) for each watershed (rows). Streamflow ratios show the tile model divided by the original model's 10-day average streamflow. The Chiwawa, shows simulated streamflow when using forest-edge parameters consistent with those in the Tuolumne and Jemez as no lidar-derived SWE observation exist in the Chiwawa. Note changes in both y-axes between rows.

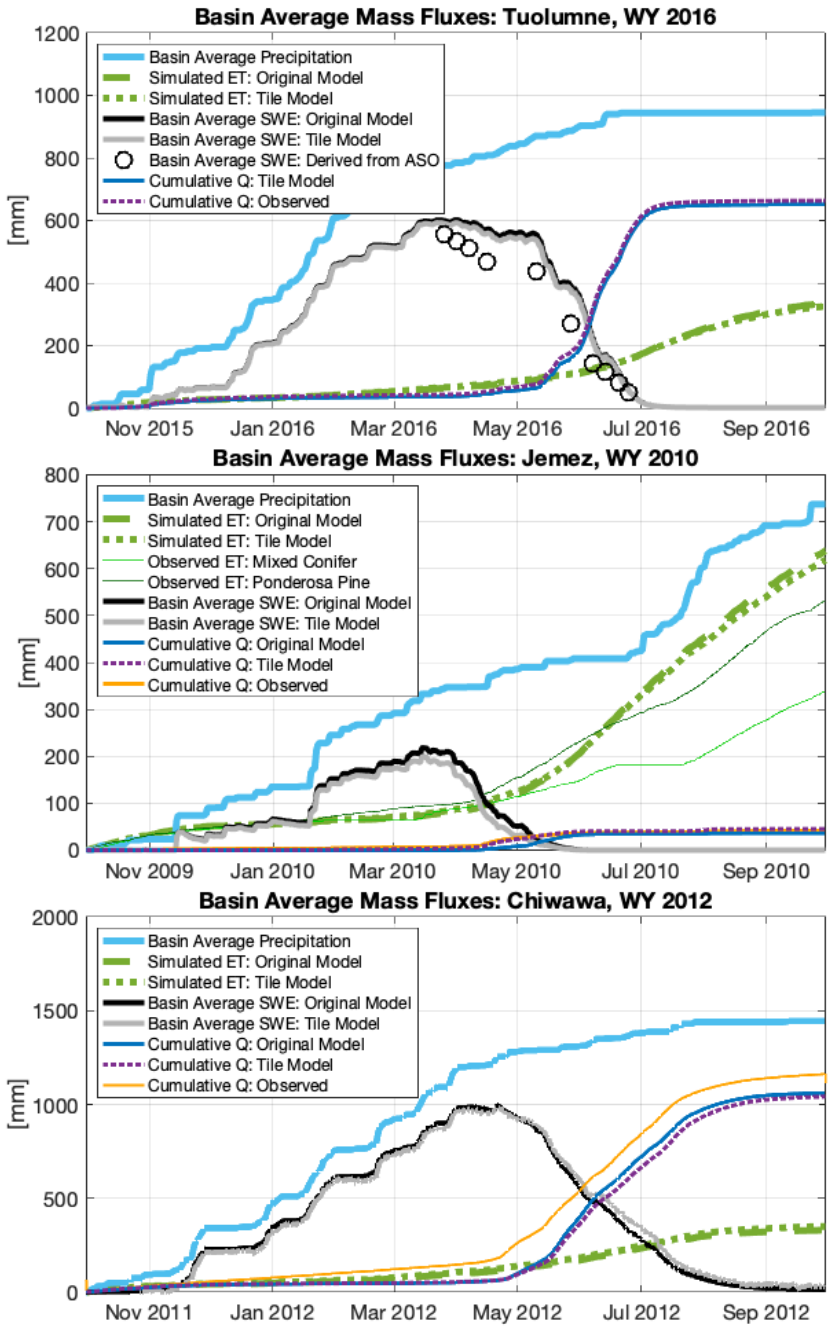

Figure 4.9 Cumulative fluxes of precipitation, evapotranspiration, and streamflow for each watershed normalized by the watershed area. Simulated basin average SWE is shown to represent the snow season and difference between the tile and original model. The Jemez show observations of evapotranspiration from two Ameriflux towers. These observations are missing 46-49% of their observations and are therefore low estimates of evapotranspiration. Tuolumne does not show observed streamflow as there were ice jams present within the data and it was unclear how to interpolate between observations. Tuolumne shows observed basin average SWE from the lidar derived SWE estimates.

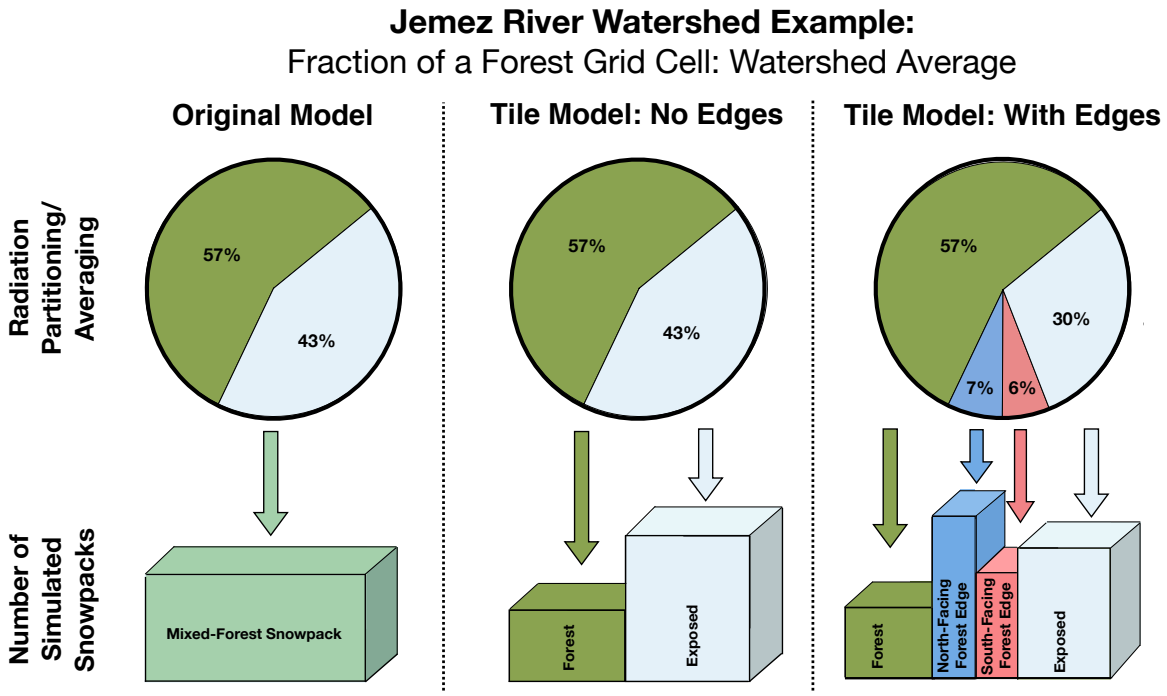

Figure 4.10 Example in the Jemez for three different model setups. In the original model, radiation between the forest and exposed areas is averaged based on the fractional forest coverage. In the tile model radiation for the forest, north-facing, south-facing, and exposed areas is directly incident on an independent snowpack. The tile model can be run with two snowpacks for exposed and forested areas, or also with forest edges.

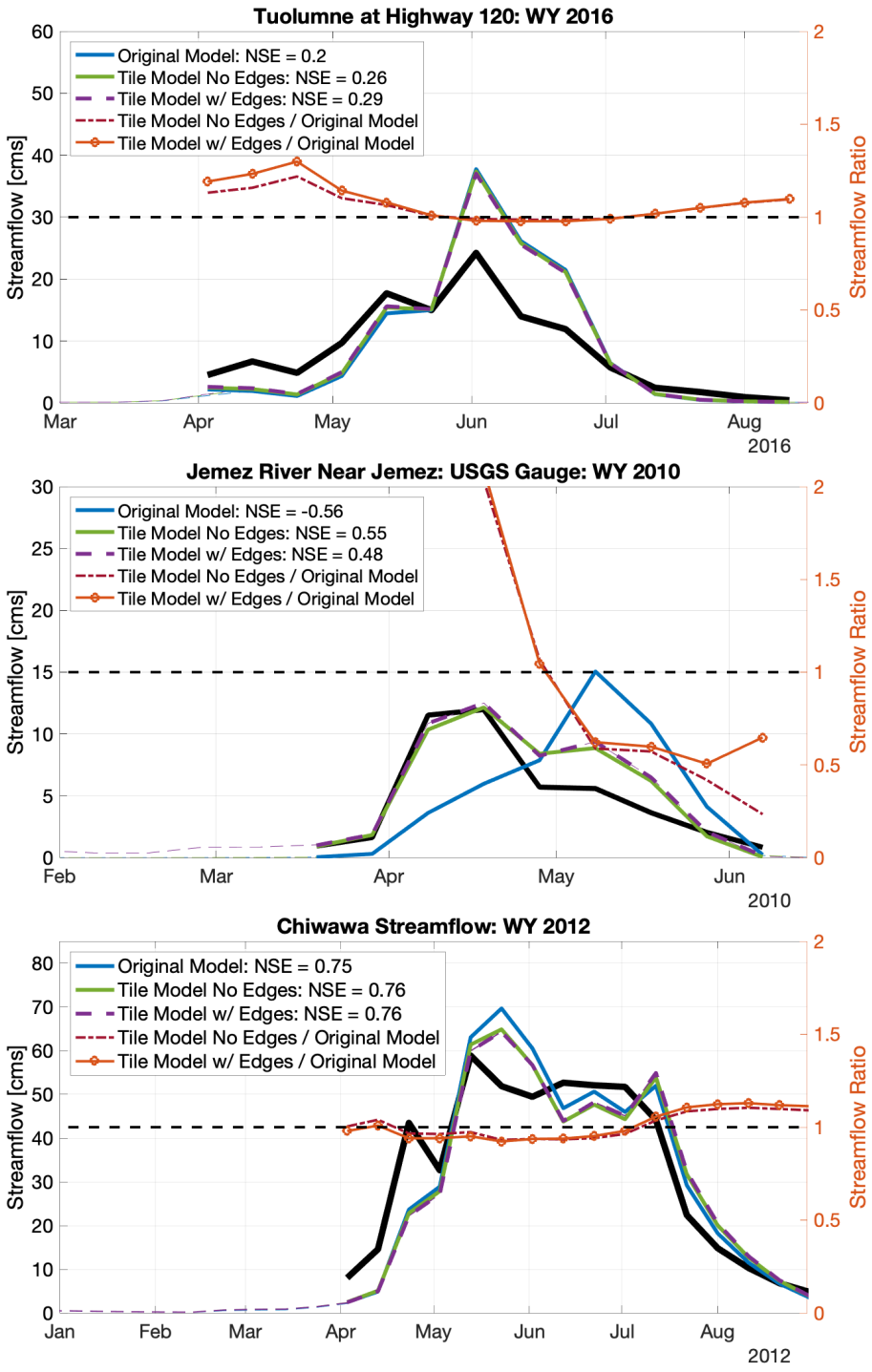

Figure 4.11 Streamflow for the three different watersheds within a representative water year. Observed streamflow (black) is compared to the baseline simulations of streamflow, the tile model without forest edges, and the tile model with forest edges. Streamflow ratio compare both tile model simulations with the baseline simulation. NSE's are for the water year shown in the figure using daily values.

References

Alexander, R. R., & Watkins, R. K. (1977). *The Fraser Experimental Forest, Colorado*. *General Technical Report - US Department of Agriculture, Forest Service*. Fort Collins, Colorado.

Anderson, H., Hoover, M., & Reinhart, K. (1976). *Forests and Water: Effects of forest management on floods, sedimentation, and water supply*. Berkeley, California.

Anderson, K. E., Glenn, N. F., Spaete, L. P., Shinneman, D. J., Pilliod, D. S., Arkle, R. S., et al. (2018). Estimating vegetation biomass and cover across large plots in shrub and grass dominated drylands using terrestrial lidar and machine learning. *Ecological Indicators*, *84*(October 2017), 793–802. https://doi.org/10.1016/j.ecolind.2017.09.034

Anderton, S. P., White, S. M., & Alvera, B. (2004). Evaluation of spatial variability in snow water equivalent for a high mountain catchment. *Hydrological Processes*, *18*(3), 435–453. https://doi.org/10.1002/hyp.1319

Andreadis, K. M., Storck, P., & Lettenmaier, D. P. (2009). Modeling snow accumulation and ablation processes in forested environments. *Water Resources Research*, *45*(5), 1–13. https://doi.org/10.1029/2008WR007042

Axelsson, P. (2000). DEM Generation from Laser Scanner Data Using adaptive TIN Models. *International Archives of Photogrammetry and Remote Sensing*, *23*(B4), 110–117. https://doi.org/10.1016/j.isprsjprs.2005.10.005

Bair, E. H., Davis, R. E., & Dozier, J. (2018). Hourly mass and snow energy balance measurements from Mammoth Mountain, CA USA, 2011-2017. *Earth System Science Data*, *10*(1), 549–563. https://doi.org/10.5194/essd-10-549-2018

Billings, W. D. (1969). Vegetational pattern near alpine timberline as affected by fire-snowdrift interactions. *Vegetatio Acta Geobotanica*, *19*(1–6), 192–207. https://doi.org/10.1007/BF00259010

Blöschl, G. (1999). Scaling issues in snow hydrology. *Hydrological Processes*, *13*(14–15), 2149–2175. https://doi.org/10.1002/(SICI)1099-1085(199910)13:14/15<2149::AID-HYP847>3.0.CO;2-8

Bohn, T. J., Livneh, B., Oyler, J. W., Running, S. W., Nijssen, B., & Lettenmaier, D. P. (2013). Global evaluation of MTCLIM and related algorithms for forcing of ecological and hydrological models. *Agricultural and Forest Meteorology*, *176*, 38–49. https://doi.org/10.1016/j.agrformet.2013.03.003

Brandle, J.R., Finch, S. (1991). How windbreaks work. *Natural Resourses, Nebraska Cooperative Extension Service*. National Agroforesty Center. https://doi.org/EC 91-1763-B

Brandle, J. R., & Nickerson, D. H. (n.d.). Windbreaks for Snow Management. National Agroforesty Center. Retrieved from https://nac.unl.edu/practices/windbreaks.htm

Broxton, P. D., Harpold, A. A., Biederman, J. A., Troch, P. A., Molotch, N. P., & Brooks, P. D. (2015). Quantifying the effects of vegetation structure on snow accumulation and ablation in mixed-conifer forests. *Ecohydrology*, *8*(6), 1073–1094. https://doi.org/10.1002/eco.1565

Carlson, B. Z., Choler, P., Renaud, J., Dedieu, J. P., & Thuiller, W. (2015). Modelling snow cover duration improves predictions of functional and taxonomic diversity for alpine plant communities. *Annals of Botany*, *116*(6), 1023–1034. https://doi.org/10.1093/aob/mcv041

Chang, H., Johnson, G., Hinkley, T., & Jung, I. W. (2014). Spatial analysis of annual runoff ratios and their variability across the contiguous U.S. *Journal of Hydrology*, *511*, 387–402. https://doi.org/10.1016/j.jhydrol.2014.01.066

Church, J. E. (1933). Snow Surveying: Its Principles and Possibilities. *Geographical Review*, *23*(4), 529. https://doi.org/10.2307/209242

Churchill, D. J., Larson, A. J., Dahlgreen, M. C., Franklin, J. F., Hessburg, P. F., & Lutz, J. A. (2013). Restoring forest resilience: From reference spatial patterns to silvicultural prescriptions and monitoring. *Forest Ecology and Management*, *291*, 442–457. https://doi.org/10.1016/j.foreco.2012.11.007

Clark, M. P., Hendrikx, J., Slater, A. G., Kavetski, D., Anderson, B., Cullen, N. J., et al. (2011). Representing spatial variability of snow water equivalent in hydrologic and land-surface models: A review. *Water Resources Research*, *47*(7). https://doi.org/10.1029/2011WR010745

Currier, W. R., & Lundquist, J. D. (2018). Snow Depth Variability at the Forest Edge in Multiple Climates in the Western United States. *Water Resources Research*, *54*, 1–18. https://doi.org/10.1029/2018WR022553

Currier, W. R., Thorson, T., & Lundquist, J. D. (2017). Independent Evaluation of Frozen Precipitation from WRF and PRISM in the Olympic Mountains. *Journal of Hydrometeorology*, *18*(10), 2681–2703. https://doi.org/10.1175/JHM-D-17-0026.1

Currier, W. R., Pflug, J., Mazzotti, G., Jonas, T., Deems, J. S., Bormann, K. J., et al. (2019). Comparing aerial lidar observations with terrestrial lidar and snow-probe transects from NASA's 2017 SnowEx campaign. *Water Resources Research*, 1–10. https://doi.org/10.1029/2018wr024533

Daly, C., Halbleib, M., Smith, J. I., Gibson, W. P., Doggett, M. K., Taylor, G. H., et al. (2008). Physiographically sensitive mapping of climatological temperature and precipitation across the conterminous United States. *International Journal of Climatology*, *28*(15), 2031–2064. https://doi.org/10.1002/joc.1688

DeBeer, C. M., & Pomeroy, J. W. (2010). Simulation of the snowmelt runoff contributing area in a small alpine basin. *Hydrology and Earth System Sciences*, *14*(7), 1205–1219. https://doi.org/10.5194/hess-14-1205-2010

Dedieu, J. P., Carlson, B. Z., Bigot, S., Sirguey, P., Vionnet, V., & Choler, P. (2016). On the importance of high-resolution time series of optical imagery for quantifying the effects of snow cover duration on alpine plant habitat. *Remote Sensing*, *8*(6). https://doi.org/10.3390/rs8060481

Deems, J. S., Fassnacht, S. R., & Elder, K. J. (2006). Fractal Distribution of Snow Depth from Lidar Data. *Journal of Hydrometeorology*, *7*(2), 285–297. https://doi.org/10.1175/JHM487.1

Deems, J. S., Fassnacht, S. R., & Elder, K. J. (2008). Interannual Consistency in Fractal Snow Depth Patterns at Two Colorado Mountain Sites. *Journal of Hydrometeorology*, *9*(5), 977–988. https://doi.org/10.1175/2008JHM901.1

Deems, J. S., Painter, T. H., & Finnegan, D. C. (2013). Lidar measurement of snow depth: A review. *Journal of Glaciology*, *59*(215), 467–479. https://doi.org/10.3189/2013JoG12J154

Deems, J. S., Gadomski, P. J., Vellone, D., Evanczyk, R., LeWinter, A. L., Birkeland, K. W., & Finnegan, D. C. (2015). Mapping starting zone snow depth with a ground-based lidar to assist avalanche control and forecasting. *Cold Regions Science and Technology*, *120*, 197–204. https://doi.org/10.1016/j.coldregions.2015.09.002

Dickerson-Lange, S. E., Lutz, J. A., Martin, K. A., Raleigh, M. S., Gersonde, R., & Lundquist, J. D. (2015). Evaluating observational methods to quantify snow duration under diverse forest canopies. *Water Resources Research*, *51*(2), 1203–1224. https://doi.org/10.1002/2014WR015744

Dickerson-Lange, S. E., Gersonde, R. F., Hubbart, J. A., Link, T. E., Nolin, A. W., Perry, G. H.,

et al. (2017). Snow disappearance timing is dominated by forest effects on snow accumulation in warm winter climates of the Pacific Northwest, United States. *Hydrological Processes*, *31*(10), 1846–1862. https://doi.org/10.1002/hyp.11144

Egli, L., & Jonas, T. (2009). Hysteretic dynamics of seasonal snow depth distribution in the Swiss Alps. *Geophysical Research Letters*, *36*(2), 1–5. https://doi.org/10.1029/2008GL035545

Elder, K., Dozier, J., & Michaelsen, J. (1991). Elder-Dozier-Michaelsen 1991 Snow Accumulation and distribution in an alpine watershed.pdf. *Water Resources Research*, *27*(7), 1541–1552.

Ellis, C. R., Pomeroy, J. W., & Link, T. E. (2013). Modeling increases in snowmelt yield and desynchronization resulting from forest gap-thinning treatments in a northern mountain headwater basin. *Water Resources Research*, *49*(2), 936–949. https://doi.org/10.1002/wrcr.20089

Essery, R., & Pomeroy, J. (2004a). Implications of spatial distributions of snow mass and melt rate for snow-cover depletion: theoretical considerations. *Annals of Glaciology*, *38*, 261–265.

Essery, R., & Pomeroy, J. (2004b). Vegetation and Topographic Control of Wind-Blown Snow Distributions in Distributed and Aggregated Simulations for an Arctic Tundra Basin. *Journal of Hydrometeorology*, *5*(5), 735–744. https://doi.org/10.1175/1525-7541(2004)005<0735:VATCOW>2.0.CO;2

Fassnacht, S. R., & Deems, J. S. (2005). Scaling associated with averaging and resampling of LiDAR-derived Montana snow depth data. *Proceedings of the 62nd Eastern Snow Conference*, 163–172.

Fischer, E. E., & Borland, J. P. (1983). *Estimation of Natural Streamflow in the Jemez River At the Boundaries of Indian Lands , Central New Mexico*. Albuquerque, New Mexico.

Ford, K. R., Ettinger, A. K., Lundquist, J. D., Raleigh, M. S., & Hille Ris Lambers, J. (2013). Spatial Heterogeneity in Ecologically Important Climate Variables at Coarse and Fine Scales in a High-Snow Mountain Landscape. *PLoS ONE*, *8*(6). https://doi.org/10.1371/journal.pone.0065008

Geddes, C. A., Brown, D. G., & Fagre, D. B. (2005). Topography and Vegetation as Predictors of Snow Water Equivalent across the Alpine Treeline Ecotone at Lee Ridge, Glacier National Park, Montana, U.S.A. *Arctic, Antarctic, and Alpine Research*, *37*(2), 197–205. https://doi.org/10.1657/1523-0430(2005)037[0197:TAVAPO]2.0.CO;2

Glennie, C. (2007). Rigorous 3D error analysis of kinematic scanning LIDAR systems. *Journal of Applied Geodesy*, *1*(3), 147–157. https://doi.org/10.1515/jag.2007.017

Golding, D. L., & Swanson, R. H. (1978). Snow accumulation and melt in small forest openings in Alberta. *Canadian Journal of Forest Research*, *8*(4), 380–388. https://doi.org/10.1139/x78-057

Goodison, B., Louie, P., & Yang, D. (1998). WMO solid precipitation measurement intercomparison: Final report. *Instrum. Obs. Methods Rep. 67*, *WMO/TD-No.*(67), 211. Retrieved from http://scholar.google.com/scholar?hl=en&btnG=Search&q=intitle:WMO+solid+precipitation+measurement+intercomparison:+Final+report#6

Greene, E. M., Liston, G. E., & Pielke, R. A. (1999). Simulation of above treeline snowdrift formation using a numerical snow-transport model. *Cold Regions Science and Technology*, *30*(1–3), 135–144. https://doi.org/10.1016/S0165-232X(99)00008-7

Griffith, D. A. (2009). Spatial Autocorrelation. In *International Encyclopedia of Human Geography* (Vol. 10, pp. 308–316). Elsevier Science.

Grünewald, T., Schirmer, M., Mott, R., & Lehning, M. (2010). Spatial and temporal variability of snow depth and ablation rates in a small mountain catchment. *Cryosphere*, *4*(2), 215–225. https://doi.org/10.5194/tc-4-215-2010

Harpold, A A, Guo, Q., Molotch, N., Brooks, P. D., Bales, R., Fernandez-Diaz, J. C., et al. (2014). LiDAR-derived snowpack data sets from mixed conifer forests accross the Western United States. *Water Resources Research*, *50*(October 2013), 2749–2755. https://doi.org/10.1002/2013WR013935.Received

Harpold, Adrian A., Molotch, N. P., Musselman, K. N., Bales, R. C., Kirchner, P. B., Litvak, M., & Brooks, P. D. (2015). Soil moisture response to snowmelt timing in mixed-conifer subalpine forests. *Hydrological Processes*, *29*(12), 2782–2798. https://doi.org/10.1002/hyp.10400

Hartzell, P. J., Gadomski, P. J., Glennie, C. L., Finnegan, D. C., & Deems, J. S. (2015). Rigorous error propagation for terrestrial laser scanning with application to snow volume uncertainty. *Journal of Glaciology*, *61*(230), 1147–1158. https://doi.org/10.3189/2015JoG15J031

Hättenschwiler, S., & Smith, W. K. (1999). Seedling occurrence in alpine treeline conifers: A case study from the central Rocky Mountains, USA. *Acta Oecologica*, *20*(3), 219–224. https://doi.org/10.1016/S1146-609X(99)80034-4

Hedrick, A. R., Marks, D., Havens, S., Robertson, M., Johnson, M., Sandusky, M., et al. (2018). Direct Insertion of NASA Airborne Snow Observatory-Derived Snow Depth Time Series Into the iSnobal Energy Balance Snow Model. *Water Resources Research*, *54*, 8045–8063. https://doi.org/10.1029/2018WR023400

Helsel, D. R., & Hirsch, R. M. (2002). Statistical Methods in Water Resources. In *4* (Vol. 4, pp. 1–524). U.S. Geological Survey. Retrieved from https://pubs.usgs.gov/twri/twri4a3/

Hiemstra, C. A., Liston, G. E., & Reiners, W. A. (2002). Snow Redistribution by Wind and Interactions with Vegetation at Upper Treeline in the Medicine Bow Mountains, Wyoming, U.S.A. *Arctic, Antarctic, and Alpine Research*, *34*(3), 262–273.

Hiemstra, C. A., Liston, G. E., & Reiners, W. A. (2006). Observing, modelling, and validating snow redistribution by wind in a Wyoming upper treeline landscape. *Ecological Modelling*, *197*(1–2), 35–51. https://doi.org/10.1016/j.ecolmodel.2006.03.005

Hodgson, M. E., Jensen, J., Raber, G., Tullis, J., Davis, B. A., Thompson, G., & Schuckman, K. (2005). An Evaluation of Lidar-derived Elevation and Terrain Slope in Leaf-off Conditions. *Photogrammetric Engineering & Remote Sensing*, *71*(7), 817–823. https://doi.org/10.14358/PERS.71.7.817

Homer, C. G., Dewitz, J. A., Yang, L., Jin, S., Danielson, P., Xian, G., et al. (2015). Completion of the 2011 National Land Cover Database for the conterminous United States-Representing a decade of land cover change information. *Photogrammetric Engineering and Remote Sensing*, *81*(5), 345–354.

Hopkinson, C., Sitar, M., Chasmer, L., Gynan, C., Agro, D., Enter, R., et al. (2001). Mapping the spatial distribution of snowpack depth beneath a variable forest canopy using airborne laser altimetry. *Proceedings of the 58th Annual Eastern Snow Conference*, 253–264. Retrieved from http://www.easternsnow.org/proceedings/2001/Hopkinson_2.pdf

Hopkinson, C., Sitar, M., Chasmer, L., & Treitz, P. (2004). Mapping Snowpack Depth beneath Forest Canopies Using Airborne Lidar. *Photogrammetric Engineering & Remote Sensing*, *70*(3), 323–330.

Hopkinson, C., Chasmer, L. E., Sass, G., Creed, I. F., Sitar, M., Kalbfleisch, W., & Treitz, P. (2005). Vegetation class dependent errors in lidar ground elevation and canopy height estimates in a boreal wetland environment. *Canadian Journal of Remote Sensing*, *31*(2), 191–206. https://doi.org/10.5589/m05-007

Hopkinson, C., Pomeroy, J., Debeer, C., Ellis, C., & Anderson, A. (2012). Relationships between snowpack depth and primary LiDAR point cloud derivatives in a mountainous environment. *IAHS-AISH Publication*, (September 2010), 354–358. Retrieved from http://cat.inist.fr/?aModele=afficheN&cpsidt=27917455

Huemmrich, K. F., & Goward, S. N. (1997). Vegetation canopy PAR absorptance and NDVI: An assessment for ten tree species with the SAIL model. *Remote Sensing of Environment*, *61*(2), 254–269. https://doi.org/10.1016/S0034-4257(97)00042-4

Hughes, M., Lundquist, J. D., & Henn, B. (2017). Dynamical downscaling overcomes deficiencies in gridded precipitation products in the Sierra Nevada, California. *Climate Dynamics*, *0*(0), 0. https://doi.org/http://dx.doi.org/10.1007/s00382-017-3631-z

Kim, E. (2018). How Can We Find Out How Much Snow Is in the World? *Eos*, *99*(June), 2–7. https://doi.org/10.1029/2018EO099939

Kim, E., Gatebe, C., Hall, D., Newlin, J., Misakonis, A., Elder, K., et al. (2017). NASA's snowex campaign: Observing seasonal snow in a forested environment. In *2017 IEEE International Geoscience and Remote Sensing Symposium (IGARSS)* (pp. 1388–1390). IEEE. https://doi.org/10.1109/IGARSS.2017.8127222

Kirchner, P. B., Bales, R. C., Molotch, N. P., Flanagan, J., & Guo, Q. (2014). LiDAR measurement of seasonal snow accumulation along an elevation gradient in the southern Sierra Nevada, California. *Hydrology and Earth System Sciences*, *18*(10), 4261–4275. https://doi.org/10.5194/hess-18-4261-2014

Kittredge, J. (1953). Influences of Forests on Snow in the Ponderosa-Sugar Pine-Fir Zone of the Central Sierra Nevada. *Journal of Chemical Information and Modeling*, *22*(1), 1–94.

LaChapelle, E. (1958). Winter snow observation at Mt. Olympus. In *Proceedings 26th Annual Western Snow Conference* (pp. 59–63). Bozeman, MT: Western Snow Conference. Retrieved from https://westernsnowconference.org/node/1174

Lawler, R. R., & Link, T. E. (2011). Quantification of incoming all-wave radiation in discontinuous forest canopies with application to snowmelt prediction. *Hydrological Processes*, *25*(21), 3322–3331. https://doi.org/10.1002/hyp.8150

Leach, J. A., & Moore, R. D. (2014). Winter stream temperature in the rain-on-snow zone of the Pacific Northwest: Influences of hillslope runoff and transient snow cover. *Hydrology and Earth System Sciences*, *18*(2), 819–838. https://doi.org/10.5194/hess-18-819-2014

Lehning, M., Löwe, H., Ryser, M., & Raderschall, N. (2008). Inhomogeneous precipitation distribution and snow transport in steep terrain. *Water Resources Research*, *44*(7), 1–19. https://doi.org/10.1029/2007WR006545

Lehning, Michael, Völksch, I., Gustafsson, D., Nguyen, T. A., Stähli, M., & Zappa, M. (2006). ALPINE3D: a detailed model of mountain surface processes and its application to snow hydrology. *Hydrological Processes*, *20*(10), 2111–2128. https://doi.org/10.1002/hyp.6204

Li, D., Wrzesien, M. L., Durand, M., Adam, J., & Lettenmaier, D. P. (2017). How much runoff originates as snow in the western United States, and how will that change in the future? *Geophysical Research Letters*, *44*(12), 6163–6172. https://doi.org/10.1002/2017GL073551

Li, L., & Pomeroy, J. W. (1997). Estimates of Threshold Wind Speeds for Snow Transport Using Meteorological Data. *Journal of Applied Meteorology*, *36*(3), 205–213.

https://doi.org/10.1175/1520-0450(1997)036<0205:EOTWSF>2.0.CO;2
Liang, X., Lettenmaier, D. P., Wood, E. F., & Burges, S. J. (1994). A simple hydrologically based model of land surface water and energy fluxes for general circulation models. *Journal of Geophysical Research: Atmospheres*, *99*(D7), 14415–14428. https://doi.org/10.1029/94JD00483
Link, T., & Marks, D. (1999). Distributed simulation of snowcover mass- and energy-balance in the boreal forest, *2452*(January).
Link, T. E., Marks, D., & Hardy, J. P. (2004). A deterministic method to characterize canopy radiative transfer properties. *Hydrological Processes*, *18*(18), 3583–3594. https://doi.org/10.1002/hyp.5793
Liston, G. E. (1999). Interrelationships among Snow Distribution, Snowmelt, and Snow Cover Depletion: Implications for Atmospheric, Hydrologic, and Ecologic Modeling. *Journal of Applied Meteorology*, *38*(10), 1474–1487. https://doi.org/10.1175/1520-0450(1999)038<1474:IASDSA>2.0.CO;2
Liston, G. E. (2004). Representing subgrid snow cover heterogeneities in regional and global models. *Journal of Climate*, *17*(6), 1381–1397. https://doi.org/10.1175/1520-0442(2004)017<1381:RSSCHI>2.0.CO;2
Liston, G. E., & Elder, K. (2006). A Meteorological Distribution System for High-Resolution Terrestrial Modeling (MicroMet). *Journal of Hydrometeorology*, *7*(2), 217–234. https://doi.org/10.1175/JHM486.1
Liston, G. E., & Sturm, M. (1998). A snow-transport model for complex terrain. *Journal of Glaciology*, *44*(148), 498–516. https://doi.org/10.3189/S0022143000002021
Liu, C., Ikeda, K., Rasmussen, R., Barlage, M., Newman, A. J., Prein, A. F., et al. (2017). Continental-scale convection-permitting modeling of the current and future climate of North America. *Climate Dynamics*, *49*(1–2), 71–95. https://doi.org/10.1007/s00382-016-3327-9
Livneh, B., Rosenberg, E. A., Lin, C., Nijssen, B., Mishra, V., Andreadis, K. M., et al. (2013). A long-term hydrologically based dataset of land surface fluxes and states for the conterminous United States: Update and extensions. *Journal of Climate*, *26*(23), 9384–9392. https://doi.org/10.1175/JCLI-D-12-00508.1
Luce, C. H., & Tarboton, D. G. (2004). The application of depletion curves for parameterization of subgrid variability of snow. *Hydrological Processes*, *18*(8), 1409–1422. https://doi.org/10.1002/hyp.1420
Luce, C. H., Tarboton, D. G., & Cooley, K. R. (1998). The infuence of the spatial distribution of snow on basin-averaged snowmelt\r. *Hydrological Processes*, *12*(May 1997), 1671–1683. https://doi.org/10.1002/(SICI)1099-1085(199808/09)12:10/11<1671::AID-HYP688>3.0.CO;2-N
Luce, C. H., Tarboton, D. G., & Cooley, K. R. (1999). Sub-grid parameterization of snow distribution for an energy and mass balance snow cover model. *Hydrological Processes*, *13*(12–13), 1921–1933. https://doi.org/10.1002/(SICI)1099-1085(199909)13:12/13<1921::AID-HYP867>3.0.CO;2-S
Lundquist, J. D., & Dettinger, M. D. (2005). How snowpack heterogeneity affects diurnal streamflow timing. *Water Resources Research*, *41*(5), 1–14. https://doi.org/10.1029/2004WR003649
Lundquist, J. D., & Huggett, B. (2010). Evergreen trees as inexpensive radiation shields for temperature sensors. *Water Resources Research*, *46*(4), 1–5. https://doi.org/10.1029/2008WR006979

Lundquist, J. D., Dettinger, M. D., & Cayan, D. R. (2005). Snow-fed streamflow timing at different basin scales: Case study of the Tuolumne River above Hetch Hetchy, Yosemite, California. *Water Resources Research*, *41*(7), 1–14. https://doi.org/10.1029/2004WR003933

Lundquist, J. D., Dickerson-Lange, S. E., Lutz, J. A., & Cristea, N. C. (2013). Lower forest density enhances snow retention in regions with warmer winters: A global framework developed from plot-scale observations and modeling. *Water Resources Research*, *49*(10), 6356–6370. https://doi.org/10.1002/wrcr.20504

Lundquist, J. D., Roche, J. W., Forrester, H., Moore, C., Keenan, E., Perry, G., et al. (2016). Yosemite Hydroclimate Network: Distributed stream and atmospheric data for the Tuolumne River watershed and surroundings. *Water Resources Research*, *52*(9), 7478–7489. https://doi.org/10.1002/2016WR019261

MacDonald, M. K., Pomeroy, J. W., & Pietroniro, A. (2009). Parameterizing redistribution and sublimation of blowing snow for hydrological models: tests in a mountainous subarctic catchment. *Hydrological Processes*, *23*(18), 2570–2583. https://doi.org/10.1002/hyp.7356

Martin, K. A., Van Stan, J. T., Dickerson-Lange, S. E., Lutz, J. A., Berman, J. W., Gersonde, R., & Lundquist, J. D. (2013). Development and testing of a snow interceptometer to quantify canopy water storage and interception processes in the rain/snow transition zone of the North Cascades, Washington, USA. *Water Resources Research*, *49*(6), 3243–3256. https://doi.org/10.1002/wrcr.20271

Mass, C. F., Albright, M., Ovens, D., Steed, R., MacIver, M., Grimit, E., et al. (2003). Regional environmental prediction over the pacific nothwest. *Bulletin of the American Meteorological Society*, *84*(10), 1353-1366+1328. https://doi.org/10.1175/BAMS-84-10-1353

Mazzotti, G., Currier, W. R., Deems, J. S., Pflug, J. M., Lundquist, J. D., & Jonas, T. (2019). Revisiting Snow Cover Variability and Canopy Structure Within Forest Stands: Insights From Airborne Lidar Data. *Water Resources Research*, *55*(7), 6198–6216. https://doi.org/10.1029/2019wr024898

Mesinger, F., DiMego, G., Kalnay, E., Mitchell, K., Shafran, P. C., Ebisuzaki, W., et al. (2006). North American regional reanalysis. *Bulletin of the American Meteorological Society*, *87*(3), 343–360. https://doi.org/10.1175/BAMS-87-3-343

Moeser, D., Mazzotti, G., Helbig, N., & Jonas, T. (2016). Representing spatial variability of forest snow: Implementation of a new interception model. *Water Resources Research*, *52*(2), 1208–1226. https://doi.org/10.1002/2015WR017961

Molotch, N. P., Brooks, P. D., Burns, S. P., Litvak, M., Monson, R. K., McConnell, J. R., & Musselman, K. N. (2009). Ecohydrological controls on snowmelt partitioning in mixed-conifer sub-alpine forests. *Ecohydrology*, *2*(2), 129–142. https://doi.org/10.1002/eco.48

Monteith, J. L. (1965). Rothamsted Repository Download. *Symposia of the Society for Experimental Biology*, (19), 205–234.

Moore, R. J. (1985). The probability-distributed principle and runoff production at point and basin scales. *Hydrological Sciences Journal*, *30*(2), 273–297. https://doi.org/10.1080/02626668509490989

Moran, P. A. P. (1950). Notes on Continuous Stochastic Phenomena. *Biometrika*, *37*(1/2), 17. https://doi.org/10.2307/2332142

Mott, R., & Lehning, M. (2010). Meteorological Modeling of Very High-Resolution Wind Fields and Snow Deposition for Mountains. *Journal of Hydrometeorology*, *11*, 934–949.

https://doi.org/10.1175/2010JHM1216.1
Mott, R., Schirmer, M., Bavay, M., Grünewald, T., & Lehning, M. (2010). Understanding snow-transport processes shaping the mountain snow-cover. *Cryosphere*, *4*(4), 545–559. https://doi.org/10.5194/tc-4-545-2010
Musselman, K. N., & Pomeroy, J. W. (2017). Estimation of Needleleaf Canopy and Trunk Temperatures and Longwave Contribution to Melting Snow. *Journal of Hydrometeorology*, *18*(2), 555–572. https://doi.org/10.1175/JHM-D-16-0111.1
Musselman, K. N., Molotch, N. P., & Brooks, P. D. (2008). Effects of vegetation on snow accumulation and ablation in a mid-latitude sub-alpine forest. *Hydrological Processes*, *22*(15), 2767–2776. https://doi.org/10.1002/hyp.7050
Musselman, K. N., Pomeroy, J. W., & Link, T. E. (2015). Variability in shortwave irradiance caused by forest gaps: Measurements, modelling, and implications for snow energetics. *Agricultural and Forest Meteorology*, *207*, 69–82. https://doi.org/10.1016/j.agrformet.2015.03.014
Nijssen, B., Schnur, R., & Lettenmaier, D. P. (2001). Global retrospective estimation of soil moisture using the variable infiltration capacity land surface modl, 1980-93. *Journal of Climate*, *14*(8), 1790–1808. https://doi.org/10.1175/1520-0442(2001)014<1790:GREOSM>2.0.CO;2
Painter, T. H., Berisford, D. F., Boardman, J. W., Bormann, K. J., Deems, J. S., Gehrke, F., et al. (2016). The Airborne Snow Observatory: Fusion of scanning lidar, imaging spectrometer, and physically-based modeling for mapping snow water equivalent and snow albedo. *Remote Sensing of Environment*, *184*(July), 139–152. https://doi.org/10.1016/j.rse.2016.06.018
Pfennigbauer, M., & Ullrich, A. (2011). Improving quality of laser scanning data acquisition through calibrated amplitude and pulse deviation measurement. In *Proceedings of SPIE* (p. 76841F). Orlando. https://doi.org/10.1117/12.849641
Pomeroy, J. W., & Gray, D. (1990). Saltation of snow. *Water Resources Research*, *26*(7), 1583–1594. https://doi.org/10.1029/WR026i007p01583
Prokop, A. (2008). Assessing the applicability of terrestrial laser scanning for spatial snow depth measurements. *Cold Regions Science and Technology*, *54*(3), 155–163. https://doi.org/10.1016/j.coldregions.2008.07.002
Prokop, A., Schirmer, M., Rub, M., Lehning, M., & Stocker, M. (2008). A comparison of measurement methods: terrestrial laser scanning, tachymetry and snow probing, for the determination of spatial snow depth distribution on slopes. *Ann Glac*, *49*(1), 210–216. Retrieved from http://id22079462.library.ingentaconnect.com/content/igsoc/agl/2008/00000049/00000001/art00034;jsessionid=14ehp1vm2wl3t.victoria
Rasmussen, R., Baker, B., Kochendorfer, J., Meyers, T., Landolt, S., Fischer, A. P., et al. (2012). How well are we measuring snow: The NOAA/FAA/NCAR winter precipitation test bed. *Bulletin of the American Meteorological Society*, *93*(6), 811–829. https://doi.org/10.1175/BAMS-D-11-00052.1
Reutebuch, S. E., Mcgaughey, R. J., Andersen, H., & Carson, W. W. (2003). Accuracy of a high-resolution lidar terrain model under a conifer forest canopy, *29*(5), 527–535.
Revuelto, J., López-Moreno, J. I., Azorin-Molina, C., & Vicente-Serrano, S. M. (2015). Canopy influence on snow depth distribution in a pine stand determined from terrestrial laser data. *Water Resources Research*, *51*(5), 3476–3489. https://doi.org/10.1002/2014WR016496

Rice, R., & Bales, R. C. (2010). Embedded-sensor network design for snow cover measurements around snow pillow and snow course sites in the Sierra Nevada of California. *Water Resources Research*, *46*(3), 1–13. https://doi.org/10.1029/2008WR007318

Sanford, W. E., & Selnick, D. L. (2013). Erratum to Estimation of Evapotranspiration Across the Conterminous United States Using a Regression with Climate and Land-Cover Data [Journal of the American Water Resources Association (JAWRA), 49, 1 (2012) 217-230]. *Journal of the American Water Resources Association*, *49*(2), 479. https://doi.org/10.1111/jawr.12049

Schirmer, M., & Lehning, M. (2011). Persistence in intra-annual snow depth distribution: 2. Fractal analysis of snow depth development. *Water Resources Research*, *47*(9). https://doi.org/10.1029/2010WR009429

Schirmer, M., Wirz, V., Clifton, A., & Lehning, M. (2011). Persistence in intra-annual snow depth distribution: 1.Measurements and topographic control. *Water Resources Research*, *47*(9), 1–16. https://doi.org/10.1029/2010WR009426

Seyednasrollah, B., & Kumar, M. (2014). Journal of Geophysical Research : Atmospheres, 1–20. https://doi.org/10.1002/2014JD021809.Received

Skamarock, W. C., Klemp, J. B., Dudhi, J., Gill, D. O., Barker, D. M., Duda, M. G., et al. (2008). A Description of the Advanced Research WRF Version 3. *Technical Report*, (June), 113. https://doi.org/10.5065/D6DZ069T

Slater, A. G., Schlosser, C. A., Desborough, C. E., Pitman, A. J., Henderson-Sellers, A., Robock, A., et al. (2001). The Representation of Snow in Land Surface Schemes: Results from PILPS 2(d). *Journal of Hydrometeorology*, *2*(1), 7–25. https://doi.org/10.1175/1525-7541(2001)002<0007:TROSIL>2.0.CO;2

Spaete, L., Glenn, N., Derryberry, D., Sankey, T., Mitchell, J., & Hardegree, S. (2011). Vegetation and Slope Effects on Accutracy of LiDAR-derived DEM in the Sagebrush Steppe. *Remote Sensing Letters*.

Storck, P. (2000). *Trees, snow and flooding: an investigation of forest canopy effects on snow accumulation and melt at the plot and watershed scales in the Pacific Northwest*. Seattle. Retrieved from https://www.ce.washington.edu/sites/cee/files/pdfs/research/hydrology/water-resources/WRS161.pdf

Storck, Pascal, Lettenmaier, D. P., & Bolton, S. M. (2002). Measurement of snow interception and canopy effects on snow accumulation and melt in a mountainous maritime climate, Oregon, United States. *Water Resources Research*, *38*(11), 5-1-5–16. https://doi.org/10.1029/2002WR001281

Sturm, M., Holmgren, J., & Liston, G. E. (1995). A seasonal snow cover classification system for local to global applications. *Journal of Climate*. https://doi.org/10.1175/1520-0442(1995)008<1261:ASSCCS>2.0.CO;2

Sturm, Matthew, & Holmgren, J. (2018). An Automatic Snow Depth Probe for Field Validation Campaigns. *Water Resources Research*. https://doi.org/10.1029/2018WR023559

Sturm, Matthew, Taras, B., Liston, G. E., Derksen, C., Jonas, T., & Lea, J. (2010). Estimating Snow Water Equivalent Using Snow Depth Data and Climate Classes. *Journal of Hydrometeorology*, *11*, 1380–1394. https://doi.org/10.1175/2010JHM1202.1

Sun, N., Wigmosta, M., Zhou, T., Lundquist, J., Dickerson-Lange, S., & Cristea, N. (2018). Evaluating the functionality and streamflow impacts of explicitly modeling forest-snow interactions and canopy gaps in a distributed hydrologic model. *Hydrological Processes*, 1–

39. https://doi.org/10.1002/hyp.13150
Tabler, R. D. (2003). Controlling blowing and drifting snow with snow fences and road design, NCHRP Project 20-7(147). *National Cooperative Highway Research Program Transportation Research Board of the National Academies*, (August), 346.
Tennant, C. J., Harpold, A. A., Lohse, K. A., Godsey, S. E., Crosby, B. T., Larsen, L. G., et al. (2017). Regional sensitivities of seasonal snowpack to elevation, aspect, and vegetation cover in western North America. *Water Resources Research*, *53*(8), 6908–6926. https://doi.org/10.1002/2016WR019374
Thompson, G., Field, P. R., Rasmussen, R. M., & Hall, W. D. (2008). Explicit Forecasts of Winter Precipitation Using an Improved Bulk Microphysics Scheme. Part II: Implementation of a New Snow Parameterization. *Monthly Weather Review*, *136*(12), 5095–5115. https://doi.org/10.1175/2008MWR2387.1
Tinkham, W. T., Huang, H., Smith, A. M. S., Shrestha, R., Falkowski, M. J., Hudak, A. T., et al. (2011). A Comparison of two open source LiDAR surface classification algorithms. *Remote Sensing*, *3*(3), 638–649. https://doi.org/10.3390/rs3030638
Tinkham, W. T., Smith, A. M. S., Marshall, H.-P., Link, T. E., Falkowski, M. J., & Winstral, A. H. (2014). Quantifying spatial distribution of snow depth errors from LiDAR using Random Forest. *Remote Sensing of Environment*, *141*, 105–115. https://doi.org/10.1016/j.rse.2013.10.021
Trujillo, E., Ramírez, J. A., & Elder, K. J. (2007). Topographic, meteorologic, and canopy controls on the scaling characteristics of the spatial distribution of snow depth fields. *Water Resources Research*, *43*(7). https://doi.org/10.1029/2006WR005317
Trujillo, E., Ramírez, J. A., & Elder, K. J. (2009). Scaling properties and spatial organization of snow depth fields in sub-alpine forest and alpine tundra. *Hydrological Processes*, *23*(11), 1575–1590. https://doi.org/10.1002/hyp.7270
Ullrich, A., & Pfennigbauer, C. (2011). Echo Digitization and Waveform Analysis in Airborne and Terrestrial Laser Scanning. *Photogrammetric Week*, 217–228. Retrieved from http://www.ifp.uni-stuttgart.de/publications/phowo11/220Ullrich.pdf
Veatch, W., Brooks, P. D., Gustafson, J. R., & Molotch, N. P. (2009). "Quantifying the effects of forest canopy cover on net snow accumulation at a continental, mid-latitude site." *Ecohydrology*, *2*(2), 115–128. https://doi.org/10.1002/eco.45
Wayand, N. E., Marsh, C. B., Shea, J. M., & Pomeroy, J. W. (2018). Globally scalable alpine snow metrics. *Remote Sensing of Environment*, *213*(May), 61–72. https://doi.org/10.1016/j.rse.2018.05.012
Webster, C., Rutter, N., Zahner, F., & Jonas, T. (2016). Measurement of Incoming Radiation below Forest Canopies: A Comparison of Different Radiometer Configurations. *Journal of Hydrometeorology*, *17*(3), 853–864. https://doi.org/10.1175/JHM-D-15-0125.1
Webster, C., Rutter, N., & Jonas, T. (2017). Improving representation of canopy temperatures for modeling subcanopy incoming longwave radiation to the snow surface. *Journal of Geophysical Research: Atmospheres*, *122*(17), 9154–9172. https://doi.org/10.1002/2017JD026581
Wigmosta, M. S., Vail, L. W., & Lettenmaier, D. P. (1994). A distributed hydrology-vegetation model for complex terrain. *Water Resources Research*, *30*(6), 1665–1679. https://doi.org/10.1029/94WR00436
Wigmosta, M. S., Nijssen, B., & Storck, P. (2002). The distributed hydrology soil vegetation model. *Mathematical Models of Small Watershed Hydrology and Applications*, 7–42.

Retrieved from http://www.cabdirect.org/abstracts/20033121322.html
Wilcoxon, F. (1945). Individual Comparisons by Ranking Methods Frank Wilcoxon. *Biometrics*, *1*(6), 80–83.
Woo, M. K., & Giesbrecht, M. A. (2000). Simulation of snowmelt in a subarctic spruce woodland: 1. Tree model. *Water Resources Research*, *36*(8), 2275–2285. https://doi.org/10.1029/2000WR900094
Xiao, Q., & McPherson, E. G. (2005). Tree health mapping with multispectral remote sensing data at UC Davis, California. *Urban Ecosystems*, *8*(3–4), 349–361. https://doi.org/10.1007/s11252-005-4867-7
Zheng, Z., Kirchner, P. B., & Bales, R. C. (2016). Topographic and vegetation effects on snow accumulation in the southern Sierra Nevada: A statistical summary from lidar data. *Cryosphere*, *10*(1), 257–269. https://doi.org/10.5194/tc-10-257-2016